AD-A137 380 AN INVESTIGATION OF ACOUSTIC INTERACTION WITH THE OCEAN 1/2
BOTTOM FROM EXPER.. (U) TEXAS UNIV AT AUSTIN APPLIED
RESEARCH LABS D P KNOBLES 01 DEC 83 ARL-TR-83-39
UNCLASSIFIED N00014-78-C-0113 F/G 20/1 NL

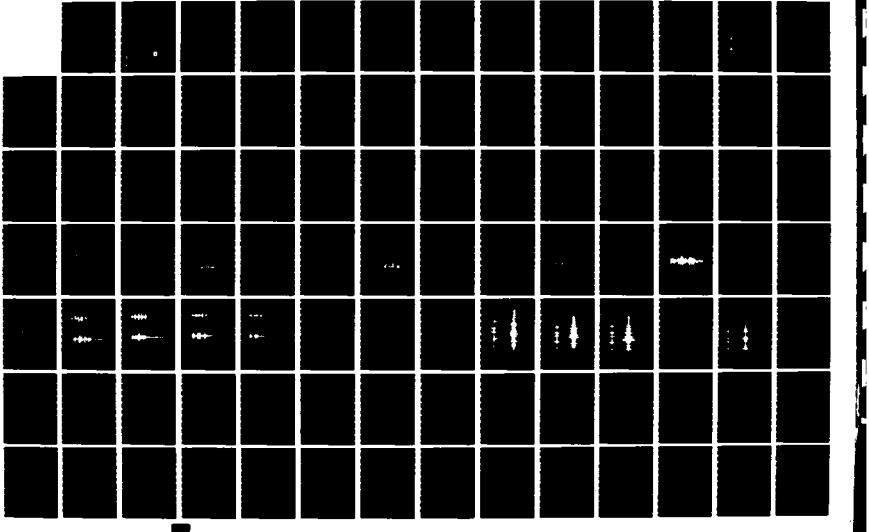

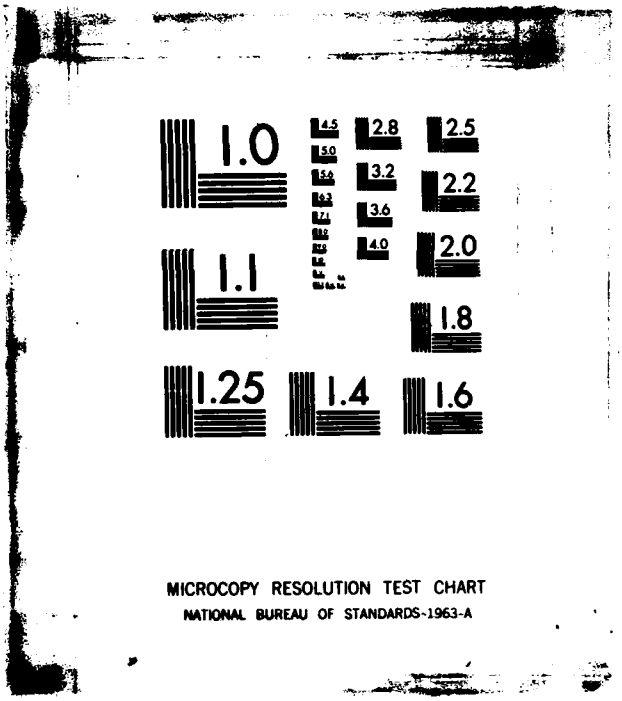
1.0
1.1
1.25
1.4
1.6
1.8
2.0
2.2
2.5
2.8
3.2
3.6
4.0
4.5
5.0
5.6
6.3
7.1
8.0
9.0
10.0
11.2
12.5
14.0
16.0
18.0
20.0
22.4
25.0
28.0
32.0
36.0
40.0
45.0
50.0
56.0
63.0
71.0
80.0
90.0
100.0
112.0
125.0
140.0
160.0
180.0
200.0
224.0
250.0
280.0
320.0
360.0
400.0
450.0
500.0
560.0
630.0
710.0
800.0
900.0
1000.0
1120.0
1250.0
1400.0
1600.0
1800.0
2000.0
2240.0
2500.0
2800.0
3200.0
3600.0
4000.0
4500.0
5000.0
5600.0
6300.0
7100.0
8000.0
9000.0
10000.0
11200.0
12500.0
14000.0
16000.0
18000.0
20000.0
22400.0
25000.0
28000.0
32000.0
36000.0
40000.0
45000.0
50000.0
56000.0
63000.0
71000.0
80000.0
90000.0
100000.0
112000.0
125000.0
140000.0
160000.0
180000.0
200000.0
224000.0
250000.0
280000.0
320000.0
360000.0
400000.0
450000.0
500000.0
560000.0
630000.0
710000.0
800000.0
900000.0
1000000.0
1120000.0
1250000.0
1400000.0
1600000.0
1800000.0
2000000.0
2240000.0
2500000.0
2800000.0
3200000.0
3600000.0
4000000.0
4500000.0
5000000.0
5600000.0
6300000.0
7100000.0
8000000.0
9000000.0
10000000.0
11200000.0
12500000.0
14000000.0
16000000.0
18000000.0
20000000.0
22400000.0
25000000.0
28000000.0
32000000.0
36000000.0
40000000.0
45000000.0
50000000.0
56000000.0
63000000.0
71000000.0
80000000.0
90000000.0
100000000.0
112000000.0
125000000.0
140000000.0
160000000.0
180000000.0
200000000.0
224000000.0
250000000.0
280000000.0
320000000.0
360000000.0
400000000.0
450000000.0
500000000.0
560000000.0
630000000.0
710000000.0
800000000.0
900000000.0
1000000000.0
1120000000.0
1250000000.0
1400000000.0
1600000000.0
1800000000.0
2000000000.0
2240000000.0
2500000000.0
2800000000.0
3200000000.0
3600000000.0
4000000000.0
4500000000.0
5000000000.0
5600000000.0
6300000000.0
7100000000.0
8000000000.0
9000000000.0
10000000000.0
11200000000.0
12500000000.0
14000000000.0
16000000000.0
18000000000.0
20000000000.0
22400000000.0
25000000000.0
28000000000.0
32000000000.0
36000000000.0
40000000000.0
45000000000.0
50000000000.0
56000000000.0
63000000000.0
71000000000.0
80000000000.0
90000000000.0
100000000000.0
112000000000.0
125000000000.0
140000000000.0
160000000000.0
180000000000.0
200000000000.0
224000000000.0
250000000000.0
280000000000.0
320000000000.0
360000000000.0
400000000000.0
450000000000.0
500000000000.0
560000000000.0
630000000000.0
710000000000.0
800000000000.0
900000000000.0
1000000000000.0
1120000000000.0
1250000000000.0
1400000000000.0
1600000000000.0
1800000000000.0
2000000000000.0
2240000000000.0
2500000000000.0
2800000000000.0
3200000000000.0
3600000000000.0
4000000000000.0
4500000000000.0
5000000000000.0
5600000000000.0
6300000000000.0
7100000000000.0
8000000000000.0
9000000000000.0
10000000000000.0
11200000000000.0
12500000000000.0
14000000000000.0
16000000000000.0
18000000000000.0
20000000000000.0
22400000000000.0
25000000000000.0
28000000000000.0
32000000000000.0
36000000000000.0
40000000000000.0
45000000000000.0
50000000000000.0
56000000000000.0
63000000000000.0
71000000000000.0
80000000000000.0
90000000000000.0
100000000000000.0
112000000000000.0
125000000000000.0
140000000000000.0
160000000000000.0
180000000000000.0
200000000000000.0
224000000000000.0
250000000000000.0
280000000000000.0
320000000000000.0
360000000000000.0
400000000000000.0
450000000000000.0
500000000000000.0
560000000000000.0
630000000000000.0
710000000000000.0
800000000000000.0
900000000000000.0
1000000000000000.0
1120000000000000.0
1250000000000000.0
1400000000000000.0
1600000000000000.0
1800000000000000.0
2000000000000000.0
2240000000000000.0
2500000000000000.0
2800000000000000.0
3200000000000000.0
3600000000000000.0
4000000000000000.0
4500000000000000.0
5000000000000000.0
5600000000000000.0
6300000000000000.0
7100000000000000.0
8000000000000000.0
9000000000000000.0
10000000000000000.0
11200000000000000.0
12500000000000000.0
14000000000000000.0
16000000000000000.0
18000000000000000.0
20000000000000000.0
22400000000000000.0
25000000000000000.0
28000000000000000.0
32000000000000000.0
36000000000000000.0
40000000000000000.0
45000000000000000.0
50000000000000000.0
56000000000000000.0
63000000000000000.0
71000000000000000.0
80000000000000000.0
90000000000000000.0
100000000000000000.0
112000000000000000.0
125000000000000000.0
140000000000000000.0
160000000000000000.0
180000000000000000.0
200000000000000000.0
224000000000000000.0
250000000000000000.0
280000000000000000.0
320000000000000000.0
360000000000000000.0
400000000000000000.0
450000000000000000.0
500000000000000000.0
560000000000000000.0
630000000000000000.0
710000000000000000.0
800000000000000000.0
900000000000000000.0
1000000000000000000.0
1120000000000000000.0
1250000000000000000.0
1400000000000000000.0
1600000000000000000.0
1800000000000000000.0
2000000000000000000.0
2240000000000000000.0
2500000000000000000.0
2800000000000000000.0
3200000000000000000.0
3600000000000000000.0
4000000000000000000.0
4500000000000000000.0
5000000000000000000.0
5600000000000000000.0
6300000000000000000.0
7100000000000000000.0
8000000000000000000.0
9000000000000000000.0
10000000000000000000.0
11200000000000000000.0
12500000000000000000.0
14000000000000000000.0
16000000000000000000.0
18000000000000000000.0
20000000000000000000.0
22400000000000000000.0
25000000000000000000.0
28000000000000000000.0
32000000000000000000.0
36000000000000000000.0
40000000000000000000.0
45000000000000000000.0
50000000000000000000.0
56000000000000000000.0
63000000000000000000.0
71000000000000000000.0
80000000000000000000.0
90000000000000000000.0
100000000000000000000.0
112000000000000000000.0
125000000000000000000.0
140000000000000000000.0
160000000000000000000.0
180000000000000000000.0
200000000000000000000.0
224000000000000000000.0
250000000000000000000.0
280000000000000000000.0
320000000000000000000.0
360000000000000000000.0
400000000000000000000.0
450000000000000000000.0
500000000000000000000.0
560000000000000000000.0
630000000000000000000.0
710000000000000000000.0
800000000000000000000.0
900000000000000000000.0
1000000000000000000000.0
1120000000000000000000.0
1250000000000000000000.0
1400000000000000000000.0
1600000000000000000000.0
1800000000000000000000.0
2000000000000000000000.0
2240000000000000000000.0
2500000000000000000000.0
2800000000000000000000.0
3200000000000000000000.0
3600000000000000000000.0
4000000000000000000000.0
4500000000000000000000.0
5000000000000000000000.0
5600000000000000000000.0
6300000000000000000000.0
7100000000000000000000.0
8000000000000000000000.0
9000000000000000000000.0
10000000000000000000000.0
11200000000000000000000.0
12500000000000000000000.0
14000000000000000000000.0
16000000000000000000000.0
18000000000000000000000.0
20000000000000000000000.0
22400000000000000000000.0
25000000000000000000000.0
28000000000000000000000.0
32000000000000000000000.0
36000000000000000000000.0
40000000000000000000000.0
45000000000000000000000.0
50000000000000000000000.0
56000000000000000000000.0
63000000000000000000000.0
71000000000000000000000.0
80000000000000000000000.0
90000000000000000000000.0
100000000000000000000000.0
112000000000000000000000.0
125000000000000000000000.0
140000000000000000000000.0
160000000000000000000000.0
180000000000000000000000.0
200000000000000000000000.0
224000000000000000000000.0
250000000000000000000000.0
280000000000000000000000.0
320000000000000000000000.0
360000000000000000000000.0
400000000000000000000000.0
450000000000000000000000.0
500000000000000000000000.0
560000000000000000000000.0
630000000000000000000000.0
710000000000000000000000.0
800000000000000000000000.0
900000000000000000000000.0
1000000000000000000000000.0
1120000000000000000000000.0
1250000000000000000000000.0
1400000000000000000000000.0
1600000000000000000000000.0
1800000000000000000000000.0
2000000000000000000000000.0
2240000000000000000000000.0
2500000000000000000000000.0
2800000000000000000000000.0
3200000000000000000000000.0
3600000000000000000000000.0
4000000000000000000000000.0
4500000000000000000000000.0
5000000000000000000000000.0
5600000000000000000000000.0
6300000000000000000000000.0
7100000000000000000000000.0
8000000000000000000000000.0
9000000000000000000000000.0
10000000000000000000000000.0
11200000000000000000000000.0
12500000000000000000000000.0
14000000000000000000000000.0
16000000000000000000000000.0
18000000000000000000000000.0
20000000000000000000000000.0
22400000000000000000000000.0
25000000000000000000000000.0
28000000000000000000000000.0
32000000000000000000000000.0
36000000000000000000000000.0
40000000000000000000000000.0
45000000000000000000000000.0
50000000000000000000000000.0
56000000000000000000000000.0
63000000000000000000000000.0
71000000000000000000000000.0
80000000000000000000000000.0
90000000000000000000000000.0
100000000000000000000000000.0
112000000000000000000000000.0
125000000000000000000000000.0
140000000000000000000000000.0
160000000000000000000000000.0
180000000000000000000000000.0
200000000000000000000000000.0
224000000000000000000000000.0
250000000000000000000000000.0
280000000000000000000000000.0
320000000000000000000000000.0
360000000000000000000000000.0
400000000000000000000000000.0
450000000000000000000000000.0
500000000000000000000000000.0
560000000000000000000000000.0
630000000000000000000000000.0
710000000000000000000000000.0
800000000000000000000000000.0
900000000000000000000000000.0
1000000000000000000000000000.0
1120000000000000000000000000.0
1250000000000000000000000000.0
1400000000000000000000000000.0
1600000000000000000000000000.0
1800000000000000000000000000.0
2000000000000000000000000000.0
2240000000000000000000000000.0
2500000000000000000000000000.0
2800000000000000000000000000.0
3200000000000000000000000000.0
3600000000000000000000000000.0
4000000000000000000000000000.0
4500000000000000000000000000.0
5000000000000000000000000000.0
5600000000000000000000000000.0
6300000000000000000000000000.0
7100000000000000000000000000.0
8000000000000000000000000000.0
9000000000000000000000000000.0
10000000000000000000000000000.0
11200000000000000000000000000.0
12500000000000000000000000000.0
14000000000000000000000000000.0
16000000000000000000000000000.0
18000000000000000000000000000.0
20000000000000000000000000000.0
22400000000000000000000000000.0
25000000000000000000000000000.0
28000000000000000000000000000.0
32000000000000000000000000000.0
36000000000000000000000000000.0
40000000000000000000000000000.0
45000000000000000000000000000.0
50000000000000000000000000000.0
56000000000000000000000000000.0
63000000000000000000000000000.0
71000000000000000000000000000.0
80000000000000000000000000000.0
90000000000000000000000000000.0
100000000000000000000000000000.0
112000000000000000000000000000.0
125000000000000000000000000000.0
140000000000000000000000000000.0
160000000000000000000000000000.0
180000000000000000000000000000.0
200000000000000000000000000000.0
224000000000000000000000000000.0
250000000000000000000000000000.0
280000000000000000000000000000.0
320000000000000000000000000000.0
360000000000000000000000000000.0
400000000000000000000000000000.0
450000000000000000000000000000.0
500000000000000000000000000000.0
560000000000000000000000000000.0
630000000000000000000000000000.0
710000000000000000000000000000.0
800000000000000000000000000000.0
900000000000000000000000000000.0
1000000000000000000000000000000.0
1120000000000000000000000000000.0
1250000000000000000000000000000.0
1400000000000000000000000000000.0
1600000000000000000000000000000.0
1800000000000000000000000000000.0
2000000000000000000000000000000.0
2240000000000000000000000000000.0
2500000000000000000000000000000.0
2800000000000000000000000000000.0
3200000000000000000000000000000.0
3600000000000000000000000000000.0
4000000000000000000000000000000.0
4500000000000000000000000000000.0
5000000000000000000000000000000.0
5600000000000000000000000000000.0
6300000000000000000000000000000.0
7100000000000000000000000000000.0
8000000000000000000000000000000.0
9000000000000000000000000000000.0
10000000000000000000000000000000.0
11200000000000000000000000000000.0
12500000000000000000000000000000.0
14000000000000000000000000000000.0
16000000000000000000000000000000.0
18000000000000000000000000000000.0
20000000000000000000000000000000.0
22400000000000000000000000000000.0
25000000000000000000000000000000.0
28000000000000000000000000000000.0
32000000000000000000000000000000.0
36000000000000000000000000000000.0
40000000000000000000000000000000.0
45000000000000000000000000000000.0
50000000000000000000000000000000.0
56000000000000000000000000000000.0
63000000000000000000000000000000.0
71000000000000000000000000000000.0
80000000000000000000000000000000.0
90000000000000000000000000000000.0
100000000000000000000000000000000.0
112000000000000000000000000000000.0
125000000000000000000000000000000.0
140000000000000000000000000000000.0
160000000000000000000000000000000.0
180000000000000000000000000000000.0
200000000000000000000000000000000.0
224000000000000000000000000000000.0
250000000000000000000000000000000.0
280000000000000000000000000000000.0
320000000000000000000000000000000.0
360000000000000000000000000000000.0
400000000000000000000000000000000.0
450000000000000000000000000000000.0
500000000000000000000000000000000.0
560000000000000000000000000000000.0
630000000000000000000000000000000.0
710000000000000000000000000000000.0
800000000000000000000000000000000.0
900000000000000000000000000000000.0
1000000000000000000000000000000000.0
1120000000000000000000000000000000.0
1250000000000000000000000000000000.0
1400000000000000000000000000000000.0
1600000000000000000000000000000000.0
1800000000000000000000000000000000.0
2000000000000000000000000000000000.0
2240000000000000000000000000000000.0
2500000000000000000000000000000000.0
2800000000000000000000000000000000.0
3200000000000000000000000000000000.0
3600000000000000000000000000000000.0
4000000000000000000000000000000000.0
4500000000000000000000000000000000.0
5000000000000000000000000000000000.0
5600000000000000000000000000000000.0
6300000000000000000000000000000000.0
7100000000000000000000000000000000.0
8000000000000000000000000000000000.0
9000000000000000000000000000000000.0
10000000000000000000000000000000000.0
11200000000000000000000000000000000.0
12500000000000000000000000000000000.0
14000000000000000000000000000000000.0
16000000000000000000000000000000000.0
18000000000000000000000000000000000.0
20000000000000000000000000000000000.0
22400000000000000000000000000000000.0
25000000000000000000000000000000000.0
28000000000000000000000000000000000.0
32000000000000000000000000000000000.0
36000000000000000000000000000000000.0
40000000000000000000000000000000000.0
45000000000000000000000000000000000.0
50000000000000000000000000000000000.0
56000000000000000000000000000000000.0
63000000000000000000000000000000000.0
71000000000000000000000000000000000.0
80000000000000000000000000000000000.0
90000000000000000000000000000000000.0
100000000000000000000000000000000000.0
112000000000000000000000000000000000.0
125000000000000000000000000000000000.0
140000000000000000000000000000000000.0
160000000000000000000000000000000000.0
180000000000000000000000000000000000.0
200000000000000000000000000000000000.0
224000000000000000000000000000000000.0
250000000000000000000000000000000000.0
280000000000000000000000000000000000.0
320000000000000000000000000000000000.0
360000000000000000000000000000000000.0
400000000000000000000000000000000000.0
450000000000000000000000000000000000.0
500000000000000000000000000000000000.0
560000000000000000000000000000000000.0
630000000000000000000000000000000000.0
710000000000000000000000000000000000.0
800000000000000000000000000000000000.0
900000000000000000000000000000000000.0
1000000000000000000000000000000000000.0
1120000000000000000000000000000000000.0
1250000000000000000000000000000000000.0
1400000000000000000000000000000000000.0
1600000000000000000000000000000000000.0
1800000000000000000000000000000000000.0
2000000000000000000000000000000000000.0
2240000000000000000000000000000000000.0
2500000000000000000000000000000000000.0
2800000000000000000000000000000000000.0
3200000000000000000000000000000000000.0
3600000000000000000000000000000000000.0
4000000000000000000000000000000000000.0
4500000000000000000000000000000000000.0
5000000000000000000000000000000000000.0
5600000000000000000000000000000000000.0
6300000000000000000000000000000000000.0
7100000000000000000000000000000000000.0
8000000000000000000000000000000000000.0
9000000000000000000000000000000000000.0
10000000000000000000000000000000000000.0
11200000000000000000000000000000000000.0
12500000000000000000000000000000000000.0
14000000000000000000000000000000000000.0
16000000000000000000000000000000000000.0
18000000000000000000000000000000000000.0
20000000000000000000000000000000000000.0
22400000000000000000000000000000000000.0
25000000000000000000000000000000000000.0
28000000000000000000000000000000000000.0
32000000000000000000000000000000000000.0
36000000000000000000000000000000000000.0
40000000000000000000000000000000000000.0
45000000000000000000000000000000000000.0
50000000000000000000000000000000000000.0
56000000000000000000000000000000000000.0
63000000000000000000000000000000000000.0
71000000000000000000000000000000000000.0
80000000000000000000000000000000000000.0
90000000000000000000000000000000000000.0
100000000000000000000000000000000000000.0
112000000000000000000000000000000000000.0
125000000000000000000000000000000000000.0
140000000000000000000000000000000000000.0
160000000000000000000000000000000000000.0
180000000000000000000000000000000000000.0
200000000000000000000000000000000000000.0
224000000000000000000000000000000000000.0
250000000000000000000000000000000000000.0
280000000000000000000000000000000000000.0
320000000000000000000000000000000000000.0
360000000000000000000000000000000000000.0
400000000000000000000000000000000000000.0
450000000000000000000000000000000000000.0
500000000000000000000000000000000000000.0
560000000000000000000000000000000000000.0
630000000000000000000000000000000000000.0
710000000000000000000000000000000000000.0
800000000000000000000000000000000000000.0
900000000000000000000000000000000000000.0
1000000000000000000000000000000000000000.0
1120000000000000000000000000000000000000.0
1250000000000000000000000000000000000000.0
1400000000000000000000000000000000000000.0
1600000000000000000000000000000000000000.0
1800000000000000000000000000000000000000.0
2000000000000000000000000000000000000000.0
2240000000000000000000000000000000000000.0
2500000000000000000000000000000000000000.0
2800000000000000000000000000000000000000.0
3200000000000000000000000000000000000000.0
3600000000000000000000000000000000000000.0
4000000000000000000000000000000000000000.0
4500000000000000000000000000000000000000.0
5000000000000000000000000000000000000000.0
5600000000000000000000000000000000000000.0
6300000000000000000000000000000000000000.0
7100000000000000000000000000000000000000.0
8000000000000000000000000000000000000000.0
9000000000000000000000000000000000000000.0
10000000000000000000000000000000000000000.0
11200000000000000000000000000000000000000.0
12500000000000000000000000000000000000000.0
14000000000000000000000000000000000000000.0
16000000000000000000000000000000000000000.0
18000000000000000000000000000000000000000.0
20000000000000000000000000000000000000000.0
22400000000000000000000000000000000000000.0
25000000000000000000000000000000000000000.0
28000000000000000000000000000000000000000.0
32000000000000000000000000000000000000000.0
36000000000000000000000000000000000000000.0
40000000000000000000000000000000000000000.0
45000000000000000000000000000000000000000.0
50000000000000000000000000000000000000000.0
56000000000000000000000000000000000000000.0
63000000000000000000000000000000000000000.0
71000000000000000000000000000000000000000.0
80000000000000000000000000000000000000000.0
90000000000000000000000000000000000000000.0
100000000000000000000000000000000000000000.0
112000000000000000000000000000000000000000.0
125000000000000000000000000000000000000000.0
140000000000000000000000000000000000000000.0
160000000000000000000000000000000000000000.0
180000000000000000000000000000000000000000.0
200000000000000000000000000000000000000000.0
224000000000000000000000000000000000000000.0
250000000000000000000000000000000000000000.0
280000000000000000000000000000000000000000.0
320000000000000000000000000000000000000000.0
360000000000000000000000000000000000000000.0
400000000000000000000000000000000000000000.0
450000000000000000000000000000000000000000.0
500000000000000000000000000000000000000000.0
560000000000000000000000000000000000000000.0
630000000000000000000000000000000000000000.0
710000000000000000000000000000000000000000.0
800000000000000000000000000000000000000000.0
900000000000000000000000000000000000000000.0
1000000000000000000000000000000000000000000.0
1120000000000000000000000000000000000000000.0
1250000000000000000000000000000000000000000.0
1400000000000000000000000000000000000000000.0
1600000000000000000000000000000000000000000.0
1800000000000000000000000000000000000000000.0
2000000000000000000000000000000000000000000.0
2240000000000000000000000000000000000000000.0
2500000000000000000000000000000000000000000.0
2800000000000000000000000000000000000000000.0
3200000000000000000000000000000000000000000.0
3600000000000000000000000000000000000000000.0
4000000000000000000000000000000000000000000.0
4500000000000000000000000000000000000000000.0
5000000000000000000000000000000000000000000.0
5600000000000000000000000000000000000000000.0
6300000000000000000000000000000000000000000.0
7100000000000000000000000000000000000000000.0
8000000000000000000000000000000000000000000.0
9000000000000000000000000000000000000000000.0
10000000000000000000000000000000000000000000.0
11200000000000000000000000000000000000000000.0
12500000000000000000000000000000000000000000.0
14000000000000000000000000000000000000000000.0
16000000000000000000000000000000000000000000.0
18000000000000000000000000000000000000000000.0
20000000000000000000000000000000000000000000.0
22400000000000000000000000000000000000000000.0
25000000000000000000000000000000000000000000.0
28000000000000000000000000000000000000000000.0
32000000000000000000000000000000000000000000.0
36000000000000000000000000000000000000000000.0
40000000000000000000000000000000000000000000.0
45000000000000000000000000000000000000000000.0
50000000000000000000000000000000000000000000.0
56000000000000000000000000000000000000000000.0
63000000000000000000000000000000000000000000.0
71000000000000000000000000000000000000000000.0
80000000000000000000000000000000000000000000.0
90000000000000000000000000000000000000000000.0
100000000000000000000000000000000000000000000.0
112000000000000000000000000000000000000000000.0
125000000000000000000000000000000000000000000.0
140000000000000000000000000000000000000000000.0
160000000000000000000000000000000000000000000.0
180000000000000000000000000000000000000000000.0
200000000000000000000000000000000000000000000.0
224000000000000000000000000000000000000000000.0
250000000000000000000000000000000000000000000.0
280000000000000000000000000000000000000000000.0
320000000000000000000000000000000000000000000.0
360000000000000000000000000000000000000000000.0
400000000000000000000000000000000000000000000.0
450000000000000000000000000000000000000000000.0
500000000000000000000000000000000000000000000.0
560000000000000000000000000000000000000000000.0
630000000000000000000000000000000000000000000.0
710000000000000000000000000000000000000000000.0
800000000000000000000000000000000000000000000.0
900000000000000000000000000000000000000000000.0
1000000000000000000000000000000000000000000000.0
1120000000000000000000000000000000000000000000.0
1250000000000000000000000000000000000000000000.0
1400000000000000000000000000000000000000000000.0
1600000000000000000000000000000000000000000000.0
1800000000000000000000000000000000000000000000.0
2000000000000000000000000000000000000000000000.0
2240000000000000000000000000000000000000000000.0
2500000000000000000000000000000000000000000000.0
2800000000000000000000000000000000000000000000.0
3200000000000000000000000000000000000000000000.0
3600000000000000000000000000000000000000000000.0
4000000000000000000000000000000000000000000000.0
4500000000000000000000000000000000000000000000.0
5000000000000000000000000000000000000000000000.0
5600000000000000000000000000000000000000000000.0
6300000000000000000000000000000000000000000000.0
7100000000000000000000000000000000000000000000.0
8000000000000000000000000000000000000000000000.0
9000000000000000000000000000000000000000000000.0
10000000000000000000000000000000000000000000000.0
11200000000000000000000000000000000000000000000.0
12500000000000000000000000000000000000000000000.0
14000000000000000000000000000000000000000000000.0
16000000000000000000000000000000000000000000000.0
18000000000000000000000000000000000000000000000.0
20000000000000000000000000000000000000000000000.0
22400000000000000000000000000000000000000000000.0
25000000000000000000000000000000000000000000000.0
28000000000000000000000000000000000000000000000.0
32000000000000000000000000000000000000000000000.0
36000000000000000000000000000000000000000000000.0
40000000000000000000000000000000000000000000000.0
45000000000000000000000000000000000000000000000.0
50000000000000000000000000000000000000000000000.0
56000000000000000000000000000000000000000000000.0
63000000000000000000000000000000000000000000000.0
71000000000000000000000000000000000000000000000.0
80000000000000000000000000000000000000000000000.0
90000000000000000000000000000000000000000000000.0
100000000000000000000000000000000000000000000000.0
112000000000000000000000000000000000000000000000.0
125000000000000000000000000000000000000000000000.0
140000000000000000000000000000000000000000000000.0
160000000000000000000000000000000000000000000000.0
180000000000000000000000000000000000000000000000.0
200000000000000000000000000000000000000000000000.0
224000000000000000000000000000000000000000000000.0
250000000000000000000000000000000000000000000000.0
280000000000000000000000000000000000000000000000.0
320000000000000000000000000000000000000000000000.0
360000000000000000000000000000000000000000000000.0
400000000000000000000000000000000000000000000000.0
450000000000000000000000000000000000000000000000.0
500000000000000000000000000000000000000000000000.0
560000000000000000000000000000000000000000000000.0
630000000000000000000000000000000000000000000000.0
710000000000000000000000000000000000000000000000.0
800000000000000000000000000000000000000000000000.0
900000000000000000000000000000000000000000000000.0
1000000000000000000000000000000000000000000000000.0
1120000000000000000000000000000000000000000000000.0
1250000000000000000000000000000000000000000000000.0
1400000000000000000000000000000000000000000000000.0
1600000000000000000000000000000000000000000000000.0
1800000000000000000000000000000000000000000000000.0
2000000000000000000000000000000000000000000000000.0
2240000000000000000000000000000000000000000000000.0
2500000000000000000000000000000000000000000000000.0
2800000000000000000000000000000000000000000000000.0
3200000000000000000000000000000000000000000000000.0
3600000000000000000000000000000000000000000000000.0
4000000000000000000000000000000000000000000000000.0
4500000000000000000000000000000000000000000000000.0
5000000000000000000000000000000000000000000000000.0
5600000000000000000000000000000000000000000000000.0
6300000000000000000000000000000000000000000000000.0
7100000000000000000000000000000000000000000000000.0
8000000000000000000000000000000000000000000000000.0
9000000000000000000000000000000000000000000000000.0
10000000000000000000000000000000000000000000000000.0
11200000000000000000000000000000000000000000000000.0
12500000000000000000000000000000000000000000000000.0
14000000000000000000000000000000000000000000000000.0
16000000000000000000000000000000000000000000000000.0
18000000000000000000000000000000000000000000000000.0
20000000000000000000000000000000000000000000000000.0
22400000000000000000000000000000000000000000000000.0
25000000000000000000000000000000000000000000000000.0
28000000000000000000000000000000000000000000000000.0
32000000000000000000000000000000000000000000000000.0
36000000000000000000000000000000000000000000000000.0
40000000000000000000000000000000000000000000000000.0
45000000000000000000000000000000000000000000000000.0
50000000000000000000000000000000000000000000000000.0
56000000000000000000000000000000000000000000000000.0
63000000000000000000000000000000000000000000000000.0
71000000000000000000000000000000000000000000000000.0
80000000000000000000000000000000000000000000000000.0
90000000000000000000000000000000000000000000000000.0
100000000000000000000000000000000000000000000000000.0
112000000000000000000000000000000000000000000000000.0
125000000000000000000000000000000000000000000000000.0
140000000000000000000000000000000000000000000000000.0
160000000000000000000000000000000000000000000000000.0
180000000000000000000000000000000000000000000000000.0
200000000000000000000000000000000000000000000000000.0
224000000000000000000000000000000000000000000000000.0
250000000000000000000000000000000000000000000000000.0
280000000000000000000000000000000000000000000000000.0
320000000000000000000000000000000000000000000000000.0
360000000000000000000000000000000000000000000000000.0
400000000000000000000000000000000000000000000000000.0
450000000000000000000000000000000000000000000000000.0
500000000000000000000000000000000000000000000000000.0
560000000000000000000000000000000000000000000000000.0
630000000000000000000000000000000000000000000000000.0
710000000000000000000000000000000000000000000000000.0
800000000000000000000000000000000000000000000000000.0
900000000000000000000000000000000000000000000000000.0
1000000000000000000000000000000000000000000000000000.0
1120000000000000000000000000000000000000000000000000.0
1250000000000000000000000000000000000000000000000000.0
1400000000000000000000000000000000000000000000000000.0
1600000000000000000000000000000000000000000000000000.0
1800000000000000000000000000000000000000000000000000.0
2000000000000000000000000000000000000000000000000000.0
2240000000000000000000000000000000000000000000000000.0
2500000000000000000000000000000000000000000000000000.0
2800000000000000000000000000000000000000000000000000.0
3200000000000000000000000000000000000000000000000000.0
3600000000000000000000000000000000000000000000000000.0
4000000000000000000000000000000000000000000000000000.0
4500000000000000000000000000000000000000000000000000.0
5000000000000000000000000000000000000000000000000000.0
5600000000000000000000000000000000000000000000000000.0
6300000000000000000000000000000000000000000000000000.0
7100000000000000000000000000000000000000000000000000.0
8000000000000000000000000000000000000000000000000000.0
9000000000000000000000000000000000000000000000000000.0
10000000000000000000000000000000000000000000000000000.0
11200000000000000000000000000000000000000000000000000.0
12500000000000000000000000000000000000000000000000000.0
14000000000000000000000000000000000000000000000000000.0
16000000000000000000000000000000000000000000000000000.0
18000000000000000000000000000000000000000000000000000.0
20000000000000000000000000000000000000000000000000000.0
22400000000000000000000000000000000000000000000000000.0
25000000000000000000000000000000000000000000000000000.0
28000000000000000000000000000000000000000000000000000.0
32000000000000000000000000000000000000000000000000000.0
36000000000000000000000000000000000000000000000000000.0
40000000000000000000000000000000000000000000000000000.0
45000000000000000000000000000000000000000000000000000.0
50000000000000000000000000000000000000000000000000000.0
56000000000000000000000000000000000000000000000000000.0
63000000000000000000000000000000000000000000000000000.0
71000000000000000000000000000000000000000000000000000.0
80000000000000000000000000000000000000000000000000000.0
90000000000000000000000000000000000000000000000000000.0
100000000000000000000000000000000000000000000000000000.0
112000000000000000000000000000000000000000000000000000.0
125000000000000000000000000000000000000000000000000000.0
140000000000000000000000000000000000000000000000000000.0
160000000000000000000000000000000000000000000000000000.0
180000000000000000000000000000000000000000000000000000.0
200000000000000000000000000000000000000000000000000000.0
224000000000000000000000000000000000000000000000000000.0
250000000000000000000000000000000000000000000000000000.0
280000000000000000000000000000000000000000000000000000.0
320000000000000000000000000000000000000000000000000000.0
360000000000000000000000000000000000000000000000000000.0
400000000000000000000000000000000000000000000000000000.0
450000000000000000000000000000000000000000000000000000.0
500000000000000000000000000000000000000000000000000000.0
560000000000000000000000000000000000000000000000000000.0
630000000000000000000000000000000000000000000000000000.0
710000000000000000000000000000000000000000000000000000.0
800000000000000000000000000000000000000000000000000000.0
900000000000000000000000000000000000000000000000000000.0
1000000000000000000000000000000000000000000000000000000.0
1120000000000000000000000000000000000000000000000000000.0
1250000000000000000000000000000000000000000000000000000.0
1400000000000000000000000000000000000000000000000000000.0
1600000000000000000000000000000000000000000000000000000.0
1800000000000000000000000000000000000000000000000000000.0
2000000000000000000000000000000000000000000000000000000.0
2240000000000000000000000000000000000000000000000000000.0
2500000000000000000000000000000000000000000000000000000.0
2800000000000000000000000000000000000000000000000000000.0
3200000000000000000000000000000000000000000000000000000.0
3600000000000000000000000000000000000000000000000000000.0
4000000000000000000000000000000000000000000000000000000.0
4500000000000000000000000000000000000000000000000000000.0
5000000000000000000000000000000000000000000000000000000.0
5600000000000000000000000000000000000000000000000000000.0
6300000000000000000000000000000000000000000000000000000.0
7100000000000000000000000000000000000000000000000000000.0
8000000000000000000000000000000000000000000000000000000.0
9000000000000000000000000000000000000000000000000000000.0
10000000000000000000000000000000000000000000000000000000.0
11200000000000000000000000000000000000000000000000000000.0
12500000000000000000000000000000000000000000000000000000.0
14000000000000000000000000000000000000000000000000000000.0
16000000000000000000000000000000000000000000000000000000.0
18000000000000000000000000000000000000000000000000000000.0
20000000000000000000000000000000000000000000000000000000.0
22400000000000000000000000000000000000000000000000000000.0
25000000000000000000000000000000000000000000000000000000.0
28000000000000000000000000000000000000000000000000000000.0
32000000000000000000000000000000000000000000000000000000.0
36000000000000000000000000000000000000000000000000000000.0
40000000000000000000000000000000000000000000000000000000.0
45000000000000000000000000000000000000000000000000000000.0
50000000000000000000000000000000000000000000000000000000.0
56000000000000000000000000000000000000000000000000000000.0
63000000000000000000000000000000000000000000000000000000.0
71000000000000000000000000000000000000000000000000000000.0
80000000000000000000000000000000000000000000000000000000.0
90000000000000000000000000000000000000000000000000000000.0
100000000000000000000000000000000000000000000000000000000.0
112000000000000000000000000000000000000000000000000000000.0
125000000000000000000000000000000000000000000000000000000.0
140000000000000000000000000000000000000000000000000000000.0
160000000000000000000000000000000000000000000000000000000.0
180000000000000000000000000000000000000000000000000000000.0
200000000000000000000000000000000000000000000000000000000.0
224000000000000000000000000000000000000000000000000000000.0
250000000000000000000000000000000000000000000000000000000.0
280000000000000000000000000000000000000000000000000000000.0
320000000000000000000000000000000000000000000000000000000.0
360000000000000000000000000000000000000000000000000000000.0
400000000000000000000000000000000000000000000000000000000.0
450000000000000000000000000000000000000000000000000000000.0
500000000000000000000000000000000000000000000000000000000.0
560000000000000000000000000000000000000000000000000000000.0
630000000000000000000000000000000000000000000000000000000.0
710000000000000000000000000000000000000000000000000000000.0
800000000000000000000000000000000000000000000000000000000.0
900000000000000000000000000000000000000000000000000000000.0
1000000000000000000000000000000000000000000000000000000000.0
1120000000000000000000000000000000000000000000000000000000.0
1250000000000000000000000000000000000000000000000000000000.0
1400000000000000000000000000000000000000000000000000000000.0
1600000000000000000000000000000000000000000000000000000000.0
1800000000000000000000000000000000000000000000000000000000.0
2000000000000000000000000000000000000000000000000000000000.0
2240000000000000000000000000000000000000000000000000000000.0
2500000000000000000000000000000000000000000000000000000000.0
2800000000000000000000000000000000000000000000000000000000.0
3200000000000000000000000000000000000000000000000000000000.0
3600000000000000000000000000000000000000000000000000000000.0
4000000000000000000000000000000000000000000000000000000000.0
4500000000000000000000000000000000000000000000000000000000.0
5000000000000000000000000000000000000000000000000000000000.0
5600000000000000000000000000000000000000000000000000000000.0
6300000000000000000000000000000000000000000000000000000000.0
7100000000000000000000000000000000000000000000000000000000.0
8000000000000000000000000000000000000000000000000000000000.0
9000000000000000000000000000000000000000000000000000000000.0
10000000000000000000000000000000000000000000000000000000000.0
11200000000000000000000000000000000000000000000000000000000.0
12500000000000000000000000000000000000000000000000000000000.0
14000000000000000000000000000000000000000000000000000000000.0
16000000000000000000000000000000000000000000000000000000000.0
18000000000000000000000000000000000000000000000000000000000.0
20000000000000000000000000000000000000000000000000000000000.0
22400000000000000000000000000000000000000000000000000000000.0
25000000000000000000000000000000000000000000000000000000000.0
28000000000000000000000000000000000000000000000000000000000.0
32000000000000000000000000000000000000000000000000000000000.0
36000000000000000000000000000000000000000000000000000000000.0
40000000000000000000000000000000000000000000000000000000000.0
45000000000000000000000000000000000000000000000000000000000.0
50000000000000000000000000000000000000000000000000000000000.0
56000000000000000000000000000000000000000000000000000000000.0
63000000000000000000000000000000000000000000000000000000000.0
71000000000000000000000000000000000000000000000000000000000.0
80000000000000000000000000000000000000000000000000000000000.0
90000000000000000000000000000000000000000000000000000000000.0
100000000000000000000000000000000000000000000000000000000000.0
112000000000000000000000000000000000000000000000000000000000.0
125000000000000000000000000000000000000000000000000000000000.0
140000000000000000000000000000000000000000000000000000000000.0
160000000000000000000000000000000000000000000000000000000000.0
180000000000000000000000000000000000000000000000000000000000.0
200000000000000000000000000000000000000000000000000000000000.0
224000000000000000000000000000000000000000000000000000000000.0
250000000000000000000000000000000000000000000000000000000000.

(12)

ARL-TR-83-39

Copy No. 41

AN INVESTIGATION OF ACOUSTIC INTERACTION WITH THE OCEAN BOTTOM FROM EXPERIMENTAL TIME SERIES GENERATED BY EXPLOSIVE SOURCES

David P. Knobles

APPLIED RESEARCH LABORATORIES
THE UNIVERSITY OF TEXAS AT AUSTIN
POST OFFICE BOX 8029, AUSTIN, TEXAS 78712-8029

1 December 1983

Technical Report

Prepared for:

NAVAL OCEAN RESEARCH
AND DEVELOPMENT ACTIVITY
NSTL STATION, MS 39529

UNCLASSIFIED

SECURITY CLASSIFICATION OF THIS PAGE *(When Data Entered)*

REPORT DOCUMENTATION PAGE		READ INSTRUCTIONS BEFORE COMPLETING FORM
1. REPORT NUMBER	2. GOVT ACCESSION NO. AD-A137380	3. RECIPIENT'S CATALOG NUMBER
4. TITLE *(and Subtitle)* AN INVESTIGATION OF ACOUSTIC INTERACTION WITH THE OCEAN BOTTOM FROM EXPERIMENTAL TIME SERIES GENERATED BY EXPLOSIVE SOURCES		5. TYPE OF REPORT & PERIOD COVERED Technical Report
		6. PERFORMING ORG. REPORT NUMBER ARL-TR-83-39
7. AUTHOR(s) David P. Knobles		8. CONTRACT OR GRANT NUMBER(s) N00014-78-C-0113
9. PERFORMING ORGANIZATION NAME AND ADDRESS Applied Research Laboratories The University of Texas at Austin Austin, Texas 78712-8029		10. PROGRAM ELEMENT, PROJECT, TASK AREA & WORK UNIT NUMBERS
11. CONTROLLING OFFICE NAME AND ADDRESS Naval Ocean Research and Development Activity NSTL Station, Mississippi 39529		12. REPORT DATE 1 December 1983
		13. NUMBER OF PAGES 94
14. MONITORING AGENCY NAME & ADDRESS *(if different from Controlling Office)*		15. SECURITY CLASS. *(of this report)* UNCLASSIFIED
		15a. DECLASSIFICATION/DOWNGRADING SCHEDULE

16. DISTRIBUTION STATEMENT *(of this Report)*

Approved for public release; distribution unlimited.

17. DISTRIBUTION STATEMENT *(of the abstract entered in Block 20, if different from Report)*

18. SUPPLEMENTARY NOTES

19. KEY WORDS *(Continue on reverse side if necessary and identify by block number)*

ocean acoustics	scattering
bottom interaction	reflection
time series	refraction
geoacoustic profile	experiment
explosive sources	theory

20. ABSTRACT *(Continue on reverse side if necessary and identify by block number)*

Received time series from explosive sources in an abyssal plains ocean environment are compared to simulated time series calculated by a ray theory model. The comparisons yield information concerning the geoacoustic profile with a single sediment layer. The comparisons are made in various frequency bands to aid in identifying sediment penetrating arrivals by taking advantage of the frequency dependence of the absorption of the sediment. For shorter ranges, the sediment penetrating rays reflect off the basement. Also, as the range decreases, the fraction of received

DD FORM 1 JAN 73 1473 EDITION OF 1 NOV 65 IS OBSOLETE

UNCLASSIFIED

SECURITY CLASSIFICATION OF THIS PAGE *(When Data Entered)*

20. (cont'd)

energy due to reflections at the water-sediment interface increases. Discrepancies between the experimental and simulated time series are interpreted in terms of reflections from thin layers within the sediment and scattered basement reflections.

TABLE OF CONTENTS

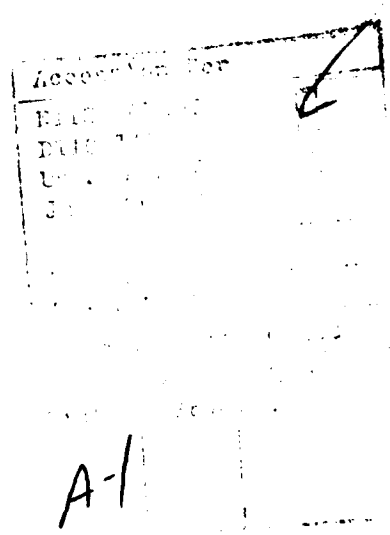

LIST OF FIGURES

I. INTRODUCTION

In order to describe the properties of sound propagation within an ocean environment, a clear understanding of the physics of the acoustic interaction with the ocean bottom is in many cases essential. Assuming linearity, the nature of this interaction is governed by a single function, which is a solution to the inhomogeneous wave equation whose initial data consist of the boundary conditions imposed by the environment and a unit source concentrated in space-time. It follows that, in principle, a precise knowledge of the geoacoustic profile of the seafloor (the depth dependence of the sound speed, density, and intrinsic attenuation) would enable one to accurately predict the effect of bottom interaction on sound propagation.

No single geoacoustic profile can account for the varied bottom structures found in the world's oceans. Pieces of the ocean bottom have been obtained from coring operations such as those conducted by the Deep Sea Drilling Project (DSDP). In situ measurements and laboratory measurements of the recovered materials have provided average geoacoustic parameters for the continental terrace, the abyssal plains, and the abyssal hills environments. These average parameters are usually the starting point in the construction of geoacoustic profiles for a particular region.

A powerful method in the construction of a geoacoustic profile for a given region is an analysis of acoustical bottom interaction experiments. The idea is to analyze pressure time series generated by explosive sources in a manner so as to yield information on the structure of the ocean bottom. The analysis takes the form of a data-model comparison. Initially, one starts with a simple bottom structure, based on the average geoacoustic parameters mentioned above and, if necessary, adjusts the parameters within known bounds to obtain the best fit to the data. Discrepancies are interpreted and provide a transition to a more complicated profile, namely one involving a more detailed representation of the actual structure. During the interpretation process, one must be aware that some of the discrepancies can be due to errors in the reported source and receiver geometry.

This report presents the results of an analysis of measured pressure time series generated by explosive charges, or SUS (sound underwater signaling) charges, in an abyssal plains ocean environment characterized by a moderately thin sediment cover (200 m). The remainder of this report is structured as follows. Section II briefly describes the experimental process and presents a sample of the experimental data. Section III describes the theoretical model which predicts the received pressure due to a TNT charge explosion as a function of time. Section IV compares the experiment to the theory, and Section V summarizes the results.

II. THE EXPERIMENTAL DATA

The focus of this study is an analysis of pressure time series data obtained in the northern Tufts abyssal plains, located in the NE Pacific Ocean. Here, the depth of the ocean is about 4500 m and the bottom bathymetry is characterized by numerous seamounts and channels. The sediments are classified as turbidites (sediments deposited by turbidity currents).[1-2] The total sediment thickness is approximately 200 m. Figure 1 illustrates the experimental procedure. Ship A drops an 816 g (1.8 lb) SUS explosive charge set to detonate at a depth of 244 m. An analysis of SUS charge explosions shows that there is typically a spread of $\pm$10% in the detonation depth about the nominal value.[3] A hydrophone and recording apparatus fastened to the end of a cable from Ship B at a reported depth of 205 m records the received pressure as a function of time. The analog acoustic data are later digitized and tentatively analyzed in terms of multipath arrivals.[4] The experiment is repeated at various ranges (distances between the two ships). During the experiments, the water sound speed is measured as a function of depth.

Figure 2 is a sketch of recorded pressure signals generated by an explosive charge in a deep ocean environment. The general characteristics of the received waveform can be understood by viewing the ocean as a two-dimensional waveguide where the water-air interface forms the top boundary and the water-sediment interface forms the bottom. For

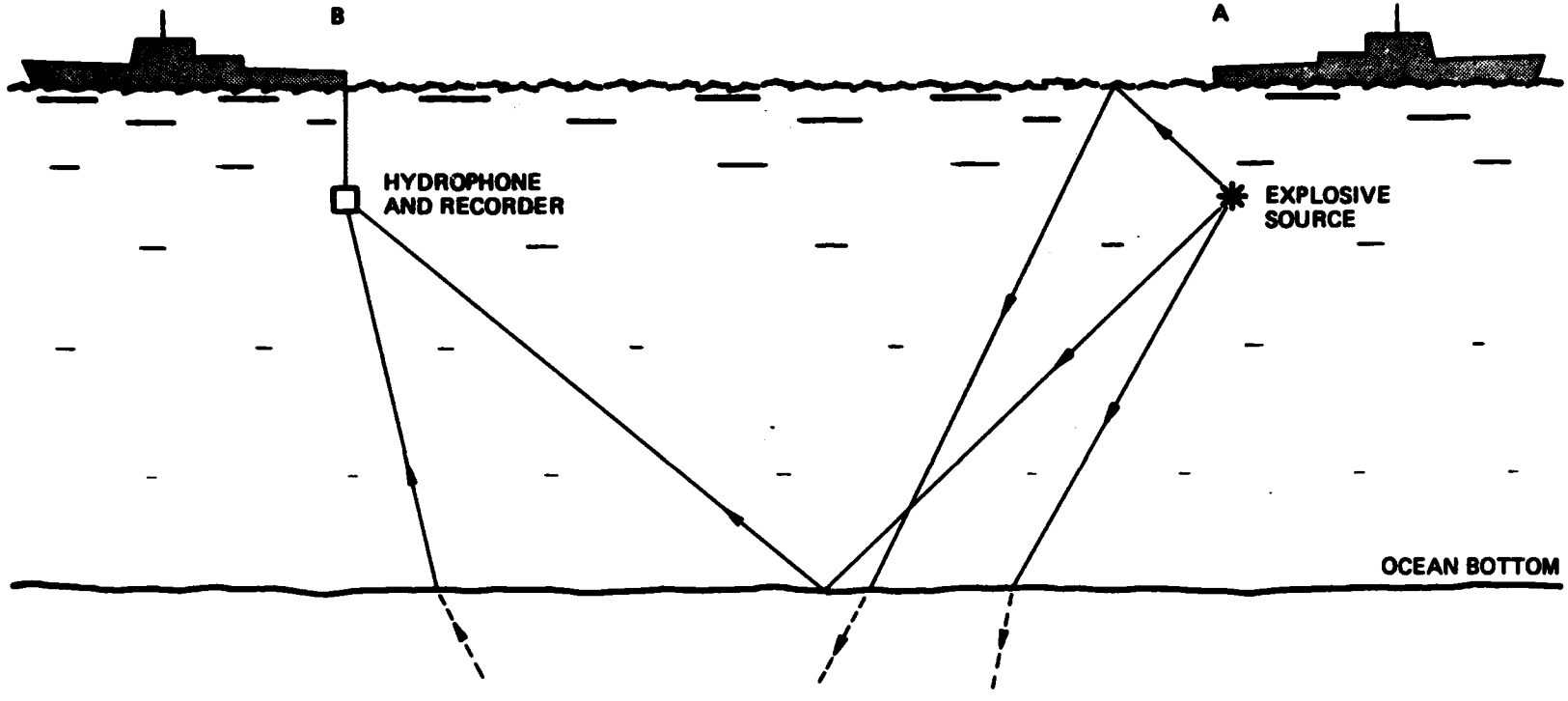

FIGURE 1
GEOMETRY OF BOTTOM INTERACTION EXPERIMENT

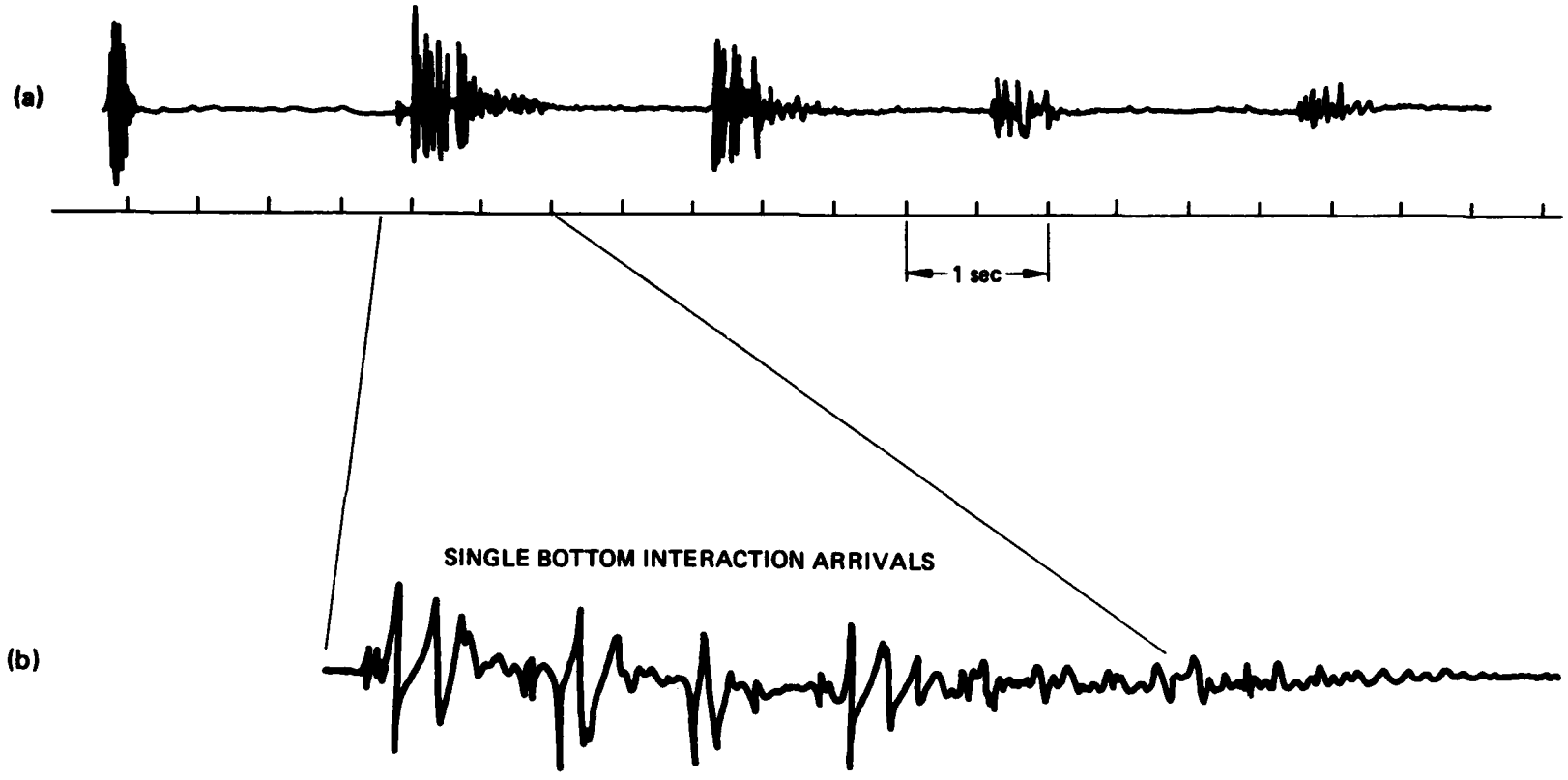

FIGURE 2
SKETCH OF RECEIVED TIME SERIES GENERATED BY AN EXPLOSIVE SOURCE IN A DEEP WATER ENVIRONMENT

ARL:UT
AS-83-901
DPK-GA
8-8-83

a deep ocean, the difference in arrival times between rays that differ by one in the number of bottom bounces can be on the order of 2.5 sec. Thus, it is possible, as illustrated in Fig. 2(a), to identify groups of arrivals according to their bottom bounce number. The first group of signals in Fig. 2(a) represents energy which did not interact with the bottom. The second group is characterized by a single bottom interaction (SBI). For each successive group of signals, the number of bottom interactions increases by one. Finally, Fig. 2(b) illustrates a high resolution plot of the SBI arrivals. This report considers only the SBI arrivals since their analysis is simple. These SBIs reveal some of the important features of acoustic interaction with the ocean bottom in an abyssal plains environment.

Figure 3 displays the actual received time series due to SBI arrivals for three ranges. For each graph, the largest received pressure has been set to unity. For the time series corresponding to the range of 23.2 km, one observes three primary arrival structures followed by a long tail of smaller arrivals. As the range decreases, the separate primary arrivals appear to "stretch out" and become more structured. Also, the temporal distance between the primary arrival patterns increases.

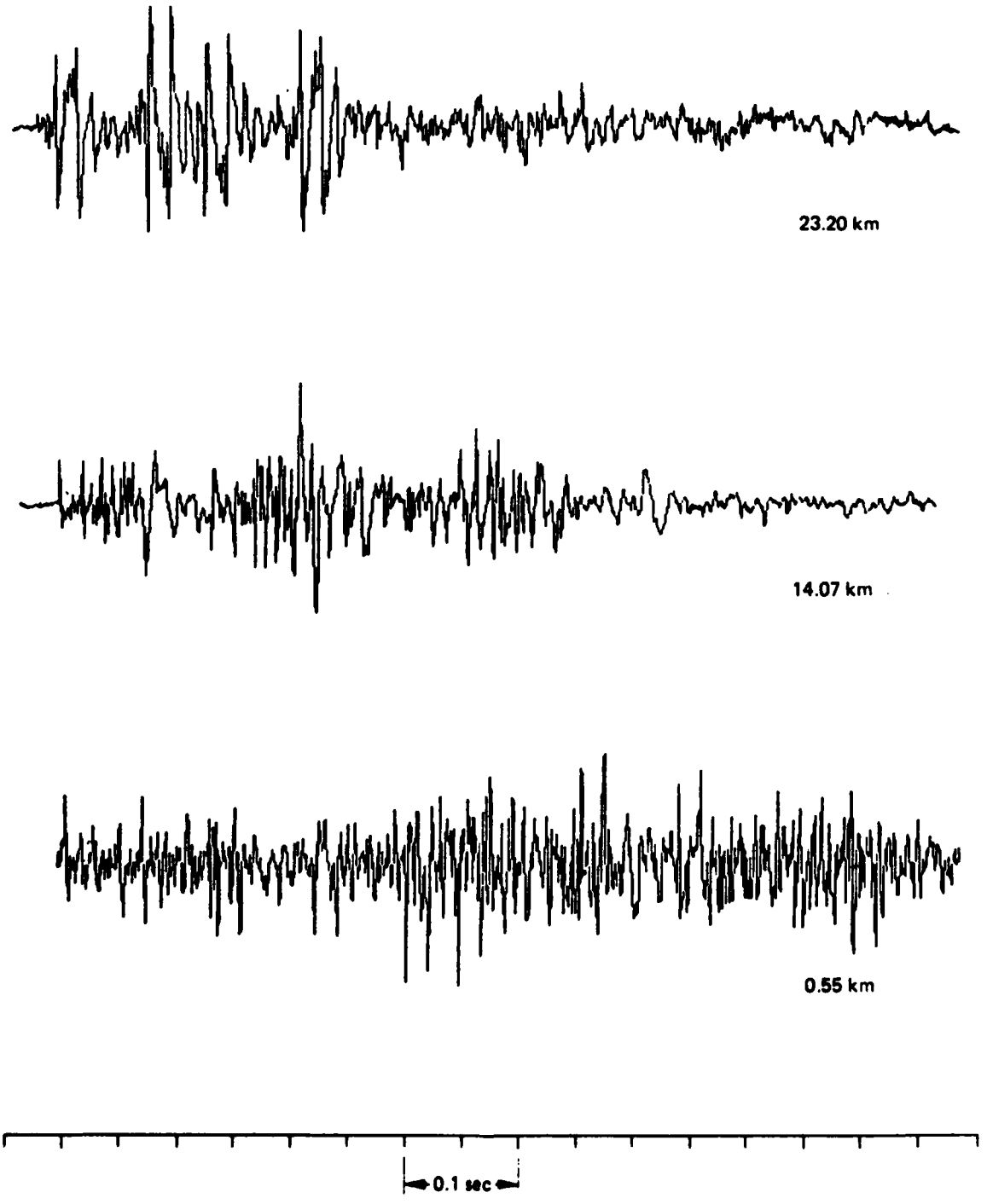

FIGURE 3
EXAMPLE OF SINGLE BOTTOM INTERACTION (SBI) EXPERIMENTAL DATA

ARL:UT
AS-83-902
DPK - GA
8 - 8 - 83

III. THE RANGE INVARIANT, SINGLE SEDIMENT LAYER RAY MODEL

Acoustical radiation generated by an SUS charge explosion in a deep ocean environment can be viewed, in a mechanical sense, as energy propagating along frequency independent trajectories called eigenrays. These rays, which connect the source and receiver, are determined using Snell's law and by allowing for reflections off the boundaries forming the ocean waveguide. Loss mechanisms in the model include reflection and transmission at the boundaries, geometrical spreading of the rays, and the continuous absorption of energy along the ray paths within the sediment. Attenuation within the water column at low frequencies is negligible. Once the rays are found and the losses and phase shifts accounted for, the basic mathematical tool used in the construction of the received signal is the Fourier transform and its properties, especially the convolution theorem.

An accurate prediction of the received signal relies on two basic ingredients: correct modeling of the source explosion and an adequate Green's function to represent the ocean environment. Modeling the source is by far the easier of the two. The acoustic signal generated by an underwater TNT explosion depends mainly on the depth of the explosion and the mass of the explosive materials. However, the Green's function must contain all the properties of the ocean environment, namely the structure of the water column and the geoacoustic

profile. It is assumed that the ocean bottom can be represented by a range invariant, single sediment layer geoacoustic profile.

A. Source Explosion

Equation 1 is the pressure signature of an underwater TNT charge explosion[5]

$$i(t) = P_o \exp\left\{-\frac{t}{t_o}\right\} U(t) + \sum_{i=1}^{N} P_i \left[\exp\left\{-\left|\frac{t-\tau_{Bi}}{\tau_i}\right|\right\}\right.$$

$$\left. + P_{ii} \sin\left[\pi\left(\frac{t-\tau_{Bi-1}}{\tau_{Bi}-\tau_{Bi-1}}\right)\right]\left(U(t-\tau_{Bi-1}) - U(t-\tau_{Bi})\right)\right] , \quad (1)$$

where

$$\tau_{B_o} = 0$$

$$U(t-t') = \begin{cases} 0 & t<t' \\ 1 & t>t' \end{cases}$$

and

$$P_{ii} = -\frac{\pi}{2}\frac{P_{i-1}\tau_{i-1} + P_i\tau_i}{\tau_{Bi} - \tau_{Bi-1}} .$$

Initially, the explosion produces a strong pulse whose amplitude decreases exponentially with time. This initial disturbance is followed by smaller pulses of decreasing amplitude. These pulses, known as bubble pulses, are the product of the oscillations of the hot gases formed by the explosion. Since the hydrostatic pressure provides the

restoring force, the time interval between the pulses is a function of depth. Here P_0 is the initial pulse pressure, and τ_0 its decay constant, P_i is the ith bubble pulse peak pressure, τ_i is the ith bubble pulse rise and decay time constant, τ_{Bi} is the ith bubble pulse period, and P_{ii} is the minimum pressure between pulse i and i-1. The relationship of these parameters to the weight of the charge and depth of the explosion has been determined from both observation and theoretical analysis.[5,6] Figure 4 is the pressure signature of an 816 g TNT explosion at a depth of 244 m, given by Eq. (1), and Fig. 5 is the power spectrum in 1 Hz bands. The time difference between the initial impulse and the first bubble pulse is about 20 msec. The advantage of using explosive charges as acoustical sources is that the explosions produce a broad band of frequencies, allowing one to study the frequency dependence of the interaction of sound with the ocean bottom.

B. Range Invariant, Single Layer Geoacoustic Profile

If one could know all of the environmental parameters, it would be possible, at least in principle, to accurately predict the received pressure time series. Precise information about a particular ocean environment, especially the bottom structure, is rare. In practice, one initially adopts a simplified geoacoustic profile. A valid assumption for many deep ocean environments is that the geoacoustic parameters are only a function of the vertical coordinate (z). This condition is known as range invariance and it greatly simplifies the mathematics needed to

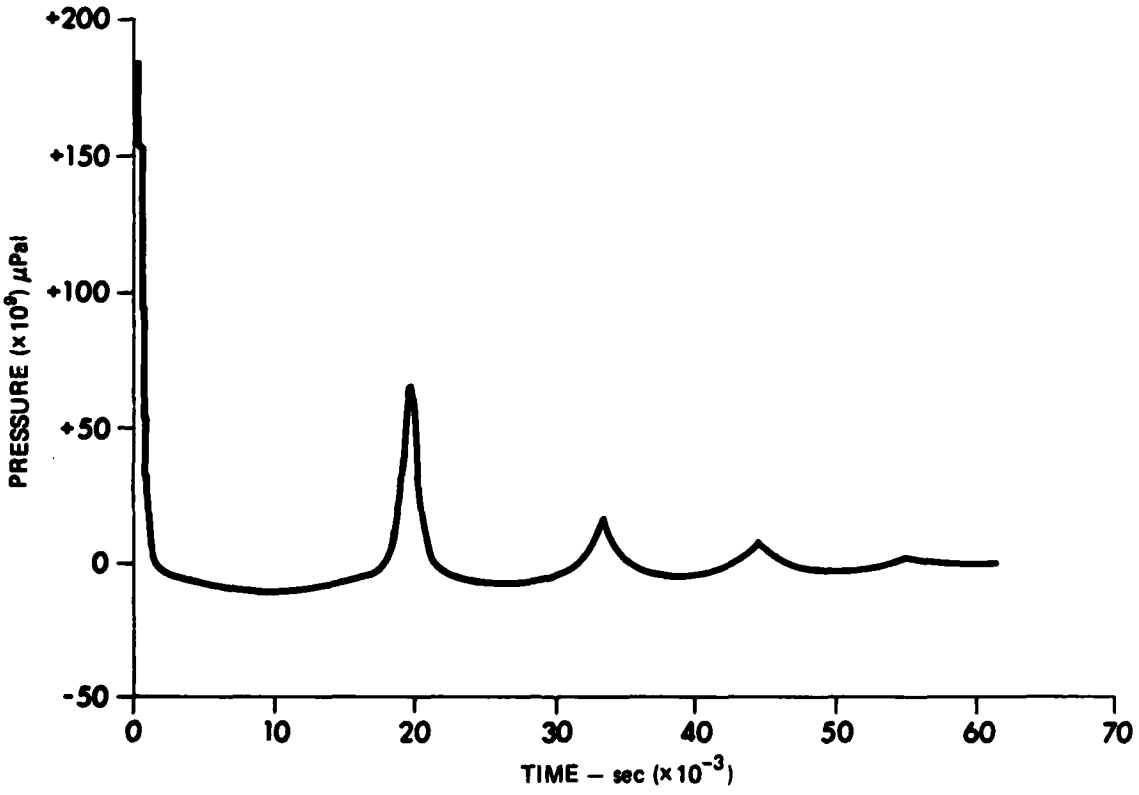

FIGURE 4
PRESSURE SIGNATURE OF 816 g TNT UNDERWATER EXPLOSION AT A DEPTH OF 244 m

ARL:UT
AS-83-903
DPK - GA
8 - 8 - 83

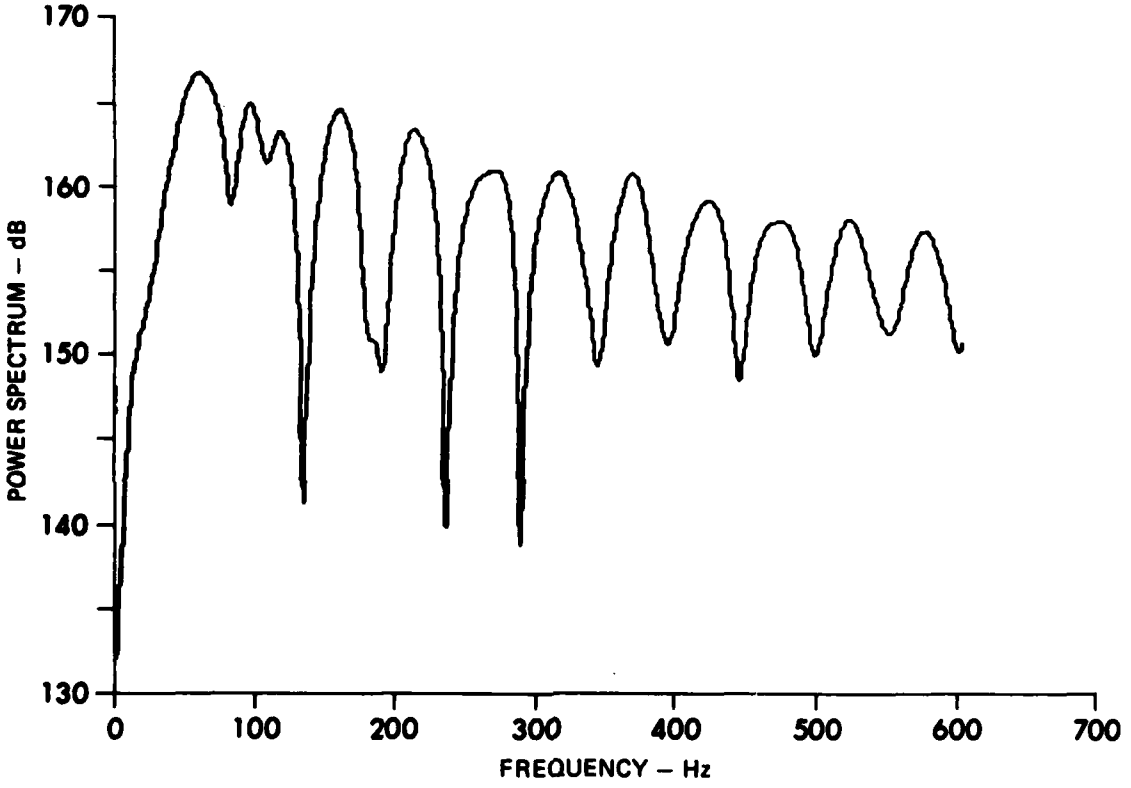

FIGURE 5
POWER SPECTRUM OF 816 g TNT UNDERWATER EXPLOSION AT A DEPTH OF 244 m

ARL:UT
AS-83-904
DPK - GA
8 - 8 - 83

represent the Green's function for the wave equation. Additional assumptions concerning the nature of the depth dependence of the geoacoustic parameters, such as linearity, further simplify the calculations.

Figure 6 illustrates the velocity and layering structure of the range invariant environmental profile. It is assumed that the ocean environment can be represented by a water column (a perfect fluid) overlying a single sediment layer covering a flat basaltic basement. Later we will present evidence that the single layer assumption is incorrect. The water-air interface is flat and, because of the large impedance difference, no significant amount of acoustic energy can be transmitted into the atmosphere. The sediment sound speed structure is assumed to be linear. An initial estimate of the ratio of the top sediment sound speed to bottom water sound speed and the sediment compressional sound speed gradient was obtained from Hamilton's work on ocean geoacoustic modeling.[2] The sediment is considered a fluid, except at the sediment-basement interface. Here, a significant amount of compressional to shear coupling can occur. In addition to a bottom sediment shear speed, basement compressional and shear speeds were also obtained from Hamilton's work. It is assumed that the sound speed gradient of basalt is zero; thus any energy entering the basement can never return to the water column to contribute to the received signal. Later, we will discuss the possible effects of a nonzero compressional gradient in the basement.

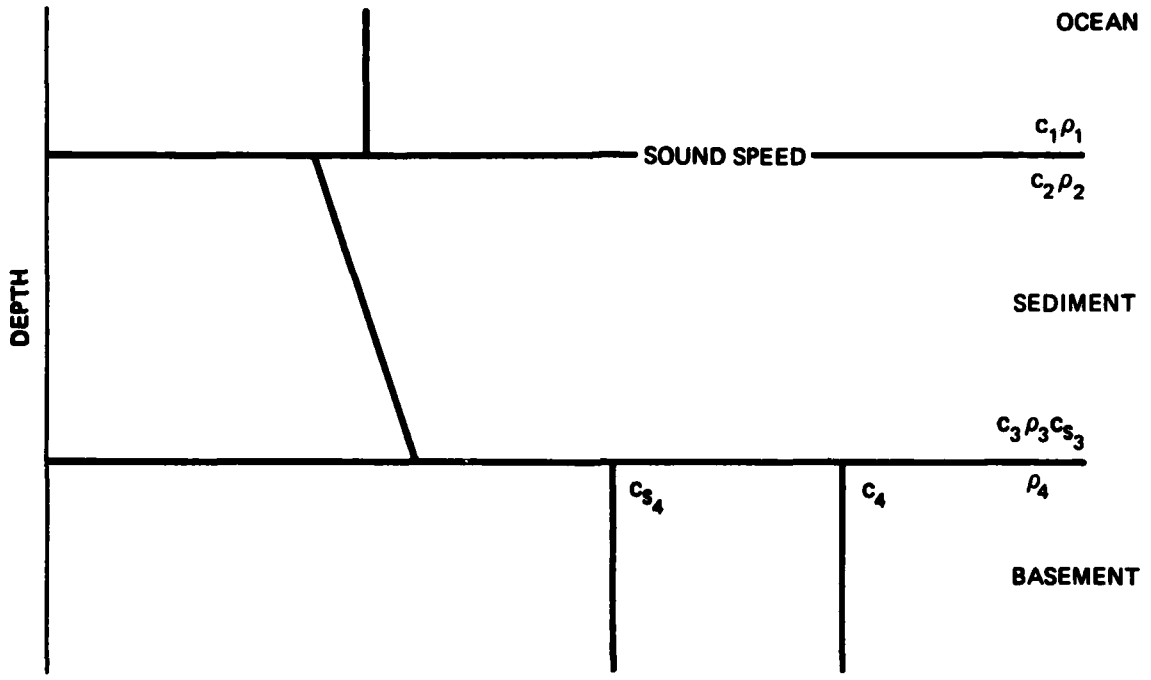

FIGURE 6
SOUND SPEED AND LAYER STRUCTURE OF RANGE INVARIANT SINGLE SEDIMENT LAYER GEOACOUSTIC PROFILE

ARL:UT
AS-83-905
DPK - GA
8 - 8 - 83

The attenuation and density profiles of the sediment are also assumed to be linear with increasing depth. Again, an initial estimate of the corresponding parameters were obtained from Hamilton's work.[2] One introduces a sediment density gradient to calculate the bottom sediment density, which is needed to calculate the sediment-basement interface reflection coefficient. The frequency dependence of the absorption in the sediment is assumed to be linear.[2] The fraction of compressional energy converted into upward going shear energy at the basement is assumed to be completely absorbed within the sediment since the sediment shear attenuation is about a thousand times as great as the compressional attenuation.[2]

C. Ray Theoretical Green's Construction of the Received Signal

In order to understand how ray theory can be used to predict the received pressure due to an arbitrary point source I(t), we begin with the two-dimensional inhomogeneous linear wave equation satisfied in the range invariant environment previously described

$$\nabla^2 P(\vec{r},t) - \frac{1}{c^2(\vec{r})} \frac{\partial^2 P(\vec{r},t)}{\partial t^2} = -I(t)\ \delta(\vec{r}) \quad . \qquad (2)$$

Here ∇^2 is the two-dimensional Laplacian operator in the range-depth plane and $\delta(r)$ is the Dirac delta function. P is the pressure, a continuous function of the position vector (r) and time (t), and C is the

sound speed. Attenuation is introduced later in an ad hoc fashion. Instead of solving Eq. (2) directly, we decompose the source into a number (n) of concentrated sources for various values of t and consider the simpler problem of solving Eq. (2) when I is a unit source concentrated at t=t', i.e., we solve

$$\nabla^2 G(\vec{r},t-t') - \frac{1}{c^2(\vec{r})} \frac{\partial^2 G(\vec{r},t-t')}{\partial t^2} = -\delta(t-t')\ \delta(\vec{r}) \quad . \tag{3}$$

G is called the Green's function or the impulse response for the linear wave equation and here has units of inverse time. Since G is the response due to a unit source concentrated at t', we demand that G be a real function. From the principle of superposition, the received signal at t due to all the concentrated sources is

$$P(\vec{r},t) = \sum_{i=1}^{n} G(\vec{r},t-t_i')\ I(t_i')\Delta t' \quad . \tag{4}$$

In the limit that n becomes very large, we can replace the summation by an integral, namely

$$P(\vec{r},t) = \int_{-\infty}^{\infty} G(\vec{r},t-t')\ I(t')dt' \quad . \tag{5}$$

The Fourier convolution theorem tells us that this is equivalent to

$$P(\vec{r},t) = \int_{-\infty}^{\infty} e^{2\pi i f t}\ \tilde{G}(\vec{r},t)\ \tilde{I}(f)df \quad , \tag{6}$$

where

$$\tilde{G}(\vec{r},t) = \int_{-\infty}^{\infty} e^{-2\pi i f t}\, G(\vec{r},t)dt \quad ,$$

and

$$\tilde{I}(f) = \int_{-\infty}^{\infty} e^{-2\pi i f t}\, I(t)dt \quad .$$

$\tilde{G}$, the Fourier transform of the impulse response, is known as the frequency response or the Green's function for the Helmholtz equation. The Helmholtz equation is obtained by taking the Fourier transform of Eq. (2) and then twice integrating by parts over all t, assuming P and dP/dt vanish sufficiently fast as $t \to \pm\infty$. In general, $\tilde{G}$ is a complex function.

We now assume that the acoustic energy propagates from source to receiver via trajectories called eigenrays. The trajectories of the eigenrays are frequency independent, and are determined completely by the sound speed structure via Snell's law and the boundaries forming the waveguide. This picture emerges from an asymptotic approximation to the wave equation. One may represent the solution to the wave equation in terms of a Feynman path integral, a superposition of an infinite number of continuous paths with end points at the source and receiver. Each path contributes equally to the observed pressure field but with a different phase. The phase for each path is the ratio of the value of the action functional for the path to the acoustic wavelength. In the

high frequency limit, all paths cancel out except those determined by Snell's law.[7,8] In the transition to ray theory, we simply rewrite Eq. (5) as

$$P(t) = \int_{-\infty}^{\infty} g(t-t')\ I(t')dt' \quad , \tag{7}$$

where g is the ray theoretical Green's function.

Figure 7(a) illustrates three classes of possible SBI eigenrays. The ray which reflects off the water-sediment interface will, from this point on, be referred to as the specular ray. The sediment penetrating rays are classified as refracting or basement reflecting. Allowing for reflection at the water-air interface, each class of rays includes four types, as illustrated in Fig. 7(b). Usually for a deep water environment, there are eight SBI eigenrays between source and receiver, four of which bounce off the water-sediment interface and four which penetrate the sediment. The four sediment rays are usually either all refracted by the increasing sound speed or all reflected from the basement. For large ranges, the sediment rays are of a refracting type. As the range decreases one finds a range, say the critical range, where some of the rays become a basement interacting type. Finally, for some range less than the critical range, all of the sediment rays become basement interacting.

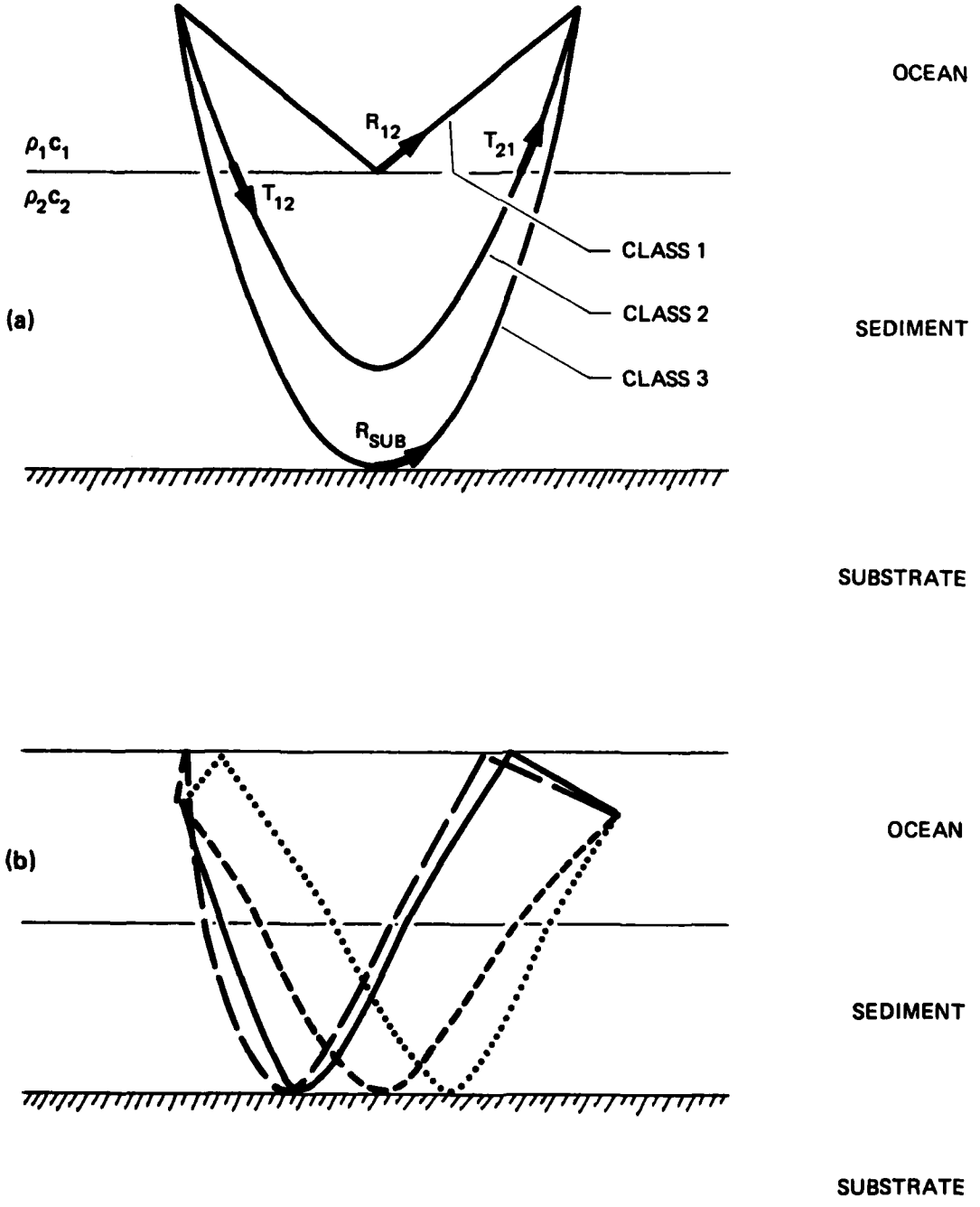

FIGURE 7
SINGLE BOTTOM BOUNCE EIGENRAYS

ARL:UT
AS-83-906
DPK - GA
8 - 8 - 83

The eigenray theoretical Green's function for the range invariant ocean environment is

$$g(t) = \int_{-\infty}^{\infty} e^{2\pi i f t}\, \tilde{g}(f)\, df \quad , \tag{8}$$

where the eigenray frequency response $\tilde{g}(f)$ is a superposition of all the eigenrays. Since we demand that $g(t)$ be real, we easily obtain from Eq. (8) that $\tilde{g}(f)^* = \tilde{g}(-f)$. This constraint on the frequency response is known as the reality condition. A representation of the frequency response is

$$\tilde{g}(f) = \sum_{j=1}^{n} P_j Q_j\, e^{-i\phi_j}\, e^{-2\pi i f t_j}\, e^{-2\pi |f| A_j} \quad . \tag{9}$$

Here P_j, ϕ_j, and t_j are the geometrical divergence, the frequency independent phase, and the travel time for the jth ray, respectively. Q_j represents the accumulation of interface reflection and transmission coefficients and $2\pi|f|A_j$ is the total absorption accumulated along the ray path in the sediment for the jth ray. The absolute value of the frequency is needed in the absorption term in Eq. (9) so that $\tilde{g}(f)$ satisfies the reality condition.

The effective interface reflection coefficient for the jth ray is assumed to be related to the complex plane wave reflection and

transmission coefficients. For a ray which reflects off the water-sediment interface, Q_j is simply given by the fluid-fluid reflection coefficient (coupling to shear waves can be neglected[9])

$$R_{12} = \frac{\rho_2\kappa_1 - \rho_1\kappa_2}{\rho_2\kappa_1 + \rho_1\kappa_2} \quad , \tag{10}$$

where κ_1 and κ_2 are the vertical wave numbers

$$\kappa_1 = \frac{2\pi f}{c_1} \sin\theta_1$$

and

$$\kappa_2 = \frac{2\pi f}{c_2} \left[1 - \left(\frac{c_2}{c_1}\right)^2 \cos^2\theta_1\right]^{1/2} \quad .$$

Here the subscripts 1 and 2 refer to the bottom of the water column and the top of the sediment, respectively. θ is the grazing angle measured from the horizontal at the water-sediment interface and ρ represents the density. For $(c_2/c_1)\cos\theta_1 > 1$, one has total reflection and R_{12} becomes

$$R_{12} = -\exp\left[-2i \tan^{-1}(\rho_2\kappa_1/-i\rho_1\kappa_2)\right] \quad . \tag{11}$$

For a ray which refracts within the sediment, Q_j is given by

$$Q_j = T_{12}T_{21} \quad , \tag{12}$$

where T_{ij} is the transmission coefficient for passing from medium i into medium j,

$$T_{ij} = \frac{2\rho_i \kappa_j}{\rho_j \kappa_i + \rho_i \kappa_j} \quad .$$

For a ray which reflects off the sediment-basement interface, we have $Q_j = T_{12}\, T_{21}\, R_{sub}$, where R_{sub} is the plane wave reflection coefficient for the compressional wave at the sediment-basement interface. R_{sub} includes the decrease in the magnitude and the change in phase of the compressional reflection coefficient due to compressional-shear coupling.[9] This represents a loss mechanism because it is assumed that all of the sediment shear energy created at the basement is absorbed within the sediment.

It is further assumed that the total intrinsic absorption within the sediment is linearly proportional to the frequency.[2] The total sediment absorption along the jth ray path in the sediment is $2\pi|f|A_j$, where

$$A_j = \frac{\ell n(10)}{4\pi \times 10^4}\; 2\int_0^Z \frac{\alpha(z')dz'}{\sqrt{1 - a_j^2 c^2(z')}} \quad . \tag{13}$$

Here Z is the turning depth of the ray or the depth of the sediment, depending on whether the ray is a refracting or basement reflecting type. $\alpha(z)$ is the linear attenuation profile in units of dB/m-kHz. c is the real part of the sediment compressional sound speed profile and

$a_j = (\cos \theta_j)/c_j$ the Snell's invariant for the jth ray. Equation (13) is derived in Appendix A. It is important to note that the physics of the intrinsic attenuation within the sediment is not well understood.[2] The attenuation profile introduced here represents the increase in attenuation with depth observed in deep sea sediments.[2]

The frequency independent phase shift ϕj is determined in the following manner. For a single bounce off the water-air interface, a phase of $+\pi$ is assigned. This result comes from the demand of continuity of pressure across the interface, i.e., the incident pressure plus the reflected pressure must equal to the transmitted pressure. Since the transmitted pressure is approximately zero, the reflected pressure is the negative of the incident pressure. This is accomplished by setting $\phi=\pi$, since $e^{-i\pi}=-1$. For a reflection off the water-sediment or sediment-basement interface, a phase change of 0 is assigned since the actual phase change of the ray is contained within the reflection coefficient. Ray theory is a WKB approximation to the wave equation. In one dimension, this solution breaks down at the classical turning point. Assuming that the potential is linear in the region near the turning point, the solutions on either side of the turning point are Airy functions.[10] The asymptotic forms of Airy functions show that a ray passing through the turning point acquires a $-\pi/2$ phase shift. In two dimensions, instead of breaking down at the turning point, the WKB approximation breaks down at a caustic line. A caustic is a point where rays intersect, mathematically causing a point where the intensity is infinite. The line which connects these points is known as a caustic

line. It is also found that a ray which grazes a caustic acquires a $-\pi/2$ phase shift.[11,12] Since all the refracting SBI eigenrays, for the sediment sound speed profile given in Table I, combined with the measured water sound speed profile, graze a sediment caustic line, a phase shift of $-\pi/2$ is assigned to them.

D. Causality Considerations

Since the environment considered here has an absorbing medium, namely the sediment layer, we briefly discuss the subject of causality. Equation (7) as it stands is incorrect because it says that the received acoustic signal at time t is not only composed of events prior to t but also events after t. To correct this, we demand that

$$P(t) = \int_{-\infty}^{\infty} g(t-t')\ I(t')dt' \quad , \tag{14}$$

where

$$g(\tau) = 0 \quad \tau<0 \quad . \tag{15}$$

This is known as the causality requirement.

To calculate the impulse response, we take the inverse transform of $\tilde{g}$.

TABLE I

RANGE INVARIANT, SINGLE SEDIMENT LAYER
GEOACOUSTIC PROFILE FOR EXERCISE AREA

Layer	Depth (m)	Sound Speed (m/sec) V_P	V_S	Attenuation (dB/m-kHz) k_p	k_s	Density (g/cm^3)
Bottom Water	4268	1528.2	0.0	0.0	0.0	1.05
Sediment (Silty Clay)	4268	1514.0	0.0	0.2	15.0	1.35
	4468	1760.0	400.0	0.04	25.0	1.6
Basement Rock	4468	5500.0	2700.0	0.03	0.07	2.62

$$g(\tau) = \int_{-\infty}^{\infty} \tilde{g}(f)\, e^{2\pi i f\tau}\, df$$

$$= \sum_{j=1}^{n} \int_{-\infty}^{\infty} P_j Q_j\, e^{-i\phi_j}\, e^{-2\pi i f t_j}\, e^{-2\pi |f| A_j}\, e^{2\pi i f\tau}\, df \qquad . \quad (16)$$

Using the reality condition of $\tilde{g}(f)$, we find that

$$g(\tau) = \sum_{j=1}^{n} P_j \int_{-\infty}^{\infty} df \left[e^{-2\pi f A_j} \left(\xi_j^*\, e^{-2\pi i f(\tau - t_j)} + \xi_j\, e^{2\pi i f(\tau - t_j)} \right) \right] \quad , \qquad (17)$$

where we have defined

$$\xi_j \equiv e^{-i\phi_j} Q_j \qquad .$$

The simple integration and a little algebra yields

$$g(\tau) = \frac{1}{\pi} \sum_{j=1}^{n} P_j \left[\frac{A_j \,\mathrm{Re}\, \xi_j + (\tau - t_j)\, \mathrm{Im}\, \xi_j}{A_j^2 + (\tau - t_j)^2} \right] \qquad . \qquad (18)$$

We see that $g(\tau)$ is nonzero for $\tau<0$ which, from previous arguments, says that $g(\tau)$ violates causality.

The reason that $g(\tau)$ violates causality is that the frequency response $\tilde{g}(f)$ is a nonanalytic function in the complex plane. The real and imaginary parts of the function $e^{-|Z|A}$ do not satisfy the Cauchy-

Riemann equation. One can use Cauchy's theorem to show that the real and imaginary parts of $\tilde{g}(f)$ do not satisfy a Hilbert transform relationship. Classical dispersion theory tells us that the real and imaginary part of $\tilde{g}(f)$ must satisfy a Hilbert transform relation in order to preserve causality.[13] Thus, the Green's function $g(\tau)$ in Eq. (18) is noncausal because the reality condition forced the frequency response to be nonanalytic in the complex plane. In order to correct this problem, one would have to find a dispersion relationship between the sound speed and the absorption in the sediment. This is a difficult task to perform and many researchers have put much effort into this most interesting problem.[14,15] Here, we simply ignore the problem because numerical calculations show that, for the problem we are considering, the amplitude of the noncausal arrivals are two orders of magnitude below the physical arrivals and hence are not a major factor in our analysis.

E. Numerical Implementation

We now summarize the numerical implementation of the range invariant ray model. The sound speed structure of the water column and the sediment along with the geometry of the source and receiver are input to a computer program which finds the SBI eigenrays.[16] In addition to the sound speed profile of the sediment, the density and attenuation structure are used to determine the accumulative interface reflection coefficient and attenuation along the path for each eigenray. The single layer, range invariant geoacoustic profile obtained from Hamilton's work[2] is given in Table I. This information is used to construct (Eq. (9)) the

ray frequency response $\tilde{g}(f)$. The inverse Fourier transform of the product of $\tilde{g}(f)$ and the source spectrum is performed numerically using the fast Fourier transform.[17] According to the convolution theorem of Fourier transforms, this gives us the desired result: the received pressure time series due to a SUS charge explosion in the ocean environment.

Figure 8 is an example of the received signal predicted by the range invariant single layer ray model for the geoacoustic parameters listed in Table I. Here, the range is 25.92 km and the depths of the source and the receiver are 244 m and 205 m, respectively. In order to understand the characteristics of the simulated waveform, the signals due to the individual eigenrays are shown. The sound speed structure and the geometry are such that the theory predicts that the sediment penetrating rays are of a refracting type. First note that the amplitude of the signals due to the specular rays (Fig. 8(a)) are an order of magnitude below those due to the sediment penetrating rays (Figs. 8(b)-(e)). The reason that the refracting rays have a much larger contribution is that the magnitude of the reflection coefficient for the specular rays is on the order of 0.1, whereas the magnitude of the transmission coefficient for the refracting rays is about 0.9. Further, for the range in question, the refracting rays do not penetrate very far into the sediment, thus accumulating a small attenuation. It is important to note that as the range decreases the sediment rays will travel deeper into the sediment, thus losing more energy to the environment. Thus, we expect that as the range decreases, the amplitudes of the specular arrivals will

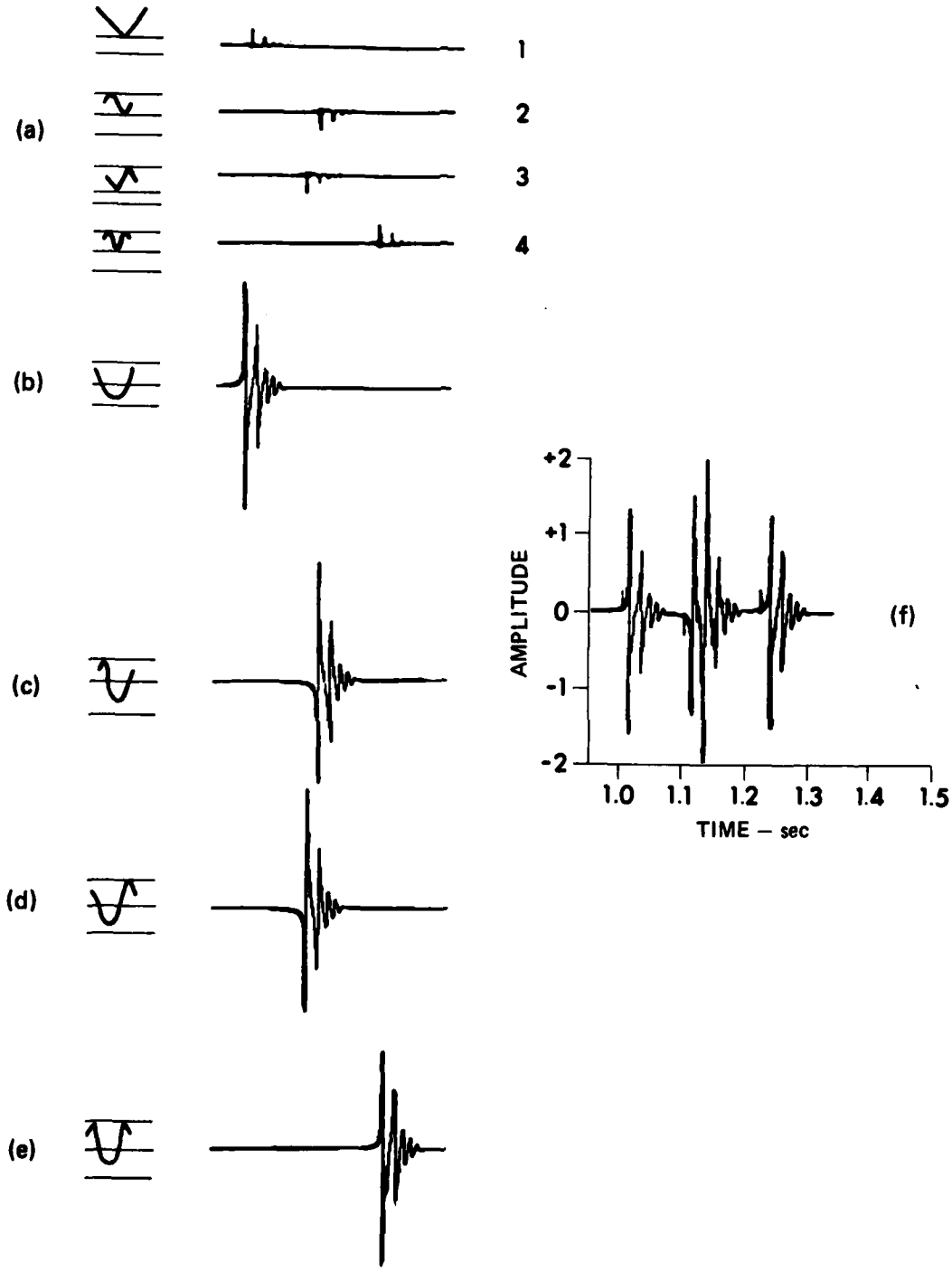

FIGURE 8
EXAMPLE OF SIMULATED TIME SERIES

ARL:UT
AS-83-908
DPK - GA
8 - 8 - 83

increase with respect to the sediment arrivals. Eigenray a1 simply reproduces the source waveform but with a smaller amplitude. Eigenrays a2 and a3 produce an inverted source waveform since the phase of the ray upon reflection at the water-air interface is increased by π, i.e., $e^{-\pi i}=-1$. Since eigenray a4 encounters two water-air reflections, it has the same form as eigenray a1. Eigenrays b-e are of a refracting nature, which means that they acquire a $-\pi/2$ phase shift passing through the sediment since they graze a caustic. For a single refracting ray, the integral of the product of the Green's function in Eq. (18) and a delta function will distort the delta function into its derivative. We can now understand the received waveform due to eigenrays b-e by seeing that the initial pulse and the bubble pulses are distorted into their derivatives because the refracted rays graze the caustic formed in the sediment. A superposition of the signals due to eigenrays a-e gives us the complete received waveform shown in Fig. 8(f).

IV. COMPARISONS OF EXPERIMENTAL AND SIMULATED PRESSURE TIME SERIES

This section presents comparisons of experimental and simulated SBI pressure time series for selected ranges. It is important to remember that our geoacoustic profile is simple in form even though we know that the actual bottom environment is of a complex nature,[2] thus we do not expect exact agreement between theory and experiment. Also, inaccuracies in the measured sound speed profile of the water column and the geometry of the experiment can lead to disagreements between experiment and theory. The idea is to examine the first order disagreements or discrepancies between experiment and theory when they arise and then make educated guesses, in terms of additional geoacoustic parameters, as to their origins.

The comparisons are first presented over a 10-600 Hz frequency band, i.e., the time series contain frequencies that range from 10 to 600 Hz. These broadband comparisons are the primary indicator of how well the range invariant, single layer geoacoustic profile portrays the actual ocean bottom in the exercise area.

A few of the analog recordings will be examined in a 10-1800 Hz band. For these shot experiments, the comparisons, in addition to the broadband comparisons, are made in 100 Hz bands, beginning with the 50-150 Hz band and ending with the 1500-1600 Hz band. These narrowband

comparisons aid in the identification of sediment penetrating arrivals, as opposed to surface or near-surface reflected arrivals, by taking advantage of the frequency dependence of the absorption within the sediment.

During the initial attempts to simulate the measured time series, it was determined that the reported receiver depth (205 m) was incorrect. Figure 9(a) illustrates the comparison of the theoretical and measured SBI time series for a range of 25.92 km. The geoacoustic parameters in Table I, the measured water sound speed profile, and the reported source-receiver geometry were used as input for the range invariant, single layer model. One immediately recognizes the poor agreement. The simulated signals do not have the correct arrival time structure. It was found that this poor agreement between experiment and theory existed for all of the ranges. Reasonable variations of the geoacoustic parameters and the water sound speed profile did not significantly improve the fit to the data, nor did small variations in the range and the ocean depth. It was determined that the reported source depth (244 m) was correct, because both the simulated and the experimental time series showed that the time difference between the initial pulse and first bubble pulse of the first refracted arrival was about 20 msec. (Recall that the time between the initial pulse and first bubble pulse is a function of depth.) Further, variations in the source depth by ±10% made little difference in the shape of the simulated signal. The only other parameter left to vary was the receiver depth. Figure 9(b) shows the comparison for a receiver depth of 154 m. Note

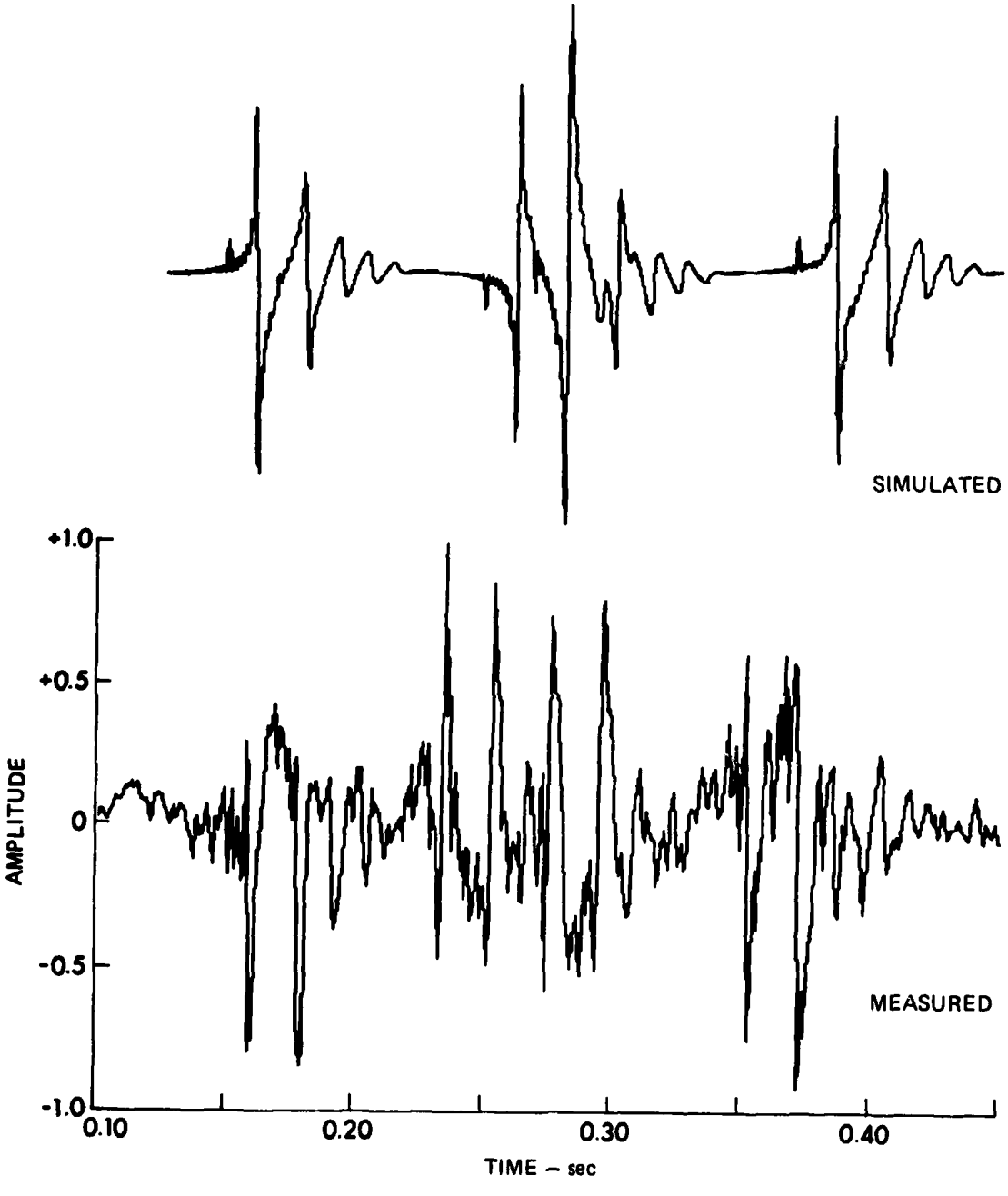

FIGURE 9(a)
COMPARISON OF SIMULATED AND MEASURED SINGLE BOTTOM INTERACTION (SBI) TIME SERIES FOR A RANGE OF 25.92 km
SIMULATED RECEIVER DEPTH: 205 m

ARL:UT
AS-83-1051
DPK - GA
10 - 3 - 83

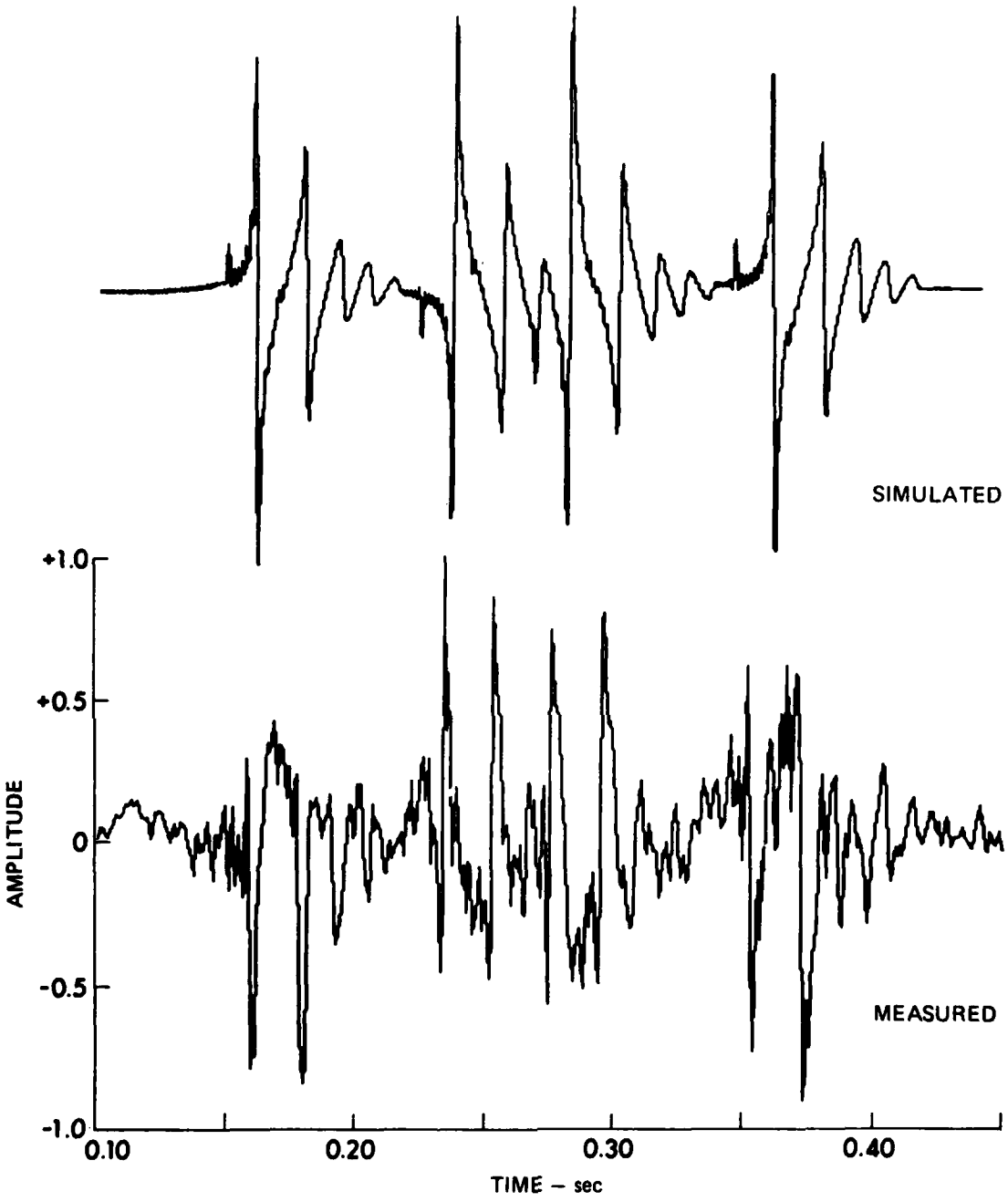

FIGURE 9(b)
COMPARISON OF SIMULATED AND MEASURED SBI TIME SERIES FOR A RANGE OF 25.92 km
SIMULATED RECEIVER DEPTH: 154 m

ARL:UT
AS-83-1052
DPK - GA
10 - 3 - 83

that the agreement is good. Raising the receiver depth has the desired effect of increasing the difference in travel time between the two refracted arrivals which have a single water-air reflection, while at the same time decreasing the difference in travel time between the first and last refracted arrivals. Thus, we conclude that the actual receiver depth is approximately 154 m.

The above conclusion is very disturbing because the intent of this study is to determine the geoacoustic structure of the ocean bottom by a data-model comparison. We now recognize that errors made in the reporting of the geometry of the experiment can have a greater effect on the shape of the simulated signal than variations in the geoacoustic parameters. In attempting to determine the geoacoustic profile from measured time series, one must be aware of these potential errors and try to correct them as they occur.

A. Broadband Comparisons

For a range of 23.2 km, ray theory predicts that, within the range invariant environment presented in Table I, the only sediment penetrating rays are of a refracting nature. Figure 10 presents the 10-600 Hz band comparison in the time domain where the range invariant ray model predicts a nonzero signal (0.18-0.47 sec). Here, the agreement between experiment and theory is very good. The four refracted rays described in the previous section are clearly identified on the basis of the distortion of the initial pulse and bubble pulses caused by the

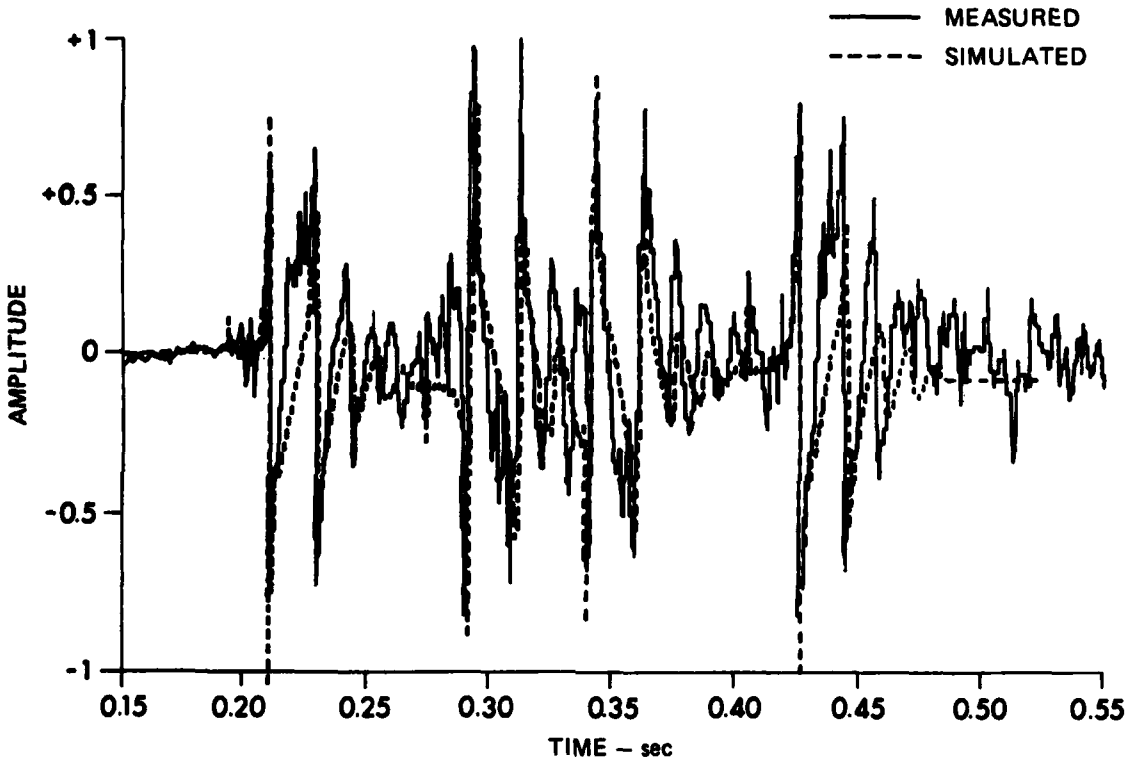

FIGURE 10
COMPARISON OF SIMULATED AND MEASURED SBI TIME SERIES
23.2 km, 10-600 Hz

ARL:UT
AS-83-909
DPK - GA
8 - 8 - 83

caustic line in the sediment. The first refracted arrival in Fig. 10 (0.21-0.27 sec) has no water-air reflections (see Fig. 8(b)). The next two refracted arrivals in Fig. 10 (0.28-0.33 sec and 0.34-0.40 sec) each have a single water-air reflection (see Figs. 8(c) and 8(d)). Finally, the last refracted arrival (0.43-0.47 sec) has two water-air reflections (see Fig. 8(e)).

The comparison in Fig. 10 also identifies surface (water-sediment interface) or near-surface reflected arrivals. The amplitudes of these arrivals are very small compared to those of the refracted arrivals. This is true because the magnitude of the reflection coefficient at the water-sediment interface is on the order of 0.1 and the attenuation of the sediment penetrating rays for this range is small since they do not travel very far into the sediment (approximately 70 m). It is important to keep in mind, however, that we expect this situation to change as the range decreases since the sediment penetrating rays will travel deeper into the sediment. Theoretically, since the phase of the reflection coefficient is small for the specular rays, the corresponding predicted waveforms have the same shape as the source pressure signature. However, the experimental time series in Fig. 10 shows a more complicated arrival structure than that predicted by the single layer model (0.18-0.21 sec), namely, the data has additional high frequency returns between the initial pulse and the first bubble pulse.

Figure 11 illustrates the comparison for the 23.2 km experiment, which includes the time domain beyond which the theory

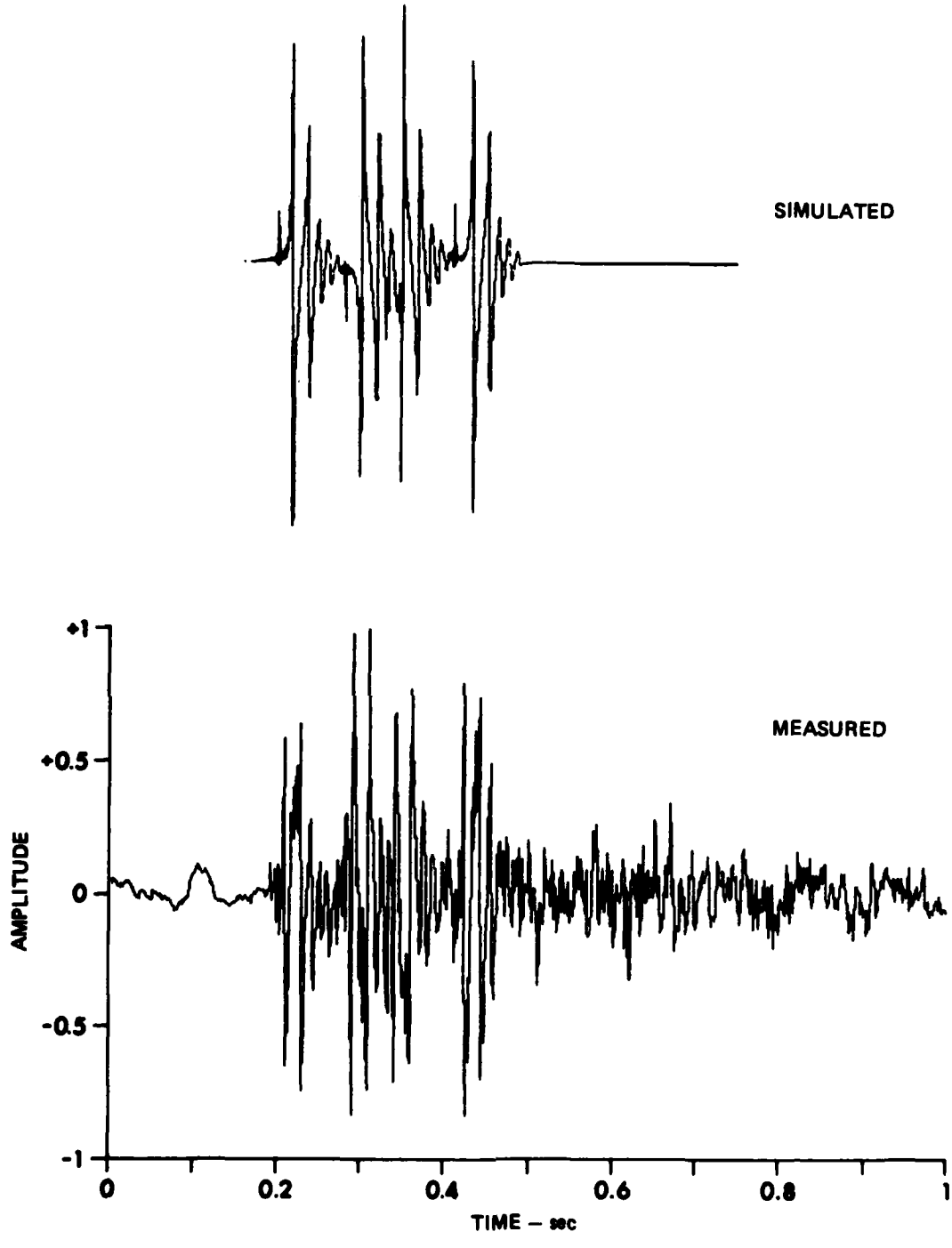

FIGURE 11
COMPARISON OF SIMULATED AND MEASURED SBI TIME SERIES WHICH INCLUDES OBSERVED SECONDARY ARRIVALS
23.2 km, 10-600 Hz

ARL:UT
AS-83-926
DPK - GA
8 - 30 - 83

predicts that there are no received SBI signals. Figure 11 shows experimental signals from 0.5 to 1.0 sec, while the simulated time series predicts no signal in this time domain. The measured signals which arrive after the last predicted arrival (refracted arrival with two water-air reflections) will be referred to as secondary arrivals. The secondary arrivals cannot possibly be the result of rays whose number of interactions with the ocean bottom exceeds one, since the first double bottom interaction arrival is received approximately 1.5 sec after the last major secondary arrival. Secondary arrivals are characteristic of all the SUS data from this experiment.

Figure 12 is the 10-600 Hz band comparison for the 19.53 km experiment. Ray theory predicts that as the range decreases the difference in travel times for the eigenrays increases. As an example, one notices that the theory predicts that the first specular arrival and the first refracted arrival separate from each other to the extent that the first bubble pulse of the specular arrival is not "washed out" by the initial pulse of the refracted arrival. Indeed, this behavior is present in the measured time series from 0.23 to 0.25 sec. One observes, as in the 23.2 km case, that a complex structure is evident between the initial pulse and the first bubble pulse for the specular arrivals. It is not understood why the data show a large difference in the amplitudes of the two refracted arrivals with a single water-air interaction.

Figure 13 presents the broadband comparison for the 15.89 km experiment. As in Figs. 10 and 12, Fig. 13 shows the comparison in the

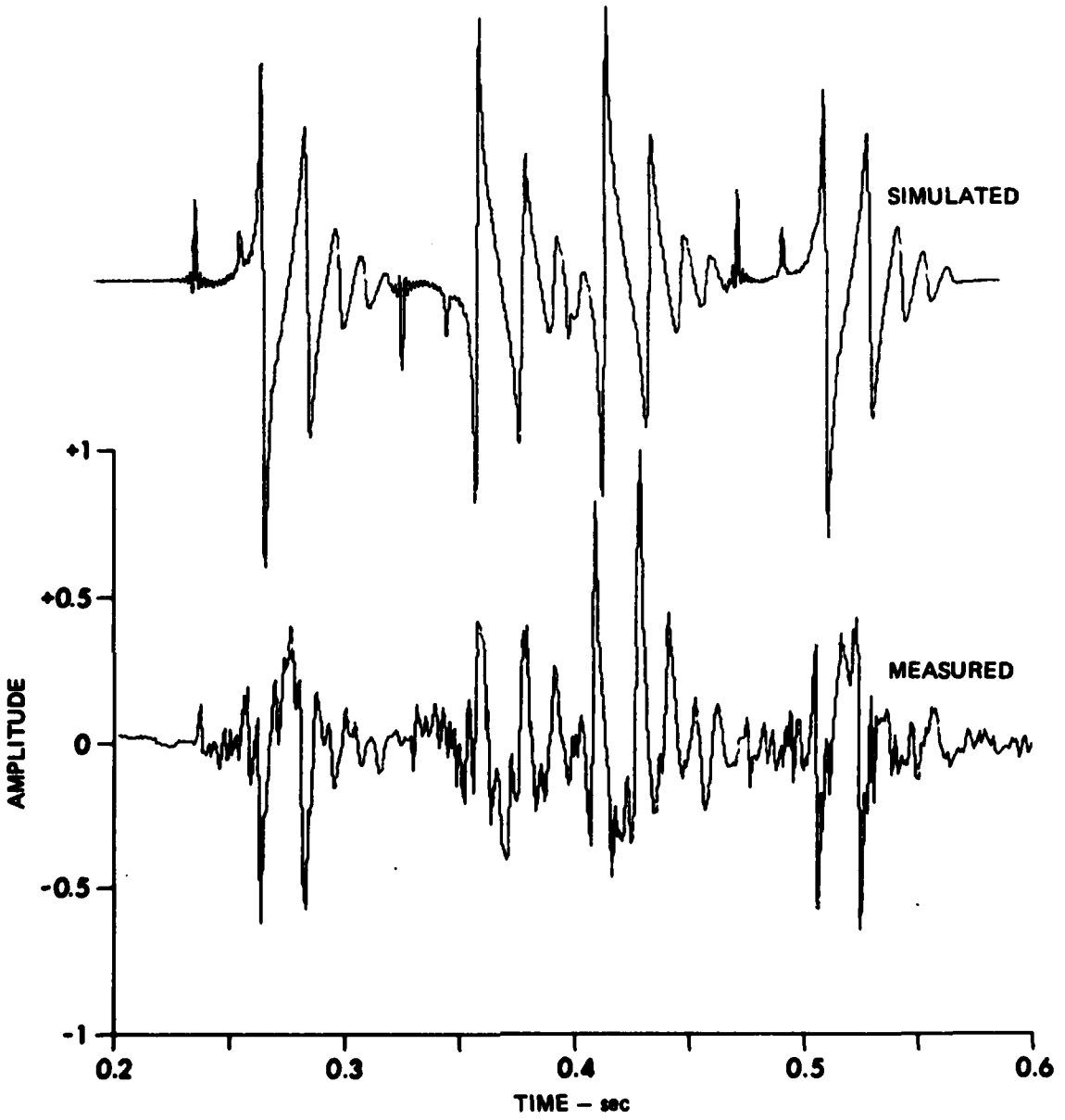

FIGURE 12
COMPARISON OF SIMULATED AND MEASURED SBI TIME SERIES
19.53 km, 10-600 Hz

ARL:UT
AS-83-928
DPK - GA
8 - 30 - 83

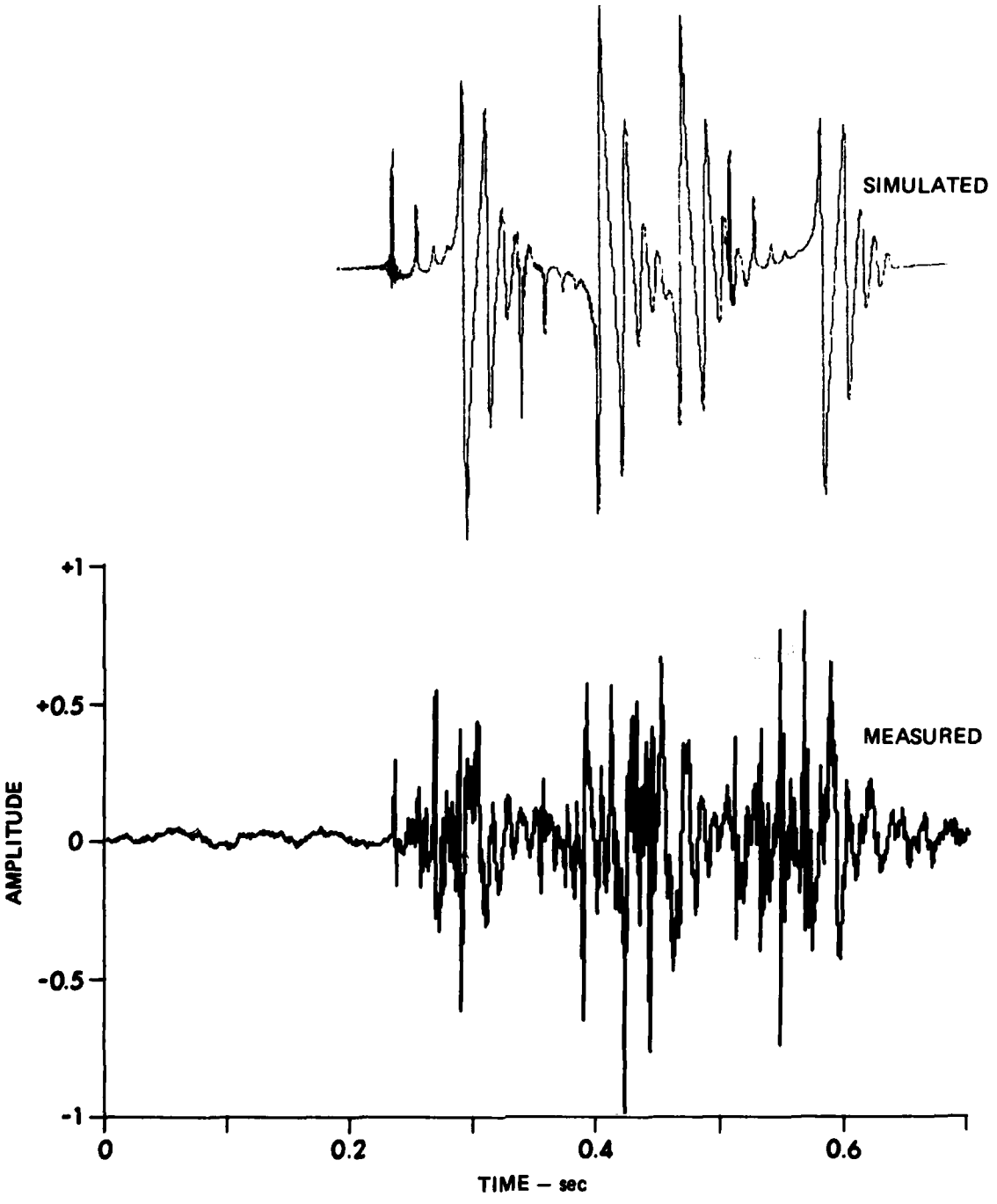

FIGURE 13
COMPARISON OF SIMULATED AND MEASURED SBI TIME SERIES
15.89 km, 10-600 Hz

ARL:UT
AS-83-927
DPK - GA
8 - 30 - 83

time domain where the theory predicts a signal (here 0.24-0.65 sec). The simulated time series accurately predicts the spreading of the SBI arrivals due to a shorter range. The theortical SBI signal lengths for the 23.2 km and 19.53 km experiments were 0.29 sec and 0.32 sec, respectively. The decrease in range to 15.89 km has further increased the signal length to 0.41 sec.

As in the 23.2 km and 19.53 km experiments, ray theory predicts that the sediment penetrating rays are of a refracting nature for the 15.89 km experiment. However, the refracting rays here penetrate the sediment to a depth of about 160 m. The comparison in Fig. 13 clearly shows that the amplitudes of the specular arrivals (0.24-0.27 sec and 0.35-0.38 sec) have increased compared to the 23.2 km and 19.53 km experiments. We expect this to occur since, as the range decreases, the refracting rays penetrate deeper into the sediment, thus acquiring a greater loss due to absorption and geometrical spreading. It follows that the complex structure of the specular arrivals observed for the longer ranges will become a more important part of the time series as the range decreases. The experimental time series clearly illustrate this behavior (0.24-0.27 sec and 0.35-0.38 sec).

For the range of 14.07 km, ray theory predicts that refracted paths are not possible. Instead, all sediment penetrating rays reflect off the sediment-basement interface with grazing angles around 10^{o}. Theoretically, one would expect a significant change in the shape of the received signals in the transition from the refracting to the basement

reflecting case. For the basement reflecting ray, a $-\pi/2$ change in phase would not occur; instead, a different change in phase due to the solid-solid boundary effects at the basement would. Indeed, the general shape of the first basement reflected arrival predicted by the ray model (0.31-0.38 sec) agrees with the experiment (see Fig. 14). Also, the simulated SBI time series accurately predicts that the length of the time series, formed by the primary arrivals, increases from 0.41 sec as in the 15.89 km experiment to approximately 0.5 sec. It follows that the four predicted basement reflected arrivals (see Fig. 7(b)) account for the temporal length of the primary signal. Thus, a decrease in range from 23.2 km to 14.07 km has increased the length of the SBI time series over 200 msec.

We also observe in Fig. 14 that the ratio of the amplitudes of the specular to the basement reflected arrivals is about 0.5. Further, as seen in the previous comparisons, the 14.07 km case shows that the physics contained in the simple plane wave reflection coefficient (Eq. (10)) cannot explain the complicated behavior observed in the 0.23-0.29 sec time interval. First, we see that the theoretical return in the 0.23-0.29 sec time interval is due to a specular eigenray. However, the measured waveform in this time interval shows considerable structure between the simulated strong initial pulse and first bubble pulse. Thin layers beneath the surface could spread the initial strong pulse over a longer time interval than that predicted by the simulated reflection of the water-sediment interface. This can occur because the initial pulse could be carried by more than one specular eigenray.

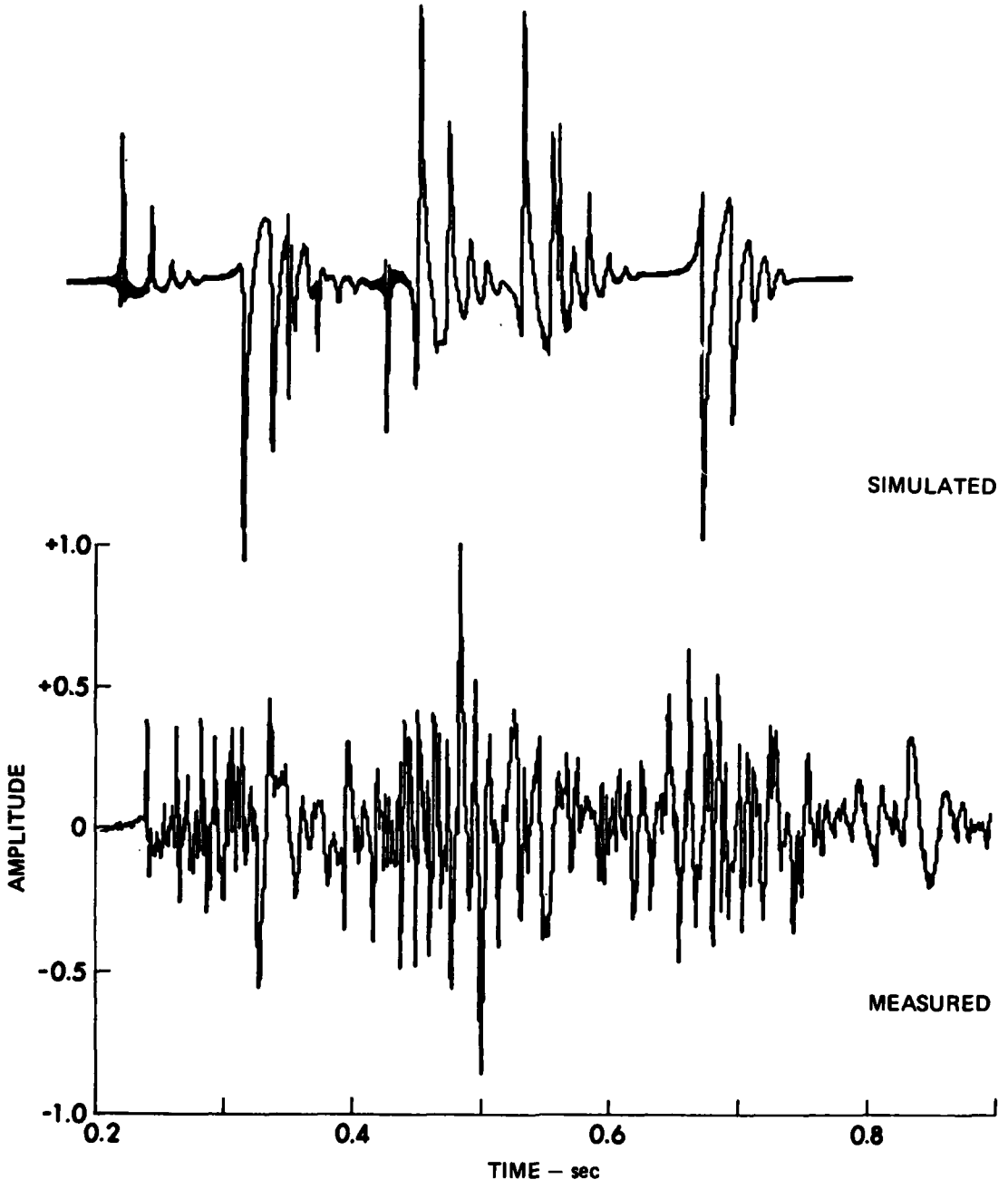

FIGURE 14
COMPARISON OF SIMULATED AND MEASURED SBI TIME SERIES
14.07 km, 10-600 Hz

ARL:UT
AS-83-1053
DPK - GA
10 - 3 - 83

The eigenrays would reflect from different layers producing different travel times.

Figure 15 (0.55 km experiment) clearly shows that the present geoacoustic profile is inadequate for describing the effects of bottom interaction at high grazing angles. It is almost impossible to identify particular arrivals out of the complex mesh of observed arrivals. It is important to note, however, that the time interval of the simulated waveform (about 0.9 sec) is about the same length as the time interval in which the major part of the observed signals arrive.

We have seen that our simple geoacoustic profile is able to explain many of the observed effects of the ocean bottom on sound propagation in an abyssal plains environment. It is surprising that the best fit of the theory to the experiment was obtained using average abyssal plain geoacoustic parameters found in the literature. The range invariant single sediment layer geoacoustic profile correctly predicts that the temporal spread of the primary waveforms increases from 290 msec to about 900 msec as the range is decreased from 23.2 km to 0.55 km. Further, refracted arrivals and basement reflected arrivals were successfully identified.

The broadband comparisons also indicate that the range invariant single layer geoacoustic profile cannot explain the complicated structure of the time series associated with interactions which are due to surface (water-sediment) or near-surface interactions. Also, the

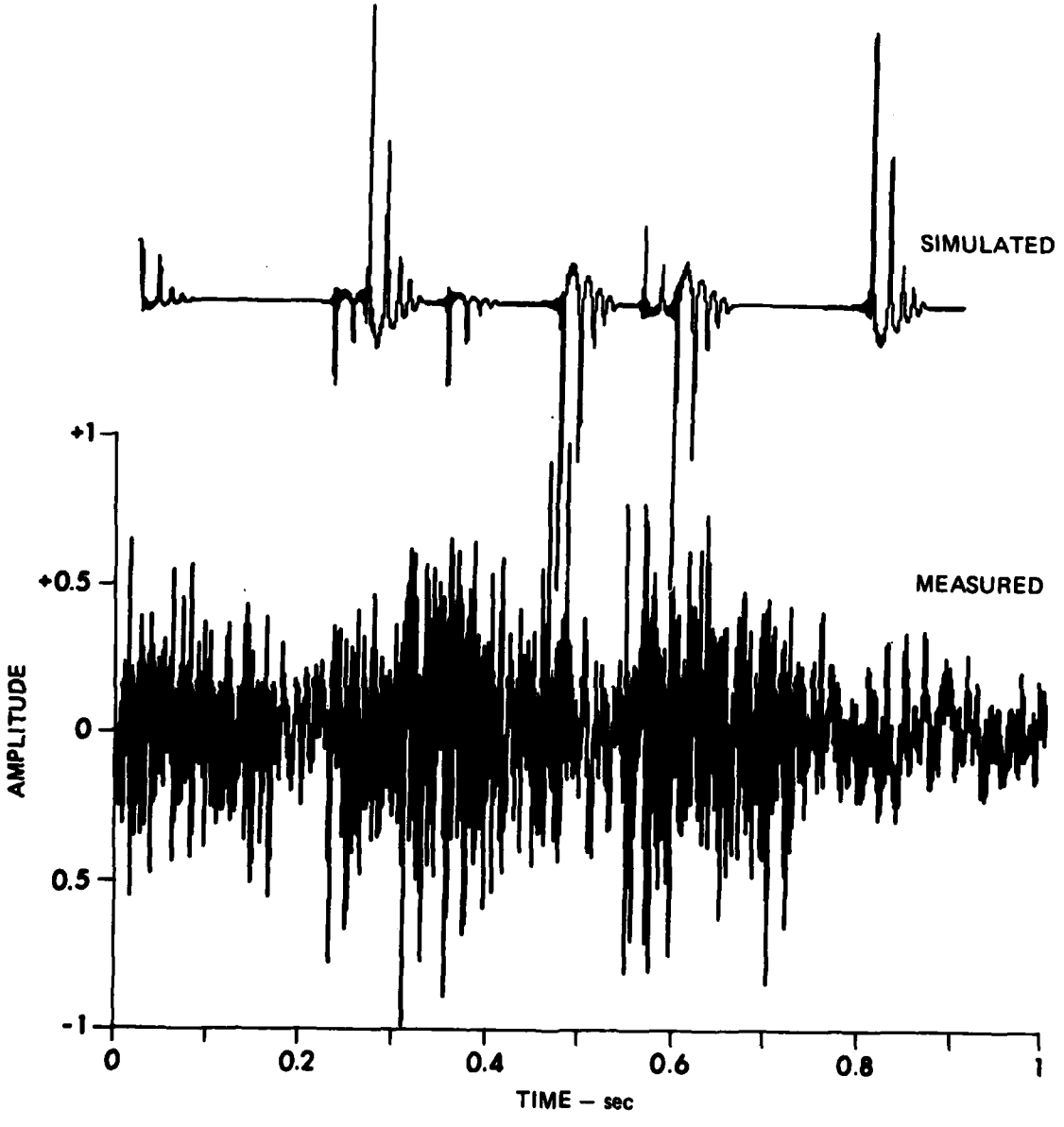

FIGURE 15
COMPARISON OF SIMULATED AND MEASURED SBI TIME SERIES
0.55 km, 10-600 Hz

ARL:UT
AS-83-929
DPK - GA
8 - 30 - 83

profile fails to produce theoretical returns in the time interval of the observed secondary arrivals. In the next section a frequency analysis of the theoretical and experimental waveforms provides information regarding the origin of the discrepancies between theory and experiment.

B. Narrowband Analysis

What information can an examination of the time series comparisons in various frequency bands yield regarding the nature of the acoustic interaction with the ocean bottom? Recall that the complex spectrum of the received signal is the product of the frequency response and the source spectrum. The sediment penetrating components, because of the increase of absorption with frequency, are necessarily dominated by low frequencies. This implies that, if the received spectrum is multiplied by a high pass frequency filter and the inverse transform performed, the dominant contribution to the resulting time series would be from specular rays. Similarly, multiplying the received spectrum by a low pass filter would result in a time series dominated by sediment penetrating rays.[18,19] Thus, a frequency band analysis of the received time series, because of the high frequency energy loss due to sediment absorption, distinguishes between specular and sediment penetrating arrivals. In making comparisons across frequency bands, one must be careful to take into account that the power spectrum for a SUS charge is not constant with frequency and, furthermore, that the average signal-to-noise ratio is not constant within different frequency bands.

Figures 16 and 17(a)-(d) illustrate the above ideas for the 14.07 km experiment. First, Fig. 16 is a comparison of the experimental signal and noise power spectra. We see that an examination of the received time series in the 900-1000 Hz and 1600-1700 Hz bands would be meaningless since, in these frequency domains, the noise is dominated by strong peaks. In these two bands, the average power of the noise is approximately equal to the average power of the signal. Figures 17(a)-(d) are comparisons of the 14.07 km experiment in four frequency bands of 100 Hz width. The particular 100 Hz bands were chosen so that they contained about the same average signal-to-noise ratio. Also, the largest amplitude in the experimental 50-150 Hz time series has been scaled to unity. Further, pressure amplitudes in bands other than the 50-150 Hz band are renormalized by dividing them by the factor $\log_{10}\left[(\underline{P}_a-\underline{P}_{ref})/20\right]$. Here, $\underline{P}_a$ and $\underline{P}_{ref}$ are the average source power (in decibels) in the frequency band of interest and the 50-150 Hz band, respectively. This renormalization compensates for the decrease in amplitudes due to the smaller amounts of source energy in the higher frequency bands and allows an interpretation of reductions in amplitudes in terms of acoustic processes and as the loss of high frequency energy due to sediment absorption.

Recall that theoretically the received time series of the 14.07 km experiment could be constructed out of a superposition of four

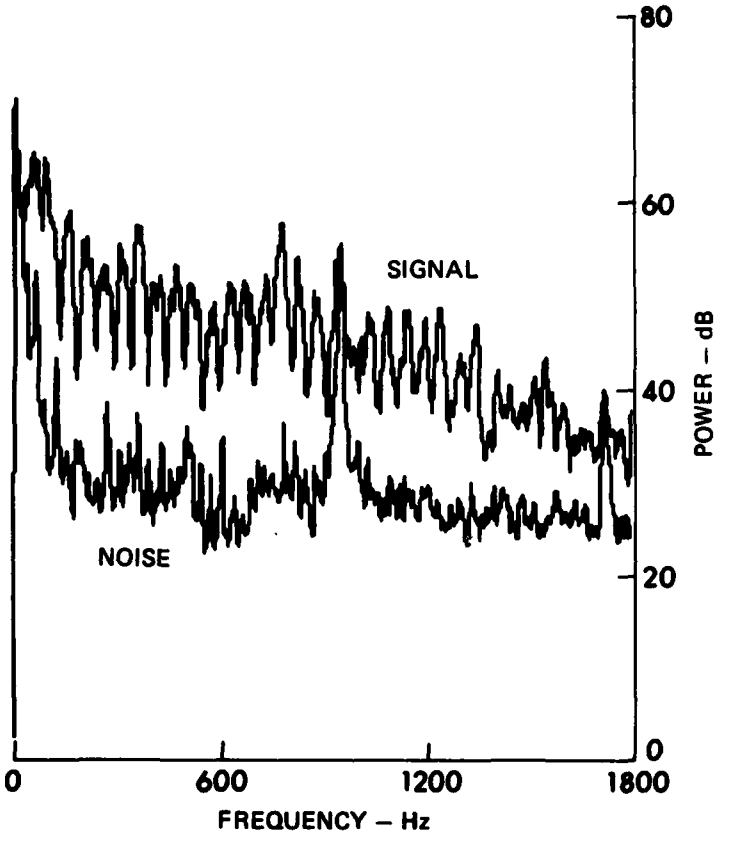

FIGURE 16
COMPARISON OF THE POWER SPECTRUM OF THE NOISE AND SBI SIGNAL
14.07 km EXPERIMENT

ARL:UT
AS-83-1054
DPK - GA
10 - 3 - 83

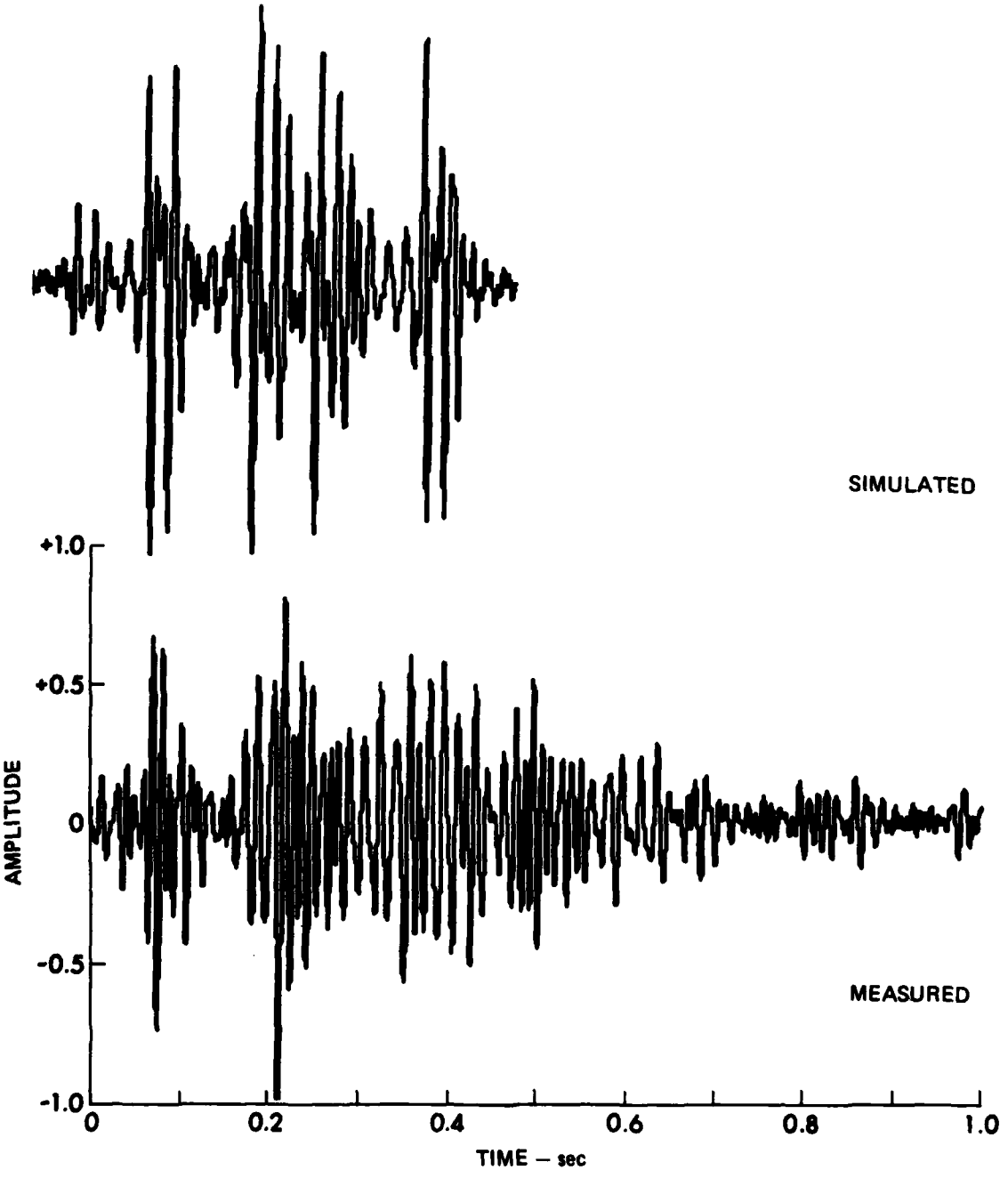

FIGURE 17(a)
COMPARISON OF SIMULATED AND MEASURED SBI TIME SERIES
14.07 km, 50-150 Hz

ARL:UT
AS-83-1055
DPK - GA
10 - 3 - 83

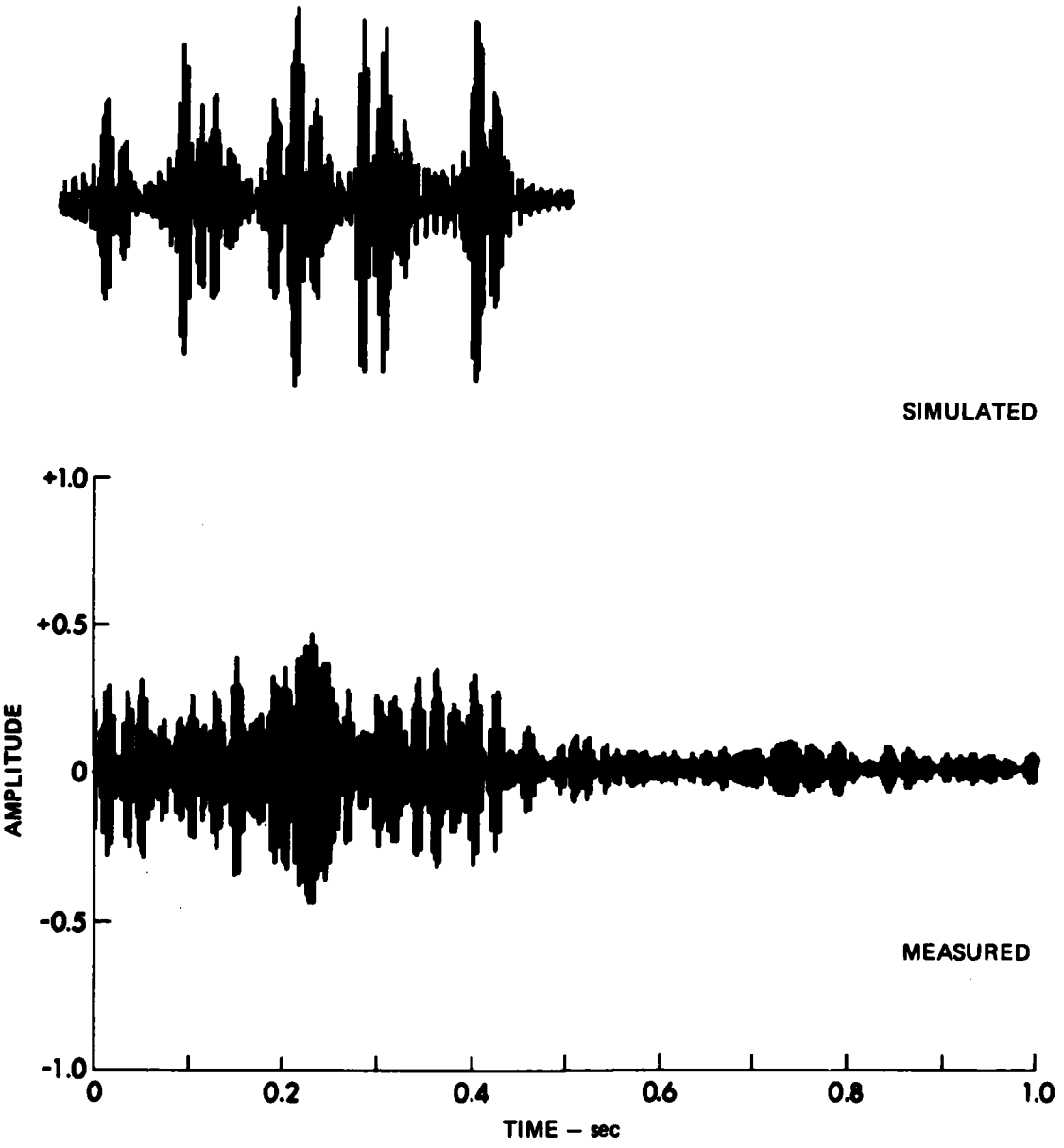

FIGURE 17(b)
COMPARISON OF SIMULATED AND MEASURED SBI TIME SERIES
14.07 km, 200-300 Hz

ARL:UT
AS-83-1056
DPK - GA
10 - 3 - 83

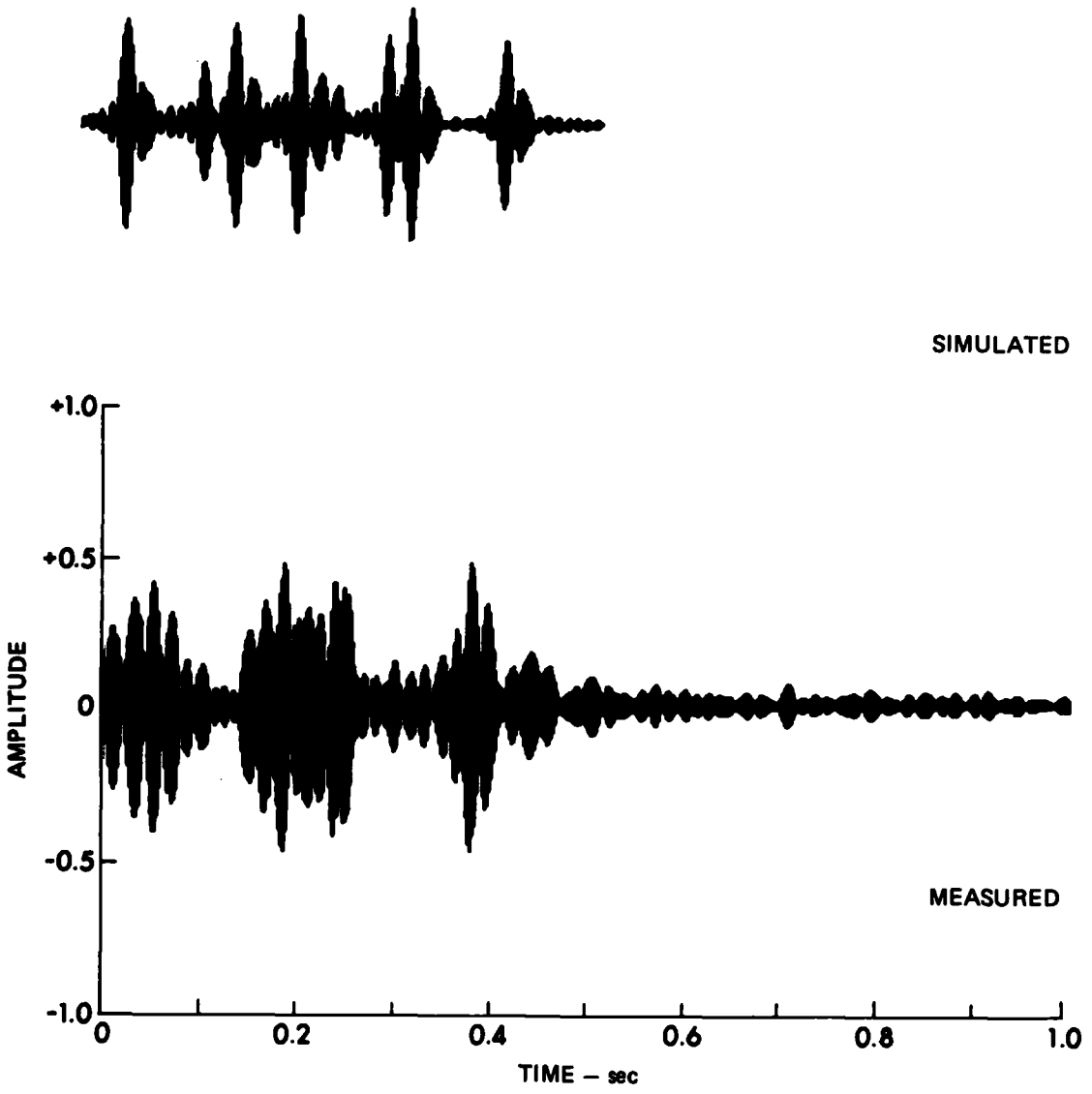

FIGURE 17(c)
COMPARISON OF SIMULATED AND MEASURED SBI TIME SERIES
14.07 km, 400-500 Hz

ARL:UT
AS-83-1057
DPK - GA
10 - 3 - 83

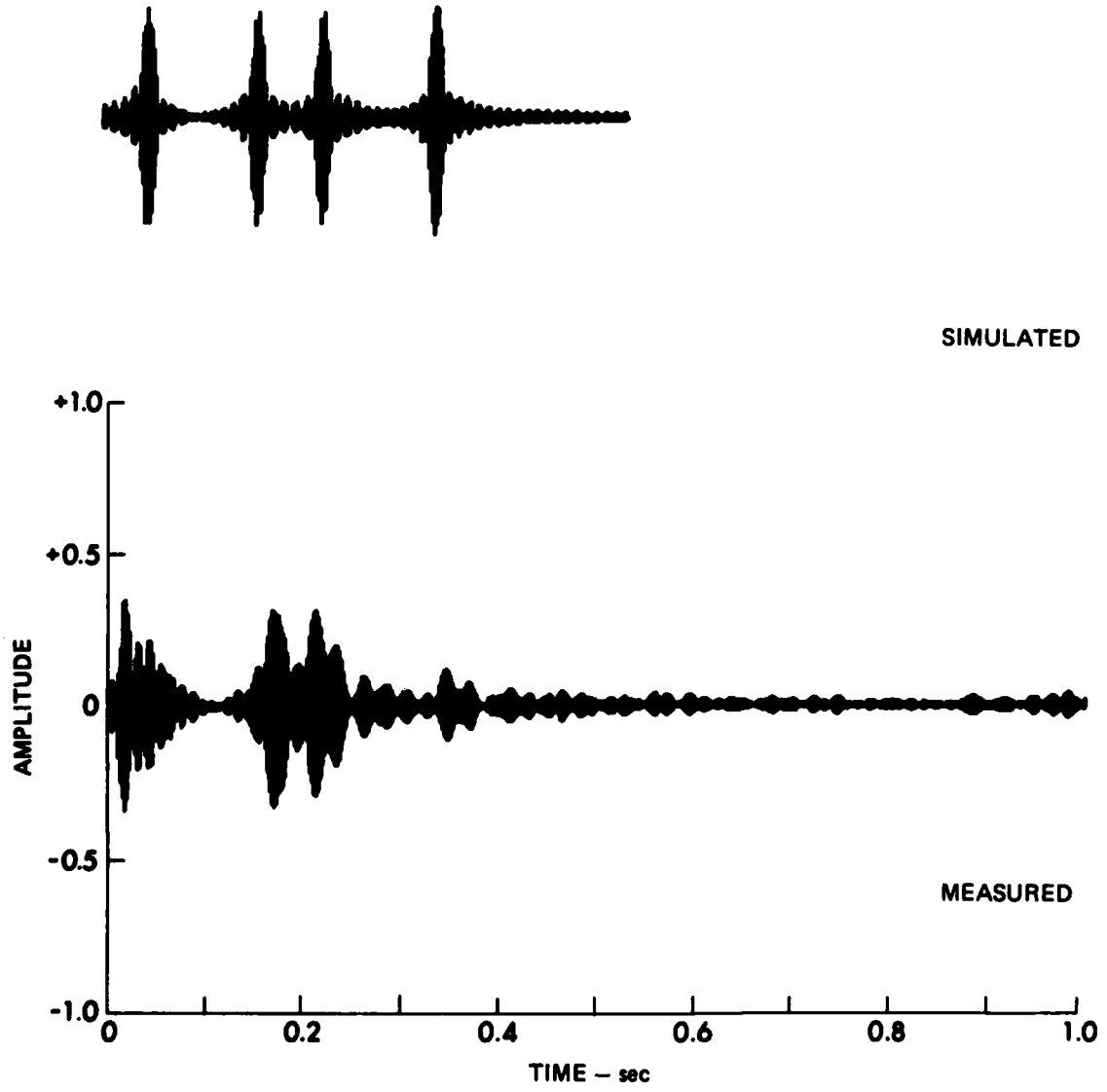

FIGURE 17(d)
COMPARISON OF SIMULATED AND MEASURES SBI TIME SERIES
14.07 km, 1500-1600 Hz

ARL:UT
AS-83-1058
DPK - GA
10 - 3 - 83

specular and four basement reflected eigenrays (see Fig. 14). Figure 17(a) shows that the low frequency (50-150 Hz) nature of the received signal is mainly characterized by the four basement reflected arrivals. As an example, one sees that the amplitude of the specular arrival with no water-air reflections (0.02-0.05 sec) is much smaller than the basement arrival with no water-air reflections (0.05-0.1 sec). Also note that a significant amount of low frequency energy is contained in secondary arrivals (0.47-1.0 sec).

Figure 17(b) is the 14.07 km comparison in the 200-300 Hz band. As the 100 Hz band moves toward the higher frequencies, arrivals appear simply as spikes, symmetric about the zero pressure line, followed by similar but smaller spikes. The larger spikes are the initial pulses and the smaller ones, the first bubble pulse. For the very high frequency bands, the bubble pulse contribution vanishes. The theoretical arrivals in the higher frequency bands all have the same shape, except for amplitude, regardless of the ray path type. In Fig. 17(b), we first observe that the amplitudes of the specular arrivals have increased relative to the amplitudes of the reflected basement arrivals. We also observe a substantial decrease in the amplitudes of the secondary arrivals. It is evident that the theoretical time series does not account for all of the characteristics of the experimental time series. Specifically, the observed specular arrivals are more structured than those predicted by the single layer model (0.0-0.05 sec), suggesting that the sediment is layered.

Figure 17(c) illustrates that the 400-500 Hz band has excluded enough low frequencies so that the amplitudes of the specular reflected arrivals are larger than those of the reflected basement arrivals. One observes fair agreement between theory and experiment except, as previously indicated, the individual experimental specular arrivals persist longer and are more structured than the theoretical arrivals. Also, we see that the amplitudes of the secondary arrivals are very small.

Finally, Fig. 17(d), the 1500-1600 Hz comparison, clearly shows that the only significant received energy at the higher frequencies is due to surface or near-surface reflections. The data clearly shows structured returns where the model predicts only single specular arrivals. It is not clear why the experimental surface arrival with two water-air reflections (0.34-0.38 sec) has a much smaller amplitude than the other three arrivals.

We now turn our attention to a bandpass frequency analysis of the 0.55 km experiment. Recall that the agreement in the broadband comparison for this range was very poor (Fig. 15). The experimental time series is saturated with complicated arrival structures possessing both low and high frequency components. From our previous bandpass analysis of the 14.07 km experiment, one is tempted to suggest that the high frequency returns in the 0.55 km experiment are due mostly to surface or near-surface interactions.

Figure 18(a) is the 0.55 km comparison in a 50-150 Hz frequency band. Except for the secondary arrivals, the theory predicts the overall duration of the observed signal (approximately 900 msec). However, the four low frequency reflected basement arrivals predicted by the theory cannot explain the excess of the observed low frequency arrivals in the time interval where the theory predicts a signal.

Figures 18(b) and 18(c) illustrate the 200-300 Hz and 400-500 Hz band comparisons. In both comparisons, the amplitudes of the theoretical specular returns are only one-third the size of the observed returns. Also, the theoretical specular returns, e.g., the arrival with no water-air reflections, persist for only about 30 msec, whereas the experimental returns persist for about 200 msec. Again, in Fig. 18(b), as in Fig. 18(a), the theoretical model correctly predicts the time duration of the primary signal, but fails to explain the large excess of observed signals in the time interval where the theory predicts a nonzero signal. Figure 18(c) clearly shows that the experimental signals, in the time interval where the theory predicts specular arrivals, are highly structured. Further, we see that the amplitudes of the secondary arrivals decrease as the frequency band moves from the 200-300 Hz band to the 400-500 Hz band. It is important to keep in mind that the analysis is designed so that any decrease in the amplitude of the secondary arrivals can only be due to frequency dependent effects such as absorption within the sediment.

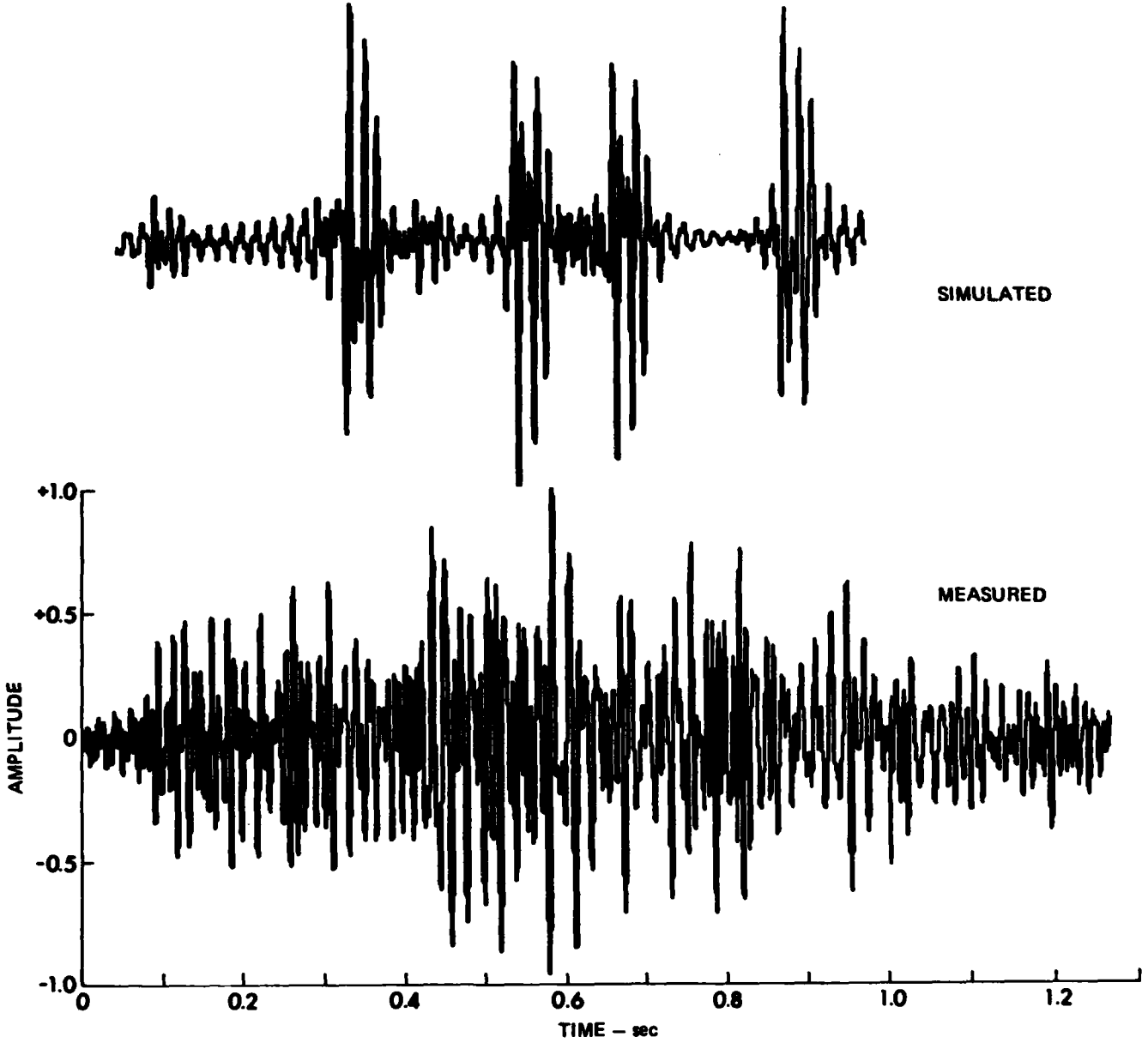

ARL:UT
AS-83-1069
DPK-GA
10-3-83

FIGURE 18(a)
COMPARISON OF SIMULATED AND MEASURED SBI TIME SERIES
0.55 km, 50-150 Hz

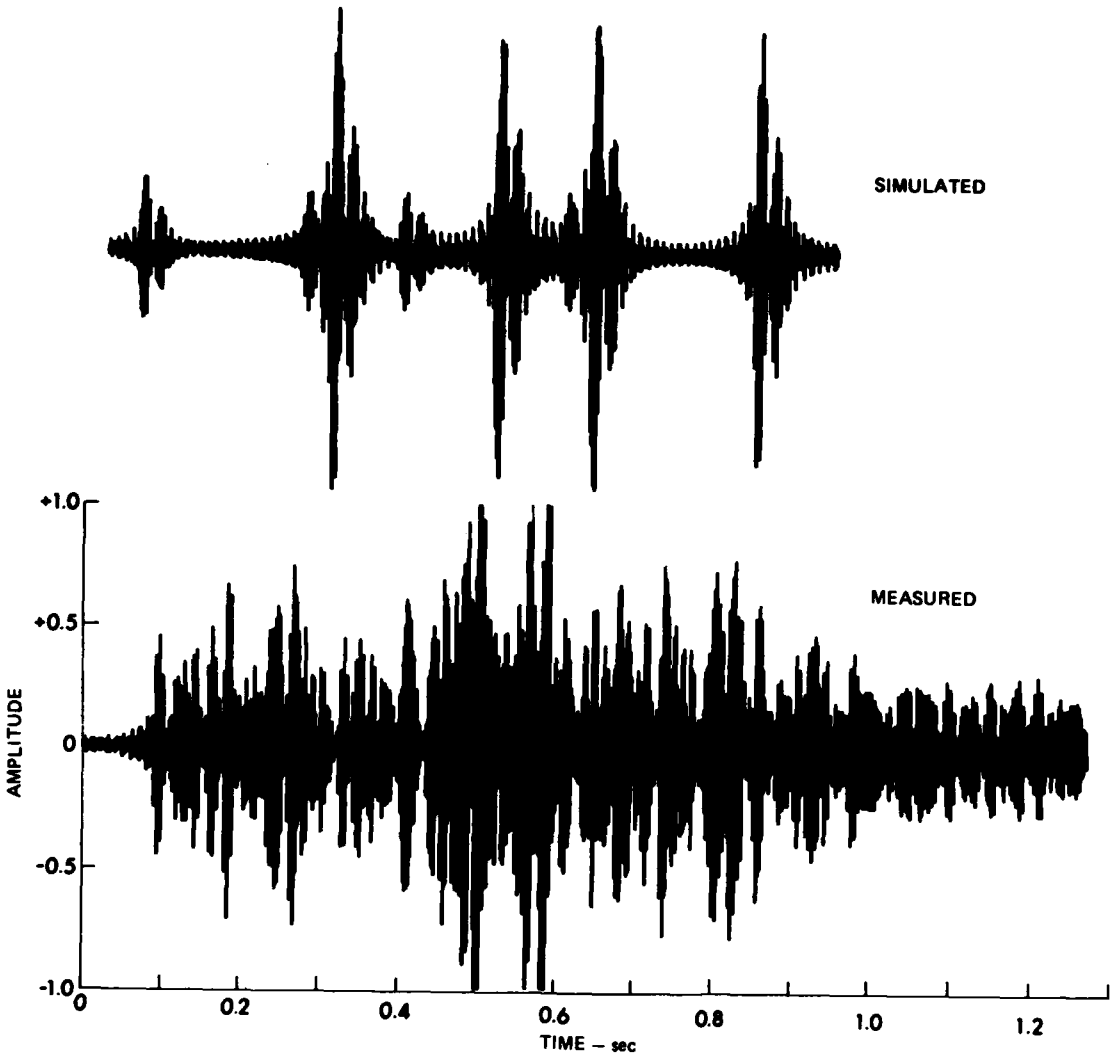

FIGURE 18(b)
COMPARISON OF SIMULATED AND MEASURED SBI TIME SERIES
0.55 km, 200-300 Hz

ARL-UT
AS-83-1060
DPK-GA
10-3-83

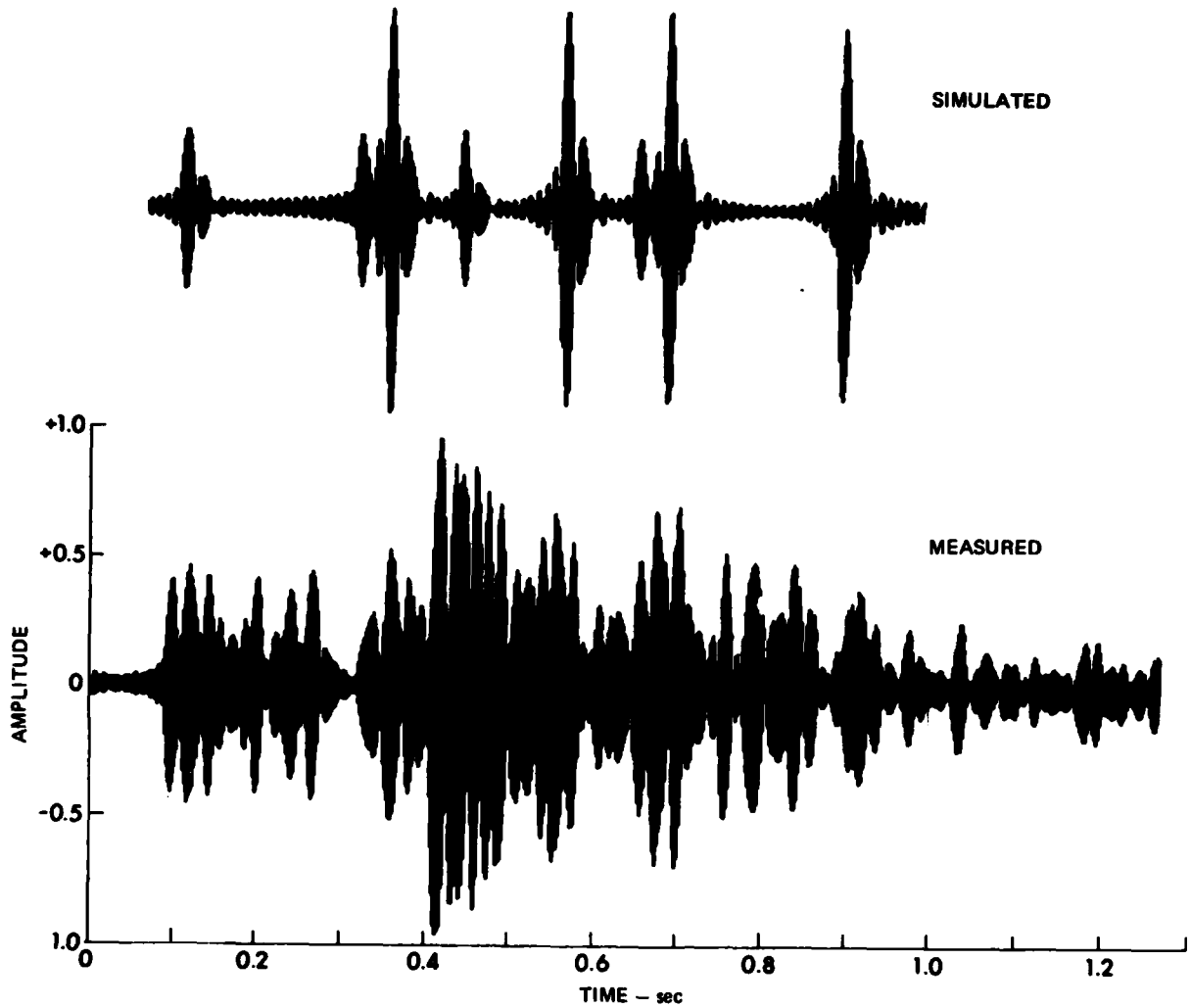

FIGURE 18(c)
COMPARISON OF SIMULATED AND MEASURED SBI TIME SERIES
0.55 km, 400-500 Hz

ARL:UT
AS-83-1061
DPK-GA
10-3-83

Figure 18(d) shows the 1500-1600 Hz band comparison. Here, the theoretical arrivals are dominated by specular arrivals. The reflected basement arrivals have been heavily attenuated. The experimental signal has clearly separated into three groups of arrivals. We see that the arrival times of the predicted specular rays coincide with the observed arrivals. It is believed that the observed middle arrival is a superposition of surface (water-sediment) and near-surface reflections of the two types of eigenrays with one water-air interaction (0.31-0.5 sec). Again, we observe that the amplitudes of the secondary arrivals are very small.

C. Interpretation of the Discrepancies

The comparisons of the experimental and the simulated time series show that our geoacoustic model is unable to describe all of the observed effects of the ocean bottom on sound propagation in an abyssal plains environment. It is natural to suspect that the source of the discrepancies may be the two major assumptions of the model, namely range invariance and that the sediment consists of a single layer. We will explore the possibility that near-surface thin layering and scattered arrivals from the basement are responsible for the discrepancies.

First, we investigate the possibility that near-surface, thin layering in the sediment is responsible for the discrepancies between theory and experiment within the time intervals where the model predicts a specular arrival. We recall that the observed arrivals in these time

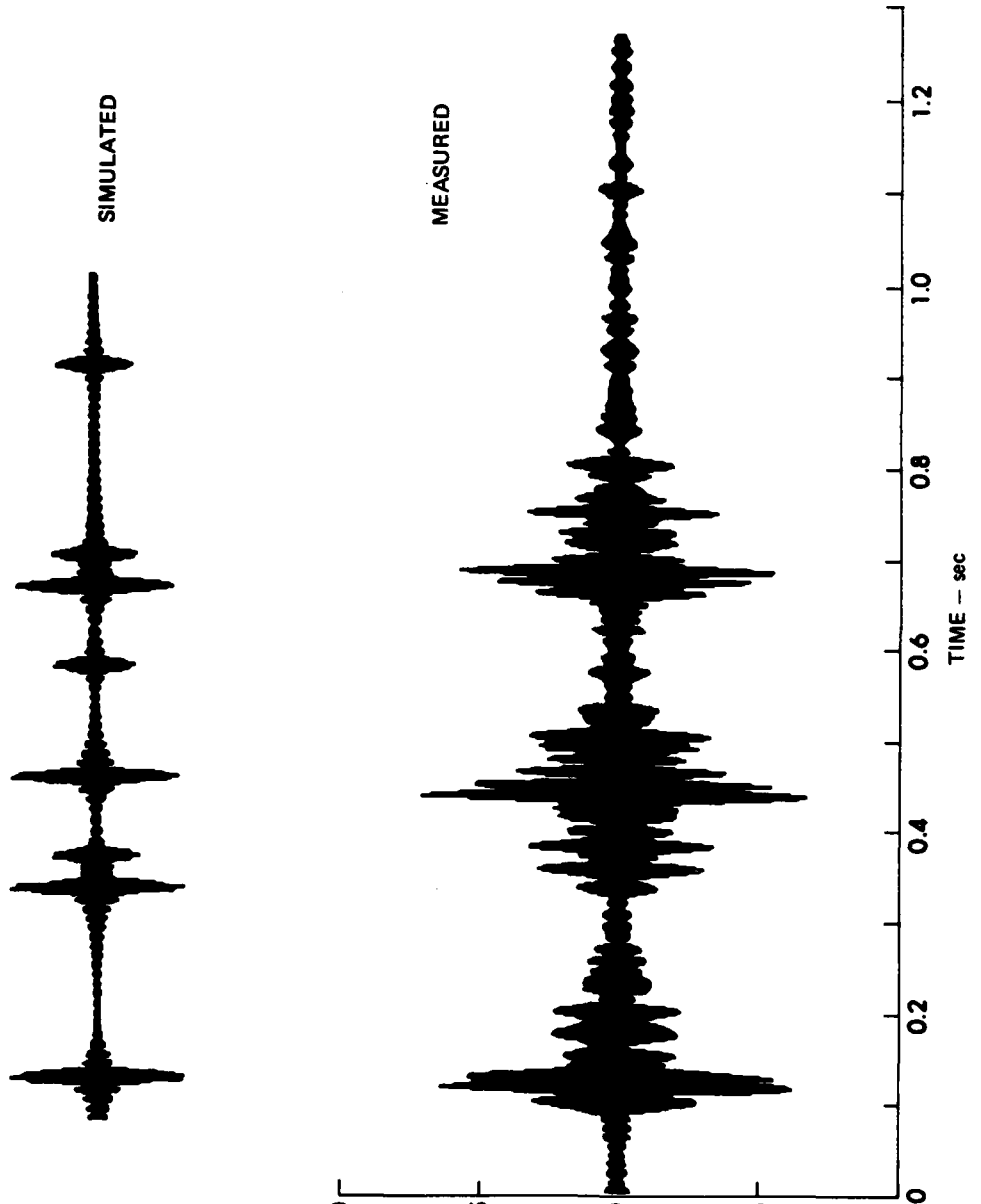

FIGURE 18(d)
COMPARISON OF SIMULATED AND MEASURED SBI TIME SERIES
0.55 km, 1500-1600 Hz

ARL:UT
AS-83-1062
DPK - GA
10 - 3 - 83

intervals were mostly high frequency in nature. Refracted arrivals, because of their low frequency nature, are controlled by the average velocity structure of the sediment. Variations in the velocity structure caused by thin layering (microstructure) are averaged over by the long wavelength refracted rays. In effect, the refracted rays are unaffected by thin layering. Indeed, the single layer model simulated, with great accuracy, the observed refracted arrivals for the long range experiments. However, high frequency energy, whose wavelengths are on the order of 1 m, would interact with thin layers near the water-sediment interface. These interactions, unhindered by any significant attenuation because of the short path length in the sediment, could conceivably return large amounts of high frequency energy to the receiver for large grazing angles or, equivalently, short ranges.[20]

The bandpass analysis of the 14.07 km and the 0.55 km experiments strongly supports the idea that thin layering is present in the region of the Tufts abyssal plains, where the data were collected. The 50-150 Hz 14.07 km comparison (Fig. 17(a)) showed that the largest contribution to the received signal in this frequency band came from reflected basement arrivals. The relative amplitudes of the simulated waveform agreed with the measured time series in the region where the simulated waveform predicted a specular arrival with no water-air interaction (0-0.05 sec). As the 100 Hz band moved toward the higher frequencies, we observed that both the theoretical and the experimental amplitudes in this time interval increased relative to the basement arrivals (see Figs. 17(c) and 17(d)). In Fig. 17(d), the theoretical

model predicts that the only contributions in the 1500-1600 Hz band come from the four specular arrivals. The experimental time series is very similar to the simulated waveform. Four distinct experimental arrivals are present and their travel times coincide with the theoretical arrivals. However, the individual experimental arrivals persist longer than the simulated arrivals. For example, the first observed arrival is about 80 msec longer than the corresponding simulated arrival. Thin layering near the surface could distort the pressure signature of the SUS charge waveform by multiple reflections from the various interfaces beneath the surface. This would have the effect of "stretching out and smearing" the initial pulse. This behavior is clearly shown in Fig. 18(d), where the initial pulse is smeared over an interval of 200 msec. Here, the incident angle is very close to normal. As the range increases or the incident angle decreases, the duration of the initial pulse caused by layering near the surface decreases (see Fig. 17(d)).

Several other independent studies support the existence of thin layers in the sediment. A theoretical study showed that a stack of thin layers has the combined effect of lowering bottom loss for the higher frequencies since a larger amount of energy is returned to the receiver by high frequency multiple specular reflections.[20] Also, bottom loss studies in the Pacific and Atlantic consistently show a much lower bottom loss for the high frequencies (800-1600 Hz) than that predicted by a single layer model. In fact, an empirical high density thin surface layer is used to fit the data.[21,22] In addition to the above studies,

Chapman has been able to explain the structure of bottom loss curves taken from the Tufts Abyssal Plains, by considering the sediment to be composed of thin layers of sand and clay caused by turbidity currents.[23] This model is supported by Hamilton's work in the area, which indicates thin layers of sand located in and near the turbidity channels.[1] Furthermore, Hastrup concludes, after an analysis of time series data taken from the Tyrrhenian abyssal plain, that the top part of the sediment (first 50 m) is composed of thin layers of sands (caused by turbidity currents) mixed in a clay sediment.[24]

We now turn our attention to the secondary arrivals. No sediment processes which take place above the basement could possibly account for the 500 msec of secondary arrivals observed in Fig. 11 for the 23.2 km experiment. Recall that we have already accounted for specular arrivals, sediment refracted arrivals, and basement reflected arrivals. Also, since the secondary arrivals have been shown to have only low frequency components, scattering from a rough water-sediment interface can be ruled out. This is true because scattered energy from the water-sediment interface would have both high and low frequency components. Further, reasonable compressional speed gradients in the basement cannot account for the secondary arrivals, because arrivals which have a single refraction within the basalt would arrive before the first bottom interacting arrival. This occurs because of the large compressional speeds for basalt (see Table I). As previously mentioned, rays which bounce off the ocean bottom twice have a much larger travel time than the last secondary arrival. A possible explanation for the

secondary arrivals is that they are the result of eigenrays formed by scattered reflections at the sediment-basement interface. In order to investigate this possibility, we introduce some simple ideas which, if expanded, may be able to explain the gross characteristics of the secondary arrivals.

Consider all rays launched from the source that strike the sediment-basement interface. The number of these rays for a given source-receiver geometry will be limited because of the positive sound speed gradient in the sediment. Now imagine that at each point along the sediment-basement interface there exists a wedge with the ability to vary its horizontal slope. The idea is that, given an initial downgoing Snell's invariant (P_1), one can find the upgoing Snell's invariant (P_2) necessary for an eigenray, if it exists. From P_2, one can find the slope ψ needed for an eigenray and proceed to calculate the ray travel time as a function of ψ (see Appendix B). Figure 19 plots travel time as a function of basement slope for various ranges. The geoacoustic parameters are the same as those listed in Table I. One sees that for the range of 0.55 km, the graph is parabolic in shape, with a minimum near the slope of zero. Also, one observes that the slopes, which would be needed to account for the secondary arrivals which persist for about 0.5 sec for the 0.55 km case, would have to be on the order of $\pm 30^{o}$.

One of the most interesting results is that there are <u>no</u> slopes at the basement which can enable a ray to reach the receiver via a scattered reflection for ranges greater than 15 km. Recall that this is

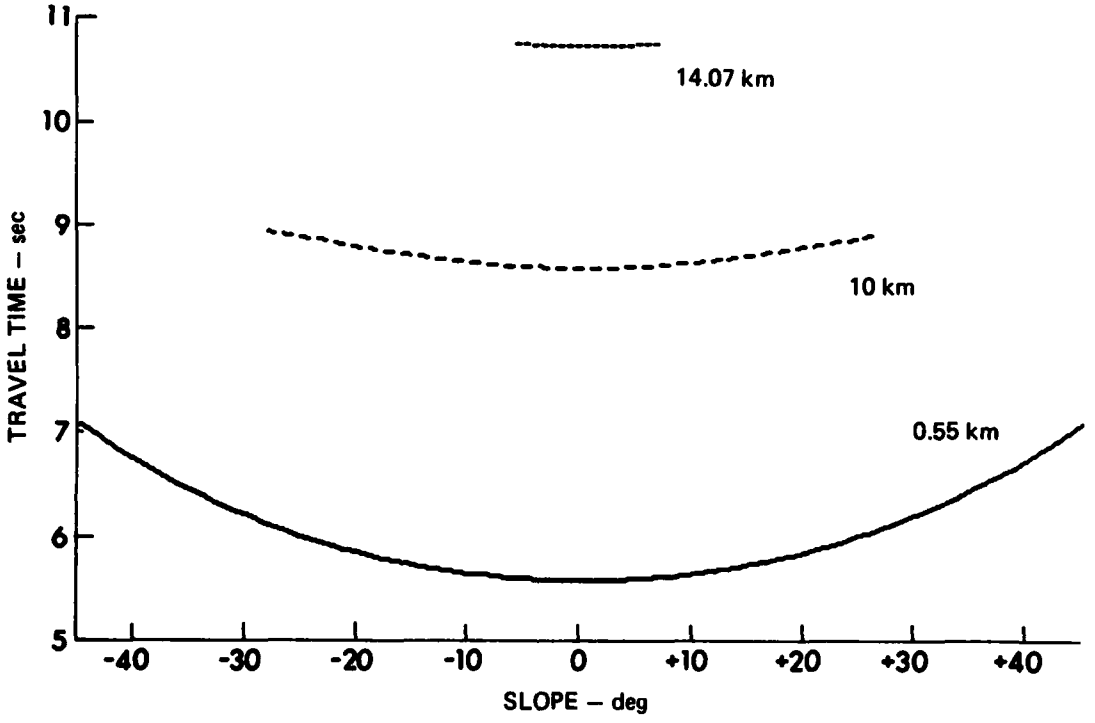

FIGURE 19
TRAVEL TIME versus POINT SLOPE AT BASEMENT
FOR SBI EIGENRAY FOR THREE RANGES

ARL:UT
AS-83-1064
DPK - GA
10 - 3 - 83

the range in which ray theory predicted a transition from refracted to basement reflected eigenrays. The sediment thickness (here 200 m) and the sound speed gradient (1.23 sec^{-1}) are large enough to prohibit a ψ which would allow the horizontal distance traveled in the sediment, after the basement reflection, to become large enough to satisfy the range equation when the range is greater than 15 km.

If the range and sediment thickness are such that a scattered eigenray, confined to the x-z (range depth plane), does not exist, then an eigenray which travels out of the plane and then scatters back to the receiver does not exist either. To show that the above statement is true, consider the sediment-basement interface as a flat plane embedded with point scatterers. These scatterers now consist of an additional slope besides the slope in the x-z plane. This extra slope, call it ψ', is defined in the plane perpendicular to the x-z plane. In the case where the ray is confined to the x-z plane, the horizontal distance that the ray travels in the sediment, after it has a scattered reflection from the sediment-basement interface, is

$$X = \int_{z_h}^{0} \frac{n_o \sin\theta_o \, dz}{\sqrt{n(z)^2 - n_o^2 \sin^2\theta_o}} \quad . \tag{19}$$

Here n is the index of refraction and θ_o, from Fig. 20, is $\theta_B + 2\psi$. If one considers a ray which travels out of the plane and then is scattered at the basement, Eq. (19) becomes

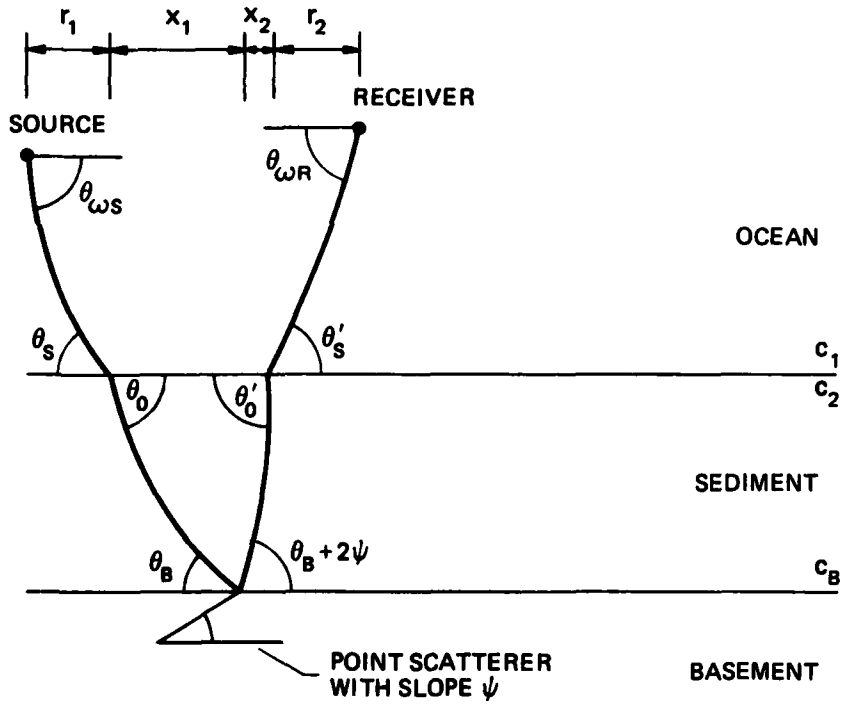

FIGURE 20
SCATTERED BASEMENT SBI EIGENRAY
CONFINED TO A PLANE

ARL:UT
AS-83-1063
DPK - GA
10 - 3 - 83

$$X = \cos\phi_0 \int_{z_h}^{0} \frac{n_0 \sin\theta_0 \, dz}{\sqrt{n(z)^2 - n_0^2 \sin^2\theta_0}} \quad . \tag{20}$$

Here ϕ_0 is the angle that the upgoing scattered ray makes with the x-z plane. Note that the only difference between Eq. (19) and Eq. (20) is the factor $\cos\phi_0$. Now, recall that for a range of 23.2 km a ψ could not be found which would allow x to become large enough to satisfy the range equation. Thus, we see that, if a scattered ray confined to the x-z plane is not an eigenray, then since $\cos\phi_0$ varies between ±1, a ray which is allowed to travel out of the x-z plane is unable to scatter back to the receiver.

Figure 21 illustrates the measured bathymetry taken during the experiment. Note the two large seamounts with slopes of about 9^o. Hamilton reports that the sediment thickness decreases to about 60 m on the sides and tops of the seamounts.[1] One can see that the 23.2 km experiment could easily be affected by the first seamount. It is possible that a theory which includes point slopes embedded in the global slopes of the seamounts could solve the paradox of the secondary arrivals for the long ranges. Such a theory would be of a range varying nature and is beyond the scope of this study.

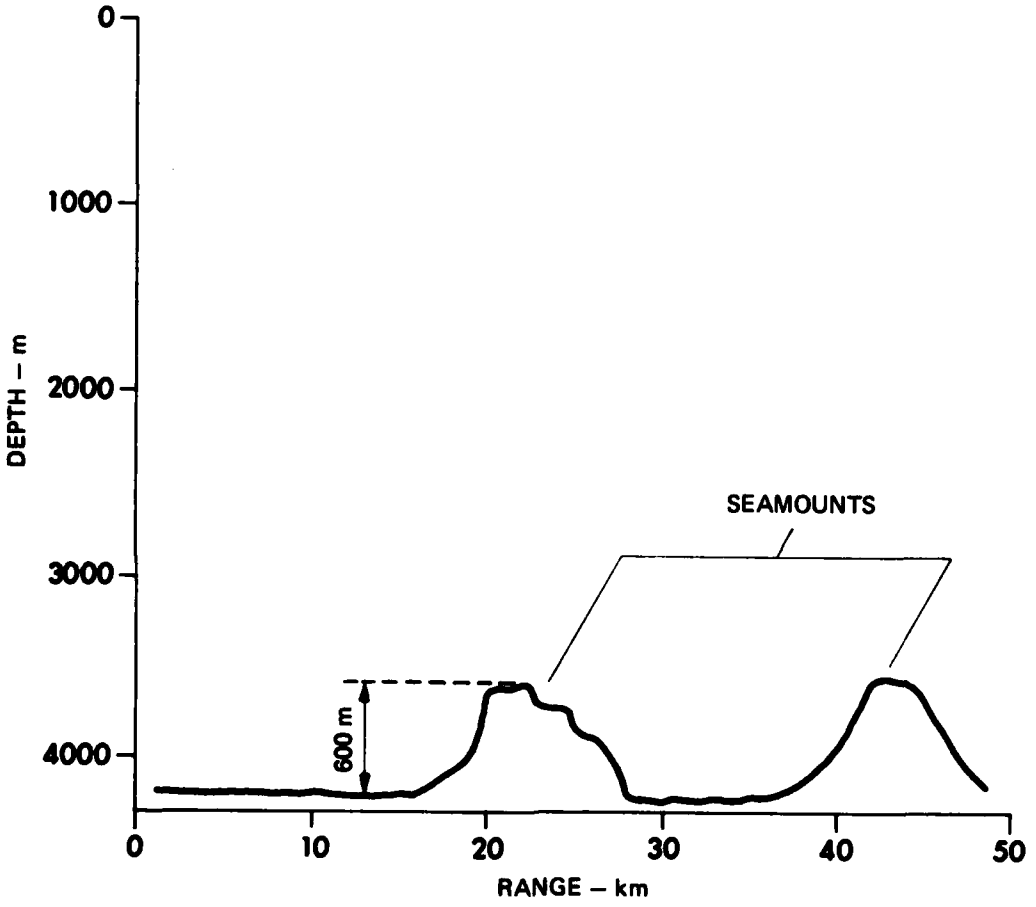

FIGURE 21
BATHYMETRY OF EXERCISE AREA

ARL:UT
AS-83-1065
DPK - GA
10 - 3 - 83

V. CONCLUSIONS

A ray theory model was used to simulate single bottom bounce time series due to TNT charge explosions in an abyssal plains environment. The simulated time series were compared to actual data in order to gain information concerning the general characteristics of the ocean bottom in abyssal plain environments.

The simulated time series were calculated using a simple geoacoustic profile. It was found that the best fit to the data was obtained with average geoacoustic parameters found in the literature. Also, it was discovered that changes in the receiver depth have a greater effect on the shape of the received signal than reasonable variations of the geoacoustic parameters.

For ranges greater than 15 km, most of the received energy travels along sediment refracting paths. The refracted arrivals can be identified solely on the basis of their distorted shapes due to the grazing of a caustic line located within the sediment. A frequency analysis further shows that the refracted energy is of a low frequency nature because of the frequency dependent absorption within the sediment. For these ranges in the time window where the theory predicts a received signal, the generally good agreement between theory and experiment shows that a single layer sediment with a sound speed increasing linearly with

depth is adequate in describing the first order effects of the ocean bottom on sound propagation. Since the refracted arrivals do not have high frequency components, thin sediment layers have no effect on them.

As the range decreases, the comparisons of the theoretical to the simulated time series show that the relative amplitudes of the sediment penetrating arrivals decrease with respect to the arrivals reflected from the water-sediment interface. This is expected since the sediment penetrating rays go deeper into the sediment, thus accumulating a greater amount of geometrical spreading and absorption. However, the comparisons further reveal that the simple Rayleigh reflection coefficient at the water-sediment interface is inadequate in describing the high frequency arrivals. The interpretation for this discrepancy is that the upper part of the sediment consists of alternating thin layers of clay and sand. When the vertical acoustic wavelength is on the order of the average distance between the layers, cumulative reflection can result in the return of significant amounts of high frequency energy. This interpretation is supported by other works concerning abyssal plain environments.

The real test of verifying the above interpretations is to add thin layers to the range invariant model and reconstruct the comparison curves. As a first try, one might take an existing thin layer plane wave model (a thin layer model which uses the WKB approximation[25]) and construct the environmental frequency response. This could be used to construct the received signal due to energy which is free of water-air

reflections. A comparison with the first 150 msec of the observed time series should show whether thin layering is a possible explanation for the high frequency reflected arrivals.

The comparisons of the simulated and measured time series identified reflected basement arrivals and tentatively identified the secondary arrivals to be due to scattered basement arrivals. For a range of 14.07 km, the comparisons identified a reflected basement arrival on the basis of its distortion due to a basement reflection below the critical angle. A simple calculation showed that the secondary arrivals, for the experiments where the range was greater than 15 km, could not be due to point scatterers embedded in a flat plane. Bathymetry data, however, showed two large seamounts in the experiment area. Scattered energy from the basement rock on the seamounts could account for the secondary arrivals. A frequency analysis showed the secondary arrivals to be of a low frequency nature, further supporting the idea that they are of a basement interacting nature. A full accounting of the secondary arrivals would necessitate a transition to a complex range varying model (possibly three-dimensional), which would include scatterers embedded within global slopes defined by the bottom bathymetry. A preliminary investigation of the effects of seamounts can be conducted with present day range varying ray models.[26] The ray model could calculate travel times for eigenrays, if they exist, that scatter off the seamounts. These travel times could then be compared to those of the observed travel times for the secondary arrivals.

APPENDIX A

DERIVATION OF THE TOTAL SEDIMENT ABSORPTION FOR A SEDIMENT PENETRATING RAY

It is assumed that the decrease in the pressure amplitude P due to the intrinsic absorption within the sediment is governed by a linear first order differential equation

$$\frac{dP}{ds} = -\kappa_i P \quad . \qquad \text{A.1}$$

Here S is the arc length of the ray path within the sediment and κ_i is the imaginary part of the acoustic wave number containing the total absorption. The solution is

$$P(s) = P_o \exp\left[-\int \kappa_i ds\right] \quad . \qquad \text{A.2}$$

We now assume that the total absorption is linearly proportional to the frequency and convert to decibel units. Hamilton's expression for absorption, κ_H, has units in dB/m-kHz. The definition of intensity difference can be expressed in decibel units, where the standard definition of the decibel is

$$db = -10 \log_{10}\left[(P/P_o)^2\right] \quad . \qquad \text{A.3}$$

It follows that

$$P(x) = P_0\, 10^{-\{(f/1000)\int \kappa_H ds\}} \quad , \qquad \text{A.4}$$

and combining with Eq. (A.2), we find that

$$-\int \kappa_i ds = \ell n\left[10^{-\{(f/2000)\int \kappa_H ds\}}\right] \qquad \text{A.5}$$

or

$$\int \kappa_i ds = \frac{2\pi f\ \ell n(10)}{4\pi \times 10^4} \int \kappa_H ds \quad , \qquad \text{A.6}$$

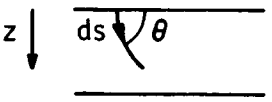

From the above diagram, we see that $dZ=\sin\theta dS$. If $\alpha(Z)$ is the attenuation, with units of dB/m-kHz as a function of Z, then

$$\int \kappa_H ds = 2\int_0^Z \frac{\alpha(z')dz'}{\sin\theta} \quad , \qquad \text{A.7}$$

where Z is the turning depth for a refracting ray or the depth of the sediment if the ray is of a basement reflecting type. From Snell's law $a_j=\cos\theta_j/c_j$, where a_j is the Snell's invariant for the jth ray, since

$\sin\theta = \sqrt{1-\cos^2\theta}$, we know that the total absorption of a ray passing through the sediment is

$$A_j = \frac{\ell n(10)}{4\pi \times 10^4} \; 2\int_0^z \frac{\alpha(z')dz'}{\sqrt{1 - a_j^2 c^2(z')}} \quad . \qquad \text{A.8}$$

APPENDIX B

DERIVATION OF TRAVEL TIME AS A FUNCTION OF THE SLOPE EMBEDDED IN A FLAT BASEMENT FOR A SINGLE BASEMENT INTERACTING EIGENRAY

It is assumed that both the water and sediment sound speed structure are linear, i.e.,

$$c = c_o + g_w z \quad , \qquad \text{B.1}$$

and

$$c = c_2 + g_s z \quad , \qquad \text{B.2}$$

where g_w and g_s are the sound speed gradients of the water column and sediment, respectively.

From Fig. 20, the downgoing Snell's invariant is

$$P_1 = \frac{\cos\theta_s}{c_1} = \frac{\cos\theta}{c} \quad . \qquad \text{B.3}$$

The range equation is

$$R = X_1 = X_2 = r_1 + r_2 \quad , \qquad \text{B.4}$$

To calculate r_1 and r_2, we note that

$$dc = g_s dz = -\frac{\sin\theta}{P_1} d\theta \quad , \qquad \text{B.5}$$

and

$$\tan\theta = \frac{dz}{dx} = \frac{\sqrt{1 - P_1^2 c^2}}{P_1 c} \quad . \qquad \text{B.6}$$

From these relationships, we find r_1 and r_2 to be

$$r_1 = -\frac{1}{g_s P_1}(\sin\theta_B - \sin\theta_o) \quad , \qquad \text{B.7}$$

$$r_2 = -\frac{1}{g_s P_2}\left(\sin\theta_o' - \sin(\theta_B + 2\psi)\right) \quad , \qquad \text{B.8}$$

where $P_2 c_B = \cos(\theta_B + 2\psi)$. Similarly, X_1 and X_2 are found to be

$$X_1 = -\frac{1}{g_s P_1}(\sin\theta_s - \sin\theta_{ws}) \text{ and } X_2 = -\frac{1}{g_w P_2}(\sin\theta_{wr} - \sin\theta_s') \quad . \qquad \text{B.9}$$

With a little rearrangement, the range equation can be placed in the form

$$\beta = -\frac{1}{g_s}\left\{\sqrt{\alpha^2 - c_2^2} - \sqrt{\alpha^2 - c_B^2}\right\} + \frac{1}{g_w}\left\{\sqrt{\alpha^2 - c_1^2} - \sqrt{\alpha^2 - c_R^2}\right\} \quad . \qquad \text{B.10}$$

where

$$\alpha > c_1 \quad , \quad \alpha > c_2 \quad , \quad \alpha > c_B \quad , \quad \alpha > c_R \quad ,$$

and

$$\alpha \equiv \frac{1}{P_2} \quad , \quad \beta \equiv r_2 + x_2 \quad .$$

Since one has an equation involving the square of α, mathematically one has two roots. Physically one uses

$$\alpha = \begin{cases} +\alpha & R - X_1 - r_1 > 0 \\ -\alpha & R - X_1 - r_1 < 0 \end{cases} , \qquad \text{B.11}$$

To find ψ, we simply use Snell's law

$$P_2 c_B = \cos(\theta_B + 2\psi) , \qquad \text{B.12}$$

or

$$\psi = \frac{\cos^{-1}(P_2 c_B) - \theta_B}{2} . \qquad \text{B.13}$$

To find the ray travel time, we use the general expression

$$t_s = \int_0^s \frac{ds'}{c} , \qquad \text{B.14}$$

where the element of arc length is

$$ds = \sqrt{1 + \left(\frac{dx}{dz}\right)^2}\ dz .$$

Rearranging and using previous relationships, we find that the sediment travel time is

$$t_s = -\frac{1}{g_s}\left\{\ell n\left[\frac{\tan(\pi/4+\theta_B/2)}{\tan(\pi/4+\theta_o/2)}\right] + \ell n\left[\frac{\tan(\pi/4+\theta_o'/2)}{\tan(\pi/4+\theta_{wB}/2)}\right]\right\} \quad , \qquad \text{B.15}$$

and the water travel time is

$$t_w = -\frac{1}{g_w}\left\{\ell n\left[\frac{\tan(\pi/4+\theta_s/2)}{\tan(\pi/4+\theta_{ws}/2)}\right] + \ell n\left[\frac{\tan(\pi/4+\theta_s'/2}{\tan(\pi/4+\theta_{wR}/2)}\right]\right\} \quad . \qquad \text{B.16}$$

BIBLIOGRAPHY

1. E. L. Hamilton, "Marine Geology of Abyssal Plains in the Gulf of Alaska", J. Geophys. Res. 72, No. 16, 4189-4213 (1967).

2. E. L. Hamilton, "Geoacoustic Modeling of the Sea Floor", J. Acoust. Soc. Am. 68 (5), 1313-1339 (1980).

3. S. K. Mitchell, N. R. Bedford, and M. S. Weinstein, "Determination of Source Depth from the Spectra of Small Explosions Observed at Long Ranges", J. Acoust. Soc. Am. 60, 825-828 (1976).

4. S. K. Mitchell, N. R. Bedford, and G. E. Ellis, "Multipath Analysis of Explosive Source Signals in the Ocean", J. Acoust. Soc. Am. 67 (5), 1590-1597 (1980).

5. J. Wakeley, Jr., "Coherent Ray Tracing-Measured and Predicted Shallow Water Frequency Spectrum", J. Acoust. Soc. Am. 63 (6), 1820-1823 (1978).

6. R. J. Urick, Principles of Underwater Sound (McGraw-Hill Book Co., Inc., New York, 1975).

7. R. P. Feynman and A. R. Hibbs, Quantum Mechanics and Path Integrals (McGraw-Hill Book Co., Inc., New York, 1975).

8. D. R. Palmer, "A Path-Integral Approach to the Parabolic Approximation I", J. Acoust. Soc. Am. 66 (3), 862-871 (1979).

9. P. J. Vidmar, "Ray Path Analysis of Sediment Shear Wave Effects on Bottom Reflection Loss", J. Acoust. Soc. Am. 68 (2), 639-648 (1980).

10. J. Powell and B. Crasemann, Quantum Mechanics (Addison-Wesley, Reading, Massachusetts, 1961).

11. R. M. Barash, "Evidence of Phase Shift at Caustics", Letter to the Editor, J. Acoust. Soc. Am. 43 (2), 378-380 (1968).

12. I. Tolstoy, "Comments on 'Evidence of Phase Shift at Caustics'", Letter to the Editor, J. Acoust. Soc. Am. 43 (2), 380-381 (1968).

13. F. W. Bryon, Jr., and R. W. Fuller, Mathematics of Classical and Quantum Physics, Vol. II (Addison-Wesley, Reading, Massachusetts, 1970).

14. W. I. Futterman, "Dispersive Body Waves", J. Geophys. Res. 67 (13), 5279-5291 (1962).

15. M. O'Donnell, E. T. Jaynes, and J. G. Miller, "Kramers-Kronig Relationship between Ultrasonic Attenuation and Phase Velocity", J. Acoust. Soc. Am. 69 (3), 696-701 (1981).

16. T. L. Foreman, "Acoustic Ray Models Based on Eigenrays", Applied Research Laboratories Technical Report No. 77-1 (ARL-TR-77-1), Applied Research Laboratories, The University of Texas at Austin, 1977.

17. E. A. Brigham, The Fast Fourier Transform (Prentice-Hall, Englewood Cliff, New Jersey, 1974).

18. R. E. Christensen, J. A. Frank, and W. H. Geddes, "Low-Frequency Propagation via Shallow Refracted Paths through Deep Ocean Unconsolidated Sediments", J. Acoust. Soc. Am. 57, 1421-1426 (1975).

19. P. J. Vidmar, "Preliminary Results of an Evaluation of the Efficiency of VLF Seismic Propagation in a Continental Slope Environment", Applied Research Laboratories Technical Report No. 82-36 (ARL-TR-82-36), Applied Research Laboratories, The University of Texas at Austin, 1982.

20. H. Holthusen and P. J. Vidmar, "The Effect of Near-Surface Layering on the Reflectivity of the Ocean Bottom", J. Acoust. Soc. Am. 72, 226-234 (1982).

21. C. W. Spofford, R. R. Greene, and J. B. Hersey, "The Estimation of Geo-Acoustic Ocean Sediment Parameters from Measured Bottom-Loss Data", Science Applications, Inc., McLean, Virginia, 1982.

22. D. Knobles and P. Vidmar, "Generation and Analysis of Bottom Loss Upgrade Geoacoustic Parameters for Specific Locations in the Northeast Pacific", Applied Research Laboratories Technical Report No. 82-17 (ARL-TR-82-17), Applied Research Laboratories, The University of Texas at Austin, 1982.

23. N. R. Chapman, "Low Frequency Bottom Reflectivity Measurements in the Tufts Abyssal Plain", in Bottom-Interacting Ocean Acoustics, edited by W. A. Kuperman and F. B. Jensen (Plenum Press, New York, 1980).

24. O. F. Hastrup, "Digital Analysis of Acoustic Reflectivity in the Tyrrhenian Abyssal Plain", J. Acoust. Soc. Am. 47 (1), 181-190 (1970).

25. Richard Pitre and Paul Vidmar, Applied Research Laboratories, The University of Texas at Austin, private communication.

26. T. L. Foreman, "MEDUSA: A Range Varying Ray Model", in preparation.

1 December 1983

DISTRIBUTION LIST FOR
ARL-TR-83-39
UNDER CONTRACT N00014-78-C-0113

Copy No.

Commanding Officer
Naval Ocean Research and Development Activity
NSTL Station, MS 39529
1 Attn: E. D. Chaika (Code 530)
2 R. Gardner (Code 501)
3 D. B. King (Code 321)
4 W. A. Kuperman (Code 320)
5 CDR M. McCallister (Code 522)
6 R. Martin (Code 110A)
7 J. Matthews (Code 362)
8 W. W. Worsley (Code 110A)

Chief of Naval Research
Department of the Navy
Arlington, VA 22217
9 Attn: M. McKisic (Code 4250A)
10 R. Obrochta (Code 425 AR)

Office of Naval Research Detachment
Naval Ocean Research and Development Activity
NSTL Station, MS 39529
11 Attn: G. Morris (Code 425GG)
12 LCDR M. McDonald (Code 425GG)

Commanding Officer
Naval Electronic Systems Command
Department of the Navy
Washington, D.C. 20360
13 Attn: LCDR S. Hollis (Code 612)
14 R. Mitnick (Code 612)
15 CDR C. Spikes (PDE 124-60)
16 L. Parish (PDE 124-50)

Director
Naval Research Laboratory
Department of the Navy
Washington, D.C. 20375
17 Attn: B. B. Adams (Code 8160)

Distribution list for ARL-TR-83-39 under Contract N00014-78-C-0113 (cont'd)

Copy No.

Commanding Officer
Naval Ocean Systems Center
Department of the Navy
San Diego, CA 92152
18 Attn: E. L. Hamilton
19 M. A. Pederson
20 H. P. Bucker

Commander
Naval Sea System Command
Department of the Navy
Washington, D.C. 20362
21 Attn: C. D. Smith (Code 63R)
22 D. E. Porter (Code 63R1)

Chief of Naval Operations
Department of the Navy
Washington, D.C. 20350
23 Attn: CAPT E. Young (OP 952D)

Chief of Naval Material
Department of the Navy
Washington, D.C. 20360
24 Attn: CAPT J. Harlett (MAT 0724)

25 Commander
Naval Surface Weapons Center
White Oak Laboratory
Department of the Navy
Silver Spring, MD 20910

26 Commander
David W. Taylor Naval Ship Research and
Development Center
Department of the Navy
Bethesda, MD 20034

Naval Oceanographic Office
Department of the Navy
NSTL Station, MS 39522
27 Attn: W. Jobst (Code 7300)
28 J. Allen (Code 7310)
29 R. Hecht (Code 7332)

Distribution list for ARL-TR-83-39 under Contract N00014-78-C-0113 (cont'd)

Copy No.

Commander
Naval Air Development Center
Department of the Navy
Warminster, PA 18974
30 Attn: C. L. Bartberger

Officer in Charge
New London Laboratory
Naval Underwater Systems Center
Department of the Navy
New London, CT 06320
31 Attn: B. Cole
32 F. R. DiNapoli
33 P. Herstein

34 Director Naval Warfare
Deputy Undersecretary Defense R&E
Room 3D1048, Pentagon
Washington, D.C. 20301

OASN (R,E&S)
Room 4D745, Pentagon
Washington, D.C. 20301
35 Attn: G. A. Cann

Superintendent
Naval Postgraduate School
Monterey, CA 93940
36 Attn: Library

Commander
Naval Coastal Systems Center
Department of the Navy
Panama City, FL 32407
37 Attn: G. McLeroy

Defense Advanced Research Projects Agency
1400 Wilson Blvd.
Arlington, VA 22209
38 Attn: CDR K. Evans (TTO)

39 Commander
Naval Intelligence Support Center
4301 Suitland Road
Washington, D.C. 20390

Distribution list for ARL-TR-83-39 under Contract N00014-78-C-0113 (cont'd)

Copy No.

40 - 51	Commanding Officer and Director Defense Technical Information Center Cameron Station, Building 5 5010 Duke Street Alexandria, VA 22314
	Woods Hole Oceanographic Institution 86-95 Water Street Woods Hole, MA 02543
52	Attn: R. Spindel
	Science Applications, Inc. 1710 Goodridge Drive McLean, VA 22101
53	Attn: C. Spofford
54	J. Hanna
	Applied Research Laboratory The Pennsylvania State University P. O. Box 30 State College, PA 16801
55	Attn: S. McDaniel
	Marine Physical Laboratory of The Scripps Institution of Oceanography The University of California, San Diego San Diego, CA 92132
56	Attn: F. Fisher
57	G. Shor
	Scripps Institution of Oceanography The University of California, San Diego La Jolla, CA 92037
58	Attn: Library
59	R. Tyce
	Bell Telephone Laboratories, Inc. Whippany Road Whippany, NJ 07961
60	Attn: A. Carter
61	R. Holford
62	D. Romain
	Planning Systems, Inc. 7900 Westpark Drive, Suite 507 McLean, VA 22101
63	Attn: R. Cavanaugh
64	B. Brunson

Distribution list for ARL-TR-83-39 under Contract N00014-78-C-0113 (cont'd)

Copy No.

TRW, Inc.
TRW Defense & Space Systems Group
Washington Operations
7600 Colshire Drive
McLean, VA 22101
65 Attn: R. T. Brown
66 I. Gereben

Defence Scientific Establishment
HMNZ Dockyard
Devonport, Auckland
NEW ZEALAND
67 Attn: K. M. Guthrie

School of Mechanical Engineering
Georgia Institute of Technology
Atlanta, GA 30332
68 Attn: A. D. Pierce

Department of Geology and Geophysics
Geophysical and Polar Research Center
Lewis G. Weeks Hall for Geological Sciences
The University of Wisconsin, Madison
1215 W. Dayton Street
Madison, WI 53706
69 Attn: C. S. Clay

Courant Institute
251 Mercer Street
New York, NY 10012
70 Attn: D. C. Stickler

Bolt, Beranek, & Newman, Inc.
50 Moulton Street
Cambridge, MA 02138
71 Attn: H. Cox

Hawaii Institute of Geophysics
The University of Hawaii
2525 Correa Road
Honolulu, HI 96822
72 Attn: L. N. Frazer

Director
North Atlantic Treaty Organization
SACLANT ASW Research Centre
APO New York 09019
73 Attn: T. Akal

AD-A137 380 AN INVESTIGATION OF ACOUSTIC INTERACTION WITH THE OCEAN 2/2
BOTTOM FROM EXPER.. (U) TEXAS UNIV AT AUSTIN APPLIED
RESEARCH LABS D P KNOBLES 01 DEC 83 ARL-TR-83-39
UNCLASSIFIED N00014-78-C-0113 F/G 20/1 NL

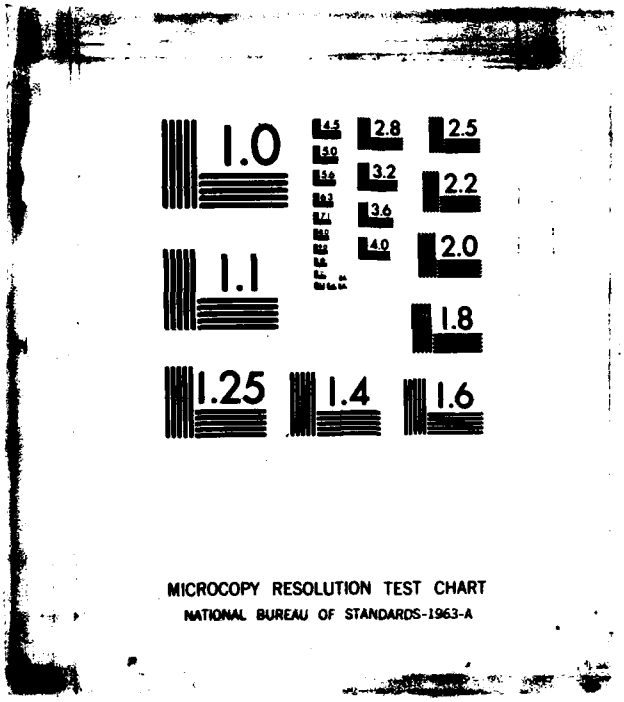
1.0
1.1
1.25
1.4
1.6
1.8
2.0
2.2
2.5
2.8
3.2
3.6
4.0
4.5
5.0
5.6
6.3
MICROCOPY RESOLUTION TEST CHART
NATIONAL BUREAU OF STANDARDS-1963-A

Distribution list for ARL-TR-83-39 under Contract N00014-78-C-0113 (cont'd)

Copy No.

Defence Research Establishment Pacific
FMO Victoria, BC
VOS 1BO CANADA
74 Attn: R. Chapman

Defence Research Establishment Atlantic
9 Grove Street
P. O. Box 1012
Dartmouth, NS
CANADA
75 Attn: D. Chapman

Rosenteil School of Marine and
Atmospheric Science
The University of Miami
10 Rickenbacker Causeway
Miami, FL 33149
76 Attn: H. DeFarrari

Applied Physics Laboratory
The Johns Hopkins University
Johns Hopkins Road
Laurel, MD 20810
77 Attn: J. Lombardo
78 R. Henrick

Department of Ocean Engineering
Massachusetts Institute of Technology
Cambridge, MA 02139
79 Attn: I. Dyer
80 G. Duckworth
81 A. Baggerar

The University of Miami
10 Rickenbacker Causeway
Miami, FL 33149
82 Attn: F. Tappert

Physics Department
The University of Rhode Island
Kingston, RI 02881
83 Attn: C. Kaufman

Department of Electrical Engineering
Polytechnic Institute of New York
Farmingdale, NY 11735
84 Attn: L. B. Felsen

Distribution list for ARL-TR-83-41 under Contract N00014-82-C-0049 (cont'd)

Copy No.

85 I. Tolstoy
Knockvennie, Castle Douglas
S. W. SCOTLAND
GREAT BRITAIN

Department of Geology
The University of Texas at Austin
Austin, TX 78712
86 Attn: C. Wilson

Physics Department
The University of Auckland
Private Bag, Auckland
NEW ZEALAND
87 Attn: A. C. Kibblewhite
88 C. T. Tindle

Chinhae Research Laboratory
P. O. Box 18
Chinhae, Kyeong Nam
KOREA
89 Attn: Jungyul Na

The Lamont-Doherty Geological Observatory
Columbia University
Palisades, NY 10964
90 Attn: R. D. Stoll

Ocean Data Systems, Inc.
Defense Systems
6110 Executive Blvd., Suite 320
Rockville, MD 20852
91 Attn: G. Jacobs
92 P. C. Etter

93 Nancy R. Bedford, ARL:UT

94 Karl C. Focke, ARL:UT

95 Terry L. Foreman, ARL:UT

96 Robert F. Gragg, ARL:UT

97 Loyd Hampton, ARL:UT

98 Kenneth E. Hawker, ARL:UT

Distribution list for ARL-TR-83-41 under Contract N00014-82-C-0049 (cont'd)

Copy No.

99	Stephen G. Houser, ARL:UT
100	Jo B. Lindberg, ARL:UT
101	Robert A. Koch, ARL:UT
102	David Knobles, ARL:UT
103	Stephen K. Mitchell, ARL:UT
104	David W. Oakley, ARL:UT
105	Clark S. Penrod, ARL:UT
106	Richard Pitre, ARL:UT
107	Carol V. Sheppard, ARL:UT
108	Paul J. Vidmar, ARL:UT
109	Library, ARL:UT
110-120	Reserve, ARL:UT

END

FILMED

02-84

DTIC